

MASS DEPENDENT GALAXY TRANSFORMATION MECHANISMS IN THE COMPLEX
ENVIRONMENT OF SUPERGROUP ABELL 1882

by

APARAJITA SENGUPTA

RONALD J. BUTA, COMMITTEE CHAIR

WILLIAM C. KEEL (ADVISOR)

JIMMY A. IRWIN

MIN S. YUN

DEAN M. TOWNSLEY

PATRICK A. TOALE

A DISSERTATION

Submitted in partial fulfillment of the requirements
for the degree of Doctor of Philosophy
in the Department of Physics and Astronomy
in the Graduate School of
The University of Alabama

TUSCALOOSA, ALABAMA

2013

Copyright Aparajita Sengupta 2013
ALL RIGHTS RESERVED

ABSTRACT

We present our data and results from panchromatic photometry and optical spectrometry of the nearest filamentary large scale structure, SuperGroup Abell 1882. It is a precursor of a cluster and is an inevitable part of the narrative in the study of galaxy transformations. There has been strong empirical evidence over the past three decades that galaxy environment affects galaxy properties. Blue disk galaxies transform into red bulge-like galaxies as they traverse into the deeper recesses of a cluster. However, we have little insight into the story of galaxy evolution in the early stages of cluster formation. Besides, in relaxed clusters, several evolutionary mechanisms take effect on similar spatial and temporal scales, making it almost impossible to disentangle different local and global mechanisms. A SuperGroup on the other hand, has a shallower dark-matter potential. Here, the accreting galaxies are subjected to evolutionary mechanisms over larger time and spatial scales. This separates processes that are otherwise superimposed in rich cluster-filament interfaces. We find that the galaxy color and morphology tie very strongly with local galaxy density even in a complex structure like Abell 1882. We identify the projected radial distance from the assumed center as a second order evolutionary driver. Our major results indicate that there is a strong dependence of galaxy transformations on the galaxy mass. We have found the thoroughly quenched low mass galaxies confined to the groups, whereas there are evidences of intermediate mass quenched galaxies even in the far

outskirts. We conclude that mass-dependent evolutionary mechanisms affect galaxies at different spatial scales. We propose harassment and/or ram-pressure stripping near or inside the high density, high velocity dispersion regions near the groups; and mergers as the mechanism for the intermediate mass quenched galaxies at the low density, low velocity dispersion outskirts. We also identify a starburst population preferentially occurring within the filaments, at least a subset of which must be progenitors of the quenched galaxies at the core of Abell 1882, indicating a higher degree of preprocessing within the filaments as compared to that in the field. The starburst galaxies and post-starburst galaxies exhibit a spatio-temporal sequence.

DEDICATION

I dedicate this dissertation to my Parents, my husband Joydeep, and my sister Dipanwita. Thanks for all the fish!

ACKNOWLEDGMENTS

The past few years spent towards the completion my PhD degree have been the most challenging and interesting learning phase of my life. I thank the Physics Department, University of Alabama, for making my graduate school experience memorable. The Department and its members will always have a special place in my heart.

First and foremost, I would like to express my heartfelt gratitude to my advisor Dr. William C. Keel whose scientific insight and intuitive understanding of astronomy have shaped and guided my own understanding of the subject. It has been a privilege to work under his guidance and mentorship. The long discussions with my advisor which often span over a vast range of topics will always be some of the most cherished memories of my graduate school. He has encouraged me to work independently and has patiently heard even my most outlandish of theories and gently guided me towards the right direction. I wish to acknowledge his contribution in developing my scientific intuitions and further developing my love for the subject.

I wish to extend a very special thanks to my collaborator Dr. Glenn Morrison, without whose help and wonderfully drafted proposals this project would not have been possible. He has been a constant support and mentor during the completion of my thesis.

I thank my committee members who took time out of their busy schedule to read my thesis and suggest several crucial corrections, modifications and

additions. I thank Dr. Min Yun for making a long trip to Tuscaloosa for my defense. A lengthy, interesting discussion with him was extremely useful in getting additional insight in to this project. Dr. Jimmy Irwin has been a wonderful mentor throughout my graduate school and has drawn my attention to similar interesting work done in X-Ray. Discussions with him about various projects and ongoing research in similar X-Ray structures have been a valuable learning process for me. Dr. Buta, Dr. Townsley and Dr. Toale have spent valuable time going through my thesis in great details that helped in shaping my thesis.

I wish to thank Dr. Rogier Windhorst and Arizona State University for graciously funding my travel and lodging expenses during the MMTO/Hectospec observations. I also wish to thank Perry Berlind at the MMTO for his help during the observation. I also wish to thank the University of Alabama graduate school and Department of Physics and Astronomy for the Graduate Student Research Travel Support Fund and College of Arts Science Research Travel Grant which have made it possible for me to go to five different conferences during my graduate school and present my thesis work. I also wish to thank my friends and colleagues Deepti Vikram, Neha Pachauri, Mihoko Yukita and Anna Manning for their constant support.

I gratefully acknowledge the contribution of the archival data obtained from Galaxy And Mass Assembly (GAMA) survey, Sloan Digital Sky Survey (SDSS) and Galaxy Evolution Explorer (GALEX) survey for my thesis. GAMA that has been made possible by the efforts of staff at the Anglo-

Australian Observatory, and members of the Sloan Digital Sky Survey and UKIRT Infrared Deep Sky Survey teams. Funding for the SDSS and SDSS-II has been provided by the Alfred P. Sloan Foundation, the Participating Institutions, the National Science Foundation, the U.S. Department of Energy, the National Aeronautics and Space Administration, the Japanese Monbukagakusho, the Max Planck Society, and the Higher Education Funding Council for England. The SDSS Web Site is <http://www.sdss.org/>. The SDSS is managed by the Astrophysical Research Consortium for the Participating Institutions. The Participating Institutions are the American Museum of Natural History, Astrophysical Institute Potsdam, University of Basel, University of Cambridge, Case Western Reserve University, University of Chicago, Drexel University, Fermilab, the Institute for Advanced Study, the Japan Participation Group, Johns Hopkins University, the Joint Institute for Nuclear Astrophysics, the Kavli Institute for Particle Astrophysics and Cosmology, the Korean Scientist Group, the Chinese Academy of Sciences (LAMOST), Los Alamos National Laboratory, the Max-Planck-Institute for Astronomy (MPIA), the Max-Planck-Institute for Astrophysics (MPA), New Mexico State University, Ohio State University, University of Pittsburgh, University of Portsmouth, Princeton University, the United States Naval Observatory, and the University of Washington. GALEX (Galaxy Evolution Explorer) is a NASA Small Explorer, launched in April 2003.

Finally, I wish to thank the constants in my life, my Parents, my husband, Joydeep, and my sister, Dipanwita for being my rocks and encouraging and

supporting me through each and every step. I especially want to take this opportunity to let my mother know that without you none of this would have been possible.

TABLE OF CONTENTS

ABSTRACT	ii
DEDICATION	iv
ACKNOWLEDGMENTS	v
LIST OF TABLES	xii
LIST OF FIGURES	xiii
1. INTRODUCTION	1
1.1 Hierarchical Structure Formation In the Universe	2
1.2 Galaxy Evolution Within Large Scale Structures	4
1.3 Mechanisms Of Galaxy Transformations	7
1.4 Galaxy Transformations In Clusters, Groups And SuperGroup Complexes	8
1.5 SuperGroup Complex Abell1882	12
2. OBSERVATION AND DATA REDUCTION	15
2.1 Optical Data	16
2.2 GALEX Data	24
2.3 XMM Data	24
3. DETERMINATION OF SPECTROSCOPIC PARAMETERS	26
3.1 Star Formation History And Star Formation Rate Indicators	26
3.2 Effect Of Dust Obscuration	28

3.3 Recombination Emission Lines	29
3.4 UV Continuum	30
3.5 Thermal Infrared Emission	30
3.6 Combining The Tracers	32
3.7 Classifying Different Galaxies Based On Their Star Formation Histories	33
4. DETERMINATION OF PHOTOMETRIC PARAMETERS	36
4.1 Origin of Galaxy Bimodality	37
4.2 Color-Magnitude Diagram	39
4.3 Best Fits For Bimodal Distribution In the Galaxies	45
4.4 Color Derived Mass Plots	50
5 STRUCTURE DETERMINATION	53
5.1 Local Galaxy Density(Σ) Profile	53
5.2 Friends-Of-Friends Algorithm To Determine The Feeding Filaments	55
5.3 Caustic Diagram.....	60
6. RESULTS AND DISCUSSIONS.....	65
6.1 Optical Color Evolution Of Galaxies With Projected Radial Distance and Local Galaxy Density(Σ).....	66
6.2 Disentangling Local Galaxy Density (Σ) Effect And Projected Radial Distance Effect On Galaxy Transformations	83
6.3 Birth Rate Parameter Evolution Of Galaxies.....	83
6.4 Photometric Evolution And Spectral Data	93
6.5 Evolution of Mean Equivalent Width Of H α	102

6.6 Spatial Sequencing Of Spectroscopically Classified Galaxies	105
7. SUMMARY AND FUTURE WORK	111
REFERENCES	114

LIST OF TABLES

1. Upper and lower bounds of continuum for equivalent width	22
2. Number of galaxies obtained from different surveys	25
3. Spectral types of galaxies versus different star formation histories	34
4. Implied timescales for different wavelengths and colors	35
5. Fractional Number Of Galaxies In Optical	38
6. Fractional Number Of Galaxies In Optical And UV Colors.....	49
7. Mass Bins Of The Galaxies Defined for this work.....	51

LIST OF FIGURES

1. Model Inputs For Galaxy Evolution	5
2. Galaxy Luminosity Function	7
3. Galaxy Evolution In SuperCluster Vs SuperGroup Environment	11
4. An overlay of X-ray emission and galaxy positions in Abell 1882	13
5. XMM-Newton image of the Abell 1882.....	14
6. Redshift distribution of galaxy spectra	16
7. Determination of equivalent width using SPLOT	23
8. Stellar components.....	27
9. Values of 'a' for calculation of star formation rate.....	33
10. Color (g-r) - Magnitude Diagram	46
11. Color (u-r) - Magnitude Diagram	47
12. Color (NUV-r) - Magnitude Diagram.....	48
13. Color (g-r) – Mass Diagram.....	51
14. Color (u-r) – Mass Diagram.....	52
15. Color (NUV-r) – Mass Diagram.....	52
16. Morphology-density relation (Dressler, 1980)	54
17. Projected radial distance-local galaxy density of the galaxies.....	56
18. Friends-Of-Friends Algorithm	59
19. Friends-Of-Friends Detected Filaments.....	60
20. Confidence Level For Friends-Of-Friends Algorithm.....	61

21. Caustic diagram.....	63
22. Fractional numbers of (g-r) color - local galaxy density	68
23. Fractional numbers of (u-r) color - local galaxy density	69
24. Fractional numbers of (g-r) color - projected radial distance	70
25. Fractional numbers of (u-r) color - projected radial distance	71
26. (g-r) color - local galaxy density.....	73
27. (g-r) color - projected radial distance.....	74
28. Color-Magnitude Diagram for dwarf galaxies.....	75
29. (g-r) color - local galaxy density for dwarf galaxies.....	76
30. (g-r) color - projected radial distance for dwarf galaxies.....	77
31. (g-r) color-magnitude diagram for intermediate mass galaxies	78
32. (g-r) color - local galaxy density for intermediate mass galaxies	79
33. (g-r) color - projected radial distance for intermediate mass galaxies.....	80
34. (g-r) color - local galaxy density for high mass galaxies.....	81
35. (g-r) color - projected radial distance for high mass galaxies.....	82
36. Local galaxy density - projected radius relation for a narrow range of local galaxy density.....	84
37. (g-r) color – local galaxy density for optically red, blue and green galaxies within the constant density range.....	85
38. (g-r) color - projected radial distance for optically red, blue and green galaxies within the constant density range.....	86
39. Fractional numbers of (g-r) color - projected radial distance within the constant density range.....	87
40. B_{300} - local galaxy density	88
41. B_{300} - Projected Radial Distance	89

42. B_{1000} - local galaxy density	90
43. B_{1000} - Projected Radial Distance	91
44. Spatial location of the dwarf galaxies with very low birth rate parameter.....	92
45. Caustic Diagram of Abell 1882 with spectral data	94
46. Projected Radial Distance - local galaxy density Relation with spectral data.....	95
47. (g-r) Color-mass relation with post-starburst galaxies.....	96
48. (u-r) Color-mass relation with post-starburst galaxies.....	97
49. (NUV-r) Color-mass relation with post-starburst galaxies.....	97
50. (g-r) color – local galaxy density with spectral data.....	98
51. (g-r) color - projected radial distance with spectral data	99
52. (g-r) color - local galaxy density for dwarf galaxies with spectral data	100
53. (g-r) color - projected radial distance for dwarf galaxies with spectral data.....	100
54. (g-r) color - local galaxy density for intermediate mass galaxies with spectral data	101
55. (g-r) color - projected radial distance for intermediate mass galaxies with spectral data	101
56. EW($H\alpha$) plotted against birth rate parameter over past 300 Myrs.....	103
57. EW($H\alpha$) evolution with projected radial distance	104
58. EW($H\alpha$) evolution with local galaxy density	104
59. Spatial Distribution Of Starburst and Post-Starburst (k+a) Galaxies	106
60. Spatial Distribution Of Post-Starburst (k+a) Galaxies	107
61. Spatial Distribution Of Starburst and Post-Starburst (k+a) Galaxies For Low Mass Galaxies	108

62. Spatial Distribution Of Passive Galaxies	109
63. Spatial Distribution Of Starburst and Post-Starburst (k+a) Galaxies For Intermediate Mass Galaxies	110
64. Spatial Distribution Of Passive Galaxies For High Mass Galaxies...	110

1 INTRODUCTION

With deeper and more extensive panchromatic data available than ever before, study of evolution of galaxies is a rapidly growing field in astronomy. We aim at providing a detailed photometric and spectroscopic study of an over-dense region at a redshift of 0.1367, that is accreting galaxies primarily through the elongated filament-like structures, and is expected to eventually accrete enough mass to form a Coma-like cluster in 2 Gyrs. Section 1 is aimed at providing a backdrop and motivation for this work. Section 2 details the observations, data reduction and obtains a redshift constraint for the member galaxies of the structure under study, namely SuperGroup Abell 1882. Section 3 and 4 detail the various spectroscopic and photometric tracers of star formation history of the galaxies. In Section 3, we define and identify the passive, starburst and post-starburst galaxies. The post-starburst phase of galaxies is believed to be an important evolutionary link between the star-forming and nonstar-forming galaxies. They also have a very well constrained lifetime of 0.1-0.3 Gyr. Hence their locations within the system are expected to provide interesting spatial and temporal constraints on galaxy transformations. Galaxy colors are among the most direct diagnostics of star formation in a galaxy. In Section 4, we have defined galaxy colors based on various color parameters and discussed the usefulness of using different wavelengths to define the galaxy colors. In Section 5, we have obtained the local galaxy density of each galaxy using the recipe from [3]. We also identify the feeding filaments of the system with a Friends-of-Friends algorithm using the recipe from Huchra & Geller ([47]). Lastly in section 6, we tie up our photometric, spectroscopic and structural results and look for clues to galaxy transformation and identify the major drivers of galaxy evolution in the early stages of cluster formation.

1.1 Hierarchical Structure Formation In the Universe

Clusters grow by accretion through filaments, and accreted galaxies undergo transformations due to environmental effects caused by local galaxy density (Σ) as well as the underlying large scale structures. In order to reconstruct the galaxy transformations in the context of metallicity, color, morphology, star formation history, AGN activity etc., one needs a panchromatic approach to study the galaxy transformations as a function of its environment, and compare them with the growing body of predictions from simulations.

The past twenty years of simulations and observations support the paradigm of a Lambda Cold Dark Matter (Λ CDM) hierarchical structure formation in the Universe driven by gravity. It is presently believed that the structures we see in the Universe today have their seeds in the primordial density fluctuations in the early Universe. These tiny and gravitationally unstable primordial fluctuations grew and amplified during the inflationary epoch. During this epoch, the nascent Universe underwent an exponential expansion which later caused matter to collapse under gravitational instability. Sub-galactic mass dark matter haloes collapsed locally and without dissipation, into the perturbations, and separated out from the large scale expansion or the Hubble flow of the Universe. These haloes underwent mergers to form progressively larger haloes (eg. [80]). The baryonic matter fell into the deep gravitational potential wells of the halos and eventually cooled and compressed to form the complex network of low density voids, and high density clusters and filaments observed at the present redshift. The galaxies undergo an accelerated evolution when they enter the harsh denser supercluster environments, as compared to the galaxies that reside in low density field regions. A supercluster environment consists of an intricate network of

filaments with clusters/proto-clusters forming at their nodes ([48]). Clusters constantly accrete small galaxy groups through filaments along preferred directions and grow in size and in richness with time. Galaxies mostly form in groups on this filamentary network where they are processed for billions of years before they are funneled into the clusters. The clusters assemble and grow by complex interactions between dark matter, diffuse gas, and thousands of individual galaxies. The physical details of these interactions are currently not fully understood. There are indications that the large scale structures play a very significant role in the star formation and quenching mechanisms in galaxies. The role of the inner regions of clusters in galaxy evolution has been extensively studied because most of the spectroscopically targeted galaxies tend to be cluster members. But the same is not true for filaments. Besides, gas in the filament is too thin to see in X-ray emission and too hot to see in absorption. Hence, even though our understanding of galaxies within the cluster potential during the later stages of their evolution has made significant strides, the same is not true for the galaxy evolution in the far outskirts of the clusters and deep inside the filaments. de Vaucouleurs identified the first supercluster (the Local Supercluster) in 1953 ([23]). This was followed by a catalogue of similar structures detected by Abell ([1]) using Palomar Observatory photographic plates. Later, wide field surveys like Two degree Field Galaxy Redshift Survey (2dFGRS) and Sloan Digital Sky Survey (SDSS) helped in detailed studies of these structures and their properties.

The adopted cosmology for this work is $H_0 = 71 \text{ kms}^{-1} \text{Mpc}^{-1}$, $\Omega_M = 0.27$ and $\Omega_\Lambda = 0.73$ as recommended by Wilkinson Microwave Anisotropy (WMAP) analysis. Here, H_0 is the Hubbles constant at redshift z_0 (i.e. at the present time), Ω_M is the mass density of the Universe and Ω_Λ is effective mass density of dark energy

in the Universe. h is scaled Hubbles constant and is given by $H_0/(100 \text{ km/s/Mpc})$.

1.2 Galaxy Evolution Within Large Scale Structures

In order to understand galaxy formation and growth, it is not sufficient to understand its constituent star formation, stellar evolution, feedback mechanisms and gas dynamics alone. One also needs to connect the galaxy evolution in the context of the hierarchical structure formation and the large scale structures that host the galaxies. The galaxy model calculations must therefore combine inputs from various cosmological parameters in the form of the angular power spectrum of the anisotropy of the cosmic microwave background, dark matter halo mergers etc., as well as from the evolution of stellar components, and predict the observed morphologies, luminosity function, mass-to-light ratios of the galaxies in the local Universe, metallicities, color distribution, star formation history, birth rate parameters etc.

Even after decades of observations, it is not clear whether a single dominant mechanism or a combination of multiple mechanisms is responsible for galaxy transformation. Hence it is necessary to investigate environments where the galaxy density, intra-cluster medium (ICM), dark matter halo density and projected radial distance from the center are not as tightly coupled as in relaxed clusters where ram pressure stripping appears to be the most dominant mechanism for galaxy transformation in its supercluster environment.

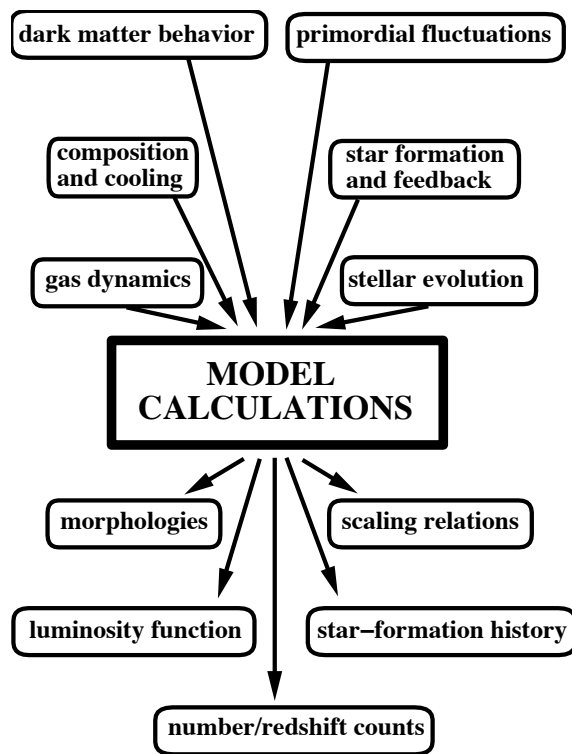


Figure 1: Model Inputs For Galaxy Evolution adopted from a figure by Carlton Baugh

1.2.1 Galaxy Luminosity Function

The luminosity function is the number distribution of galaxy luminosities or the space density of galaxies. It is a fundamental observable of galaxies and contains information about galaxy formation and transformations, both secular and environmental. Galaxies have an enormous range in mass and luminosity that can span over 10^6 orders of magnitude, the faintest dwarfs being $\approx 250,000 L_{\odot}$, whereas the largest cD galaxies at the center of the richest clusters are as bright as $2 \times 10^{12} L_{\odot}$. It turns out that the Schechter function is a good description of galaxy populations in a wide range of environments from the rarely populated fields to well populated rich clusters. ([87], [33]). The number of galaxies decreases monotonically with increasing galaxy luminosity. This agrees well with the Press-Schechter theory which states that the number density of massive objects like clusters is expected to drop off exponentially at high masses in a hierarchical mass assembly scenario ([87]). The Schechter function has the following functional form in terms of luminosity (L):

$$\phi(L)dL = n_{\star} \left(\frac{L}{L_{\star}} \right)^{\alpha} \exp \left(-\frac{L}{L_{\star}} \right) d \left(\frac{L}{L_{\star}} \right) \quad (1)$$

where, L_{\star} is the luminosity that separates the steep faint end slope and high luminosity end of the slope and $L_{\star} \approx 10^{10} L_{B\odot} h^{-2}$. If $L < L_{\star}$, the luminosity function exhibits a power law $\phi(L) \propto L^{\alpha}$ where $\alpha \approx -0.8$ to -1.3 . At high luminosity, i.e. $L > L_{\star}$ the function has an exponential cutoff, $\phi(L) \propto e^{-L}$. This implies that very luminous galaxies are very rare compared to low luminosity galaxies. n_{\star} is a normalization set at L_{\star} where $n_{\star} \approx 0.02 h^3 Mpc^{-3}$ for the total galaxy population. While computing the luminosity function it is important to specify the

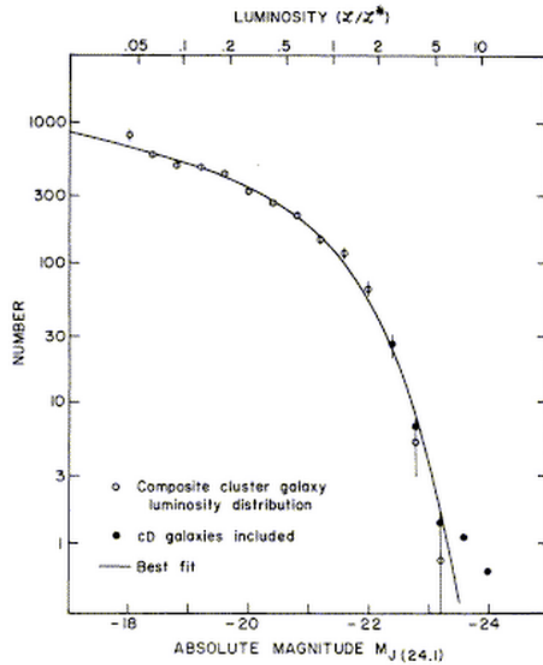


Figure 2: Galaxy Luminosity Function: Best fit of analytic expression to observed composite cluster galaxy luminosity distribution for 12 Abell clusters. Filled circles show the effect of including cD galaxies in the composite ([92])

galaxy environment. The galaxy luminosity function is used in Chapter 5 for the Friends-of-Friends algorithm to determine the feeding filaments in the SuperGroup environment of Abell 1882.

1.3 Mechanisms Of Galaxy Transformations

The past three decades of galaxy evolution studies show strong empirical evidence that galaxy environment affects galaxy properties in terms of their color, star formation capabilities, morphologies, dynamics etc. The environmental mechanisms that cause forced evolution in galaxies can be classified into three broad categories. Galaxies can interact with the gravitational potentials of clusters or other galaxies to give rise to harassment (e.g., [89], [74], [75]) or mergers. Ha-

rassment occurs at high density (notably cluster cores), high speed environments where a galaxy can be subjected to several weak, fast encounters. The characteristic time scales required for interaction are usually shorter than characteristic time scales required for mass to fall back into the galaxy. Hence the galaxy may end up losing its mass over time and the star formation is quenched eventually (e.g., [63], [5]). This process mainly changes the morphologies of the low mass galaxies. Galaxies mergers on the other had occur in low density, low speed environments, and can also transform disk-like galaxies into bulge-dominated galaxies by destroying the disk structure(e.g., [101], [49]). Tidal galaxy-galaxy interactions on the other hand can tidally compress a galaxy's envelope of gas, increasing the star formation rate. It causes galaxy starvation that removes some of the hot gas halo enhanced by the tidal interaction leading to late quenching of star formation (e.g., [35]). The third type of mechanism involves galaxy - IntraCluster Medium (ICM) interaction. As the galaxy enters the ICM of a cluster, if the ICM wind exceeds the gravitational restoring pressure of a galaxy, the outer gas shell will be blown away. This is known as ram pressure stripping of galaxies (e.g., [43], [88]), [108], [56]).

1.4 Galaxy Transformations In Clusters, Groups And SuperGroup Complexes

Study of galaxy transformations in the far outskirts of a dominant cluster potential has been challenging owing to the fact that it requires a very wide field for the inclusion of their feeding filaments at a reasonably low redshift, to enable tracing of evolutionary effects within individual galaxies. Presently, we are still converging on effective tools to understand the early formation and evolution of galaxies. One of the missing links in the narrative is the role of galaxy transfor-

mations in clusters/filament precursors. They provide us with a rare glimpse into the early galaxy transformations that are otherwise difficult to disentangle once the cluster-centric mechanisms begin to dominate. Proto-clusters have very shallow, and sometimes highly unvirialized potential wells, and thus are often hard to detect. Their highly clumpy nature also means that quantifying their velocity structure is extremely tricky.

Hydrodynamical simulations show that cluster formation by galaxy accretion is not a simple spherical shell collapse scenario. It is highly episodic and clumpy, where the galaxies are accreted mostly in the form of groups, along preferred directions (reference). These groups/clumps are usually in different stages of virialization during the accretion. With extensive spectrometry and photometric imaging of galaxies in the cluster outskirts, one can ideally map the radial locations of these transformations onto a time sequence. In relaxed clusters, several evolutionary mechanisms act on similar spatial and temporal scales, making it almost impossible to disentangle different local and global mechanisms such as projected radial distance, local galaxy density and intra-cluster medium density. A proto-cluster on the other hand, has a shallower dark matter potential. Hence, the accreting galaxies are subjected to evolutionary mechanisms over larger time and spatial scales. This can separate processes that are otherwise superimposed in rich cluster-filament interfaces, and hence facilitate our understanding of filament-cluster core interaction at a different dynamical scale as compared to a more evolved and relaxed system. Since proto-clusters at high redshifts are hard to detect, and not many have been observed at lower redshifts, we have very little understanding of the galaxy transformations occurring in these environments. However, the galaxy bimodality that we see in the present day clusters might

trace back to the evolutionary mechanisms in the early phases of cluster formation. This would make these proto-cluster environments an inevitable part of the narrative in the study of galaxy evolution, in addition to telling us what already happened in the past of a rich cluster like Coma. Even with only a handful of proto-clusters observed at low redshifts, it is clear that these proto-clusters can be diverse enough, leading to the idea that there may be several pathways to a virialized cluster, a SuperGroup being one such pathway. It is a group of groups of galaxies that are in the process of coalescing and will eventually accrete enough mass to form a cluster [16].

There are three known low- z SuperGroups, namely Abell 1882 ($z = 0.138$), Eridanus ($z = 0.006$) and SG1120-1202 ($z = 0.37$). SuperGroups Eridanus and SG1120-1202 show an overabundance of early-type galaxies indicating that morphological preprocessing similar to rich clusters has already taken place in these early systems, and possibly within the filaments ([54], [?]). Hence the morphology density correlation in these structures seems to be sealed even before the virialization of the structures. SG 1120-1202 detected by Gonzalez et al. ([41], is more similar to Abell 1882. It has $M = 5.3 \times 10^{14} M_{\odot}$, at a redshift $z \sim 0.4$, and is made up of at least four individual groups, each of which has an extended X-ray halo, indicative of dynamically mature group structures. The correlation between spectral properties of galaxies and the local galaxy density relation is established in this system as a result of galaxy-galaxy mergers in groups prior to the cluster assembly.

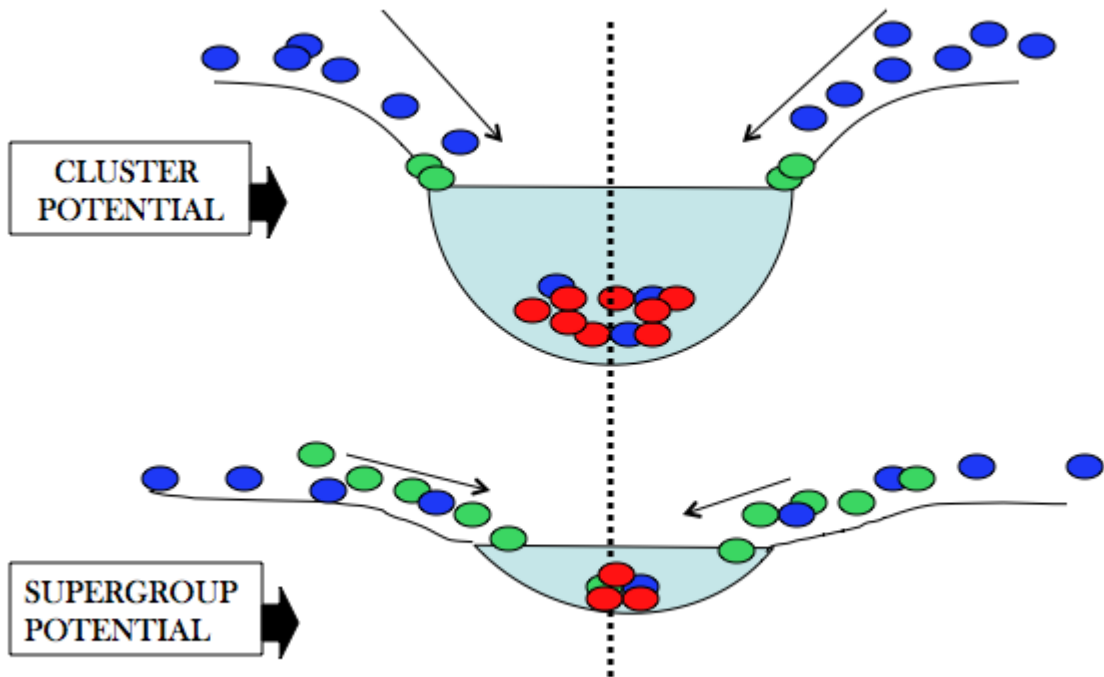


Figure 3: Galaxy Evolution In SuperCluster Vs SuperGroup Environment: In relaxed clusters, several evolutionary mechanisms act on similar spatial and temporal scales, making it almost impossible to disentangle different local and global mechanisms (top). A SuperGroup has a shallower dark matter potential and the accreting galaxies experience evolutionary mechanisms over larger time and spatial scales (bottom), thus separating processes that are otherwise superimposed in rich cluster-filament interfaces.

1.5 SuperGroup Complex Abell 1882

The SuperGroup Abell 1882 hosts a highly diverse filament-type large scale structure environment. Gomez estimates the mass of the system to be $\sim 2 \times 10^{14} M_{\odot}$ by comparing the kinematical data with N-body numerical simulations, and predicts that in about 2 Gyrs the system will coalesce into a Coma-like cluster ([39], also see, [41]; [16]). It has a redshift of $z = 0.1367$ and lies approximately at $\alpha = 14\text{h}14'39.9''$ and $\delta = -00^{\circ}19'57''$ in the constellation of Virgo. It covers a much wider area than most previously observed intermediate-redshift clusters. It is still accreting its mass and is highly unvirialized. Hence, the galaxy density and projected structure-centric distances are sufficiently decoupled to study the galaxy evolution mechanisms in different environments within the system. This provides a unique opportunity to explore the formation process of a cluster of galaxies from its original group/filament precursors.

Abell 1882 is made up of at least three high-density groups which are interconnected via filaments, all of which have been detected in X-ray (Figure 4 and 5). Two of the three components are on a collision course along the line-of-sight and may currently be undergoing core-crossing. Each of the three galaxy groups appear to lie within 1 - 1.5 r_{virial} (virial radius) of the other two groups. This leads to a central dense region between the three major groups, where the outer gaseous halos of the groups overlap. This region is denser than the outskirts, but more tenuous than the groups themselves. The mass ratio between group A and group C is $\sim 2:1$, and there is no obvious X-Ray emission between these two groups. In a merger scenario, group A and group C would exhibit a severely retarded sub-clump motion, and are unlikely to have travelled the presently observed large distance of $R_{proj} \approx 2$ Mpc after a head-on collision.

Although the temperature distributions are asymmetric, a recent core passage merger of these two groups is unlikely since there is no significant observable distortion of X-Ray morphology, shocks, cold fronts or significant offsets between X-Ray and optical substructures like the bullet cluster. Bullet cluster consists of two colliding galaxies and hence has extremely clumpy and diverse X-Ray environment similar to that of Abell 1882. Hence, although there is a subtle sign of interaction, they are likely falling into each other for the first time (See Matt Owens, TAIPAN workshop, 2012). All these factors strongly indicate that although Abell 1882 contains dynamically mature groups with their own individual well formed X-Ray structures, it is nonetheless a dynamically young system.

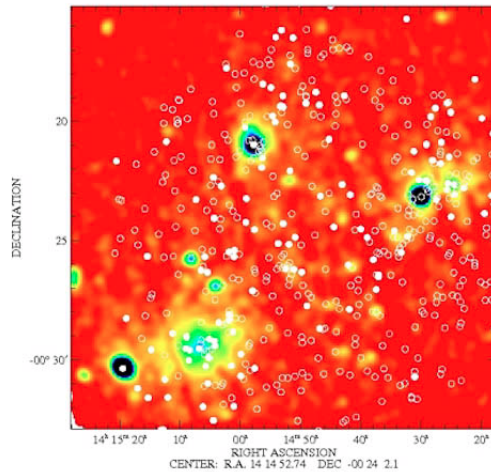


Figure 4: An overlay of extended X-ray emission originating from at least three distinct groups of galaxies and the positions of the galaxies in Abell 1882 ([40])

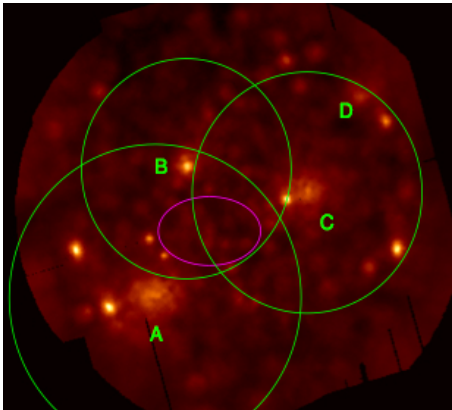


Figure 5: Composite MOS1+MOS2+PN image of the Abell 1882 system from XMM-Newton data, showing the four X-ray clumps at $z=0.139-0.140$ associated with galaxy groups A, B, C, and D. Green circles represent the virial radius of each of the three larger X-ray clumps (from Evrard et al. 1996 [30], assuming $r_{virial} = 2.75(T/10keV)^{0.5}$ for $H_0 = 71 \text{ km s}^{-1} \text{ Mpc}^{-1}$ using the measured X-ray temperatures quoted in the text). The magenta oval represents the overlap region where excess X-ray emission was detected. (J. Irwin, private communication.)

2 OBSERVATION AND DATA REDUCTION

We draw our galaxy samples for Abell 1882 from six primary sources. We have obtained optical spectroscopic data from MMTO/Hectospec at Mt. Hopkins. Based on the redshift distribution of these galaxies we have defined the SuperGroup members of Abell 1882. We have complemented this catalog with data from wide-field surveys like the Sloan Digital Sky Survey (SDSS) and the Galaxy And Mass Assembly (GAMA) survey. We also have data from targeted observation using the Gemini Multi-Object Spectrograph (GMOS) on Gemini South (PI: Miller C., Gomez P.L., 2008). We have an additional WIYN-Hydra data set (PI: Owen), which is a filler program and hence not sufficiently deep for this study. We found that the signal-to-noise ratio (SNR) was too low to extract reliable spectroscopic redshifts. Hence these data were excluded from the final catalog. We have spectroscopic redshifts for Gemini Multi-Object Spectrograph (GMOS) from collaboration. However, we do not have the spectra. Hence, the GMOS data have been used only for photometric and structural analysis. We have also procured additional redshifts from the NASA/IPAC Extragalactic Database (NED). We then matched the final optical galaxy catalog with the $24\mu\text{m}$ data from the Spitzer space telescope (PI: Morrison G. E. [76]), and FUV/NUV data from the Galaxy Evolution Explorer (GALEX) archive.

Our final galaxy catalog containing the Abell 1882 SuperGroup members has 526 galaxies, constrained in a redshift range of $0.133 \leq z \leq 0.144$ (Fig. 2), within a radius of 1.05° or 9.2232 Mpc from the assumed center of Abell 1882 at RA = 213.71° and Dec = -0.41° .

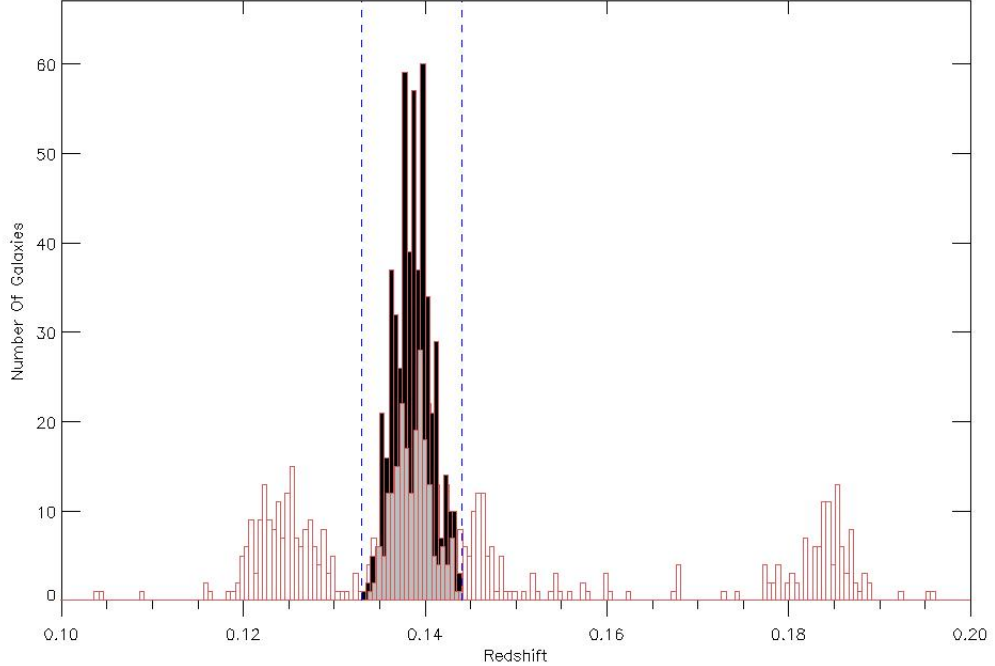


Figure 6: Redshift distribution of 1500 galaxy spectra (in pink) obtained using the Hectospec constrains the SuperGroup Abell 1882 galaxy catalog within $0.133 < z < 0.144$. Black solid histogram shows all the member galaxies obtained from Hectospec, GAMA survey, SDSS archive, NED and GMOS preselected based on the redshift cuts obtained from Hectospec spectra. Dashed vertical lines mark the redshift boundaries for Abell 1882.

2.1 Optical Data

Integrated photometric and spectroscopic properties of galaxies are powerful diagnostics of galaxy formation and evolution. In most galaxies, these integrated properties are dominated by disk and bulge and have very little contribution from the nucleus of the galaxy, in both continuum and emission lines. Important galaxy statistics like color bimodality, morphological classification, stellar mass estimation etc. can be obtained from photometric imaging. Integrated spectroscopic

properties on the other hand can constrain the star formation rate, star formation history, ionization mechanisms, chemical abundance, dust content and also stellar mass (e.g., [53], [79], [102], [15]).

2.1.1 MMTO/Hectospec

Hectospec is a multi-object, moderate-dispersion (50 to 75 Å/mm) optical spectrograph with 300 fiber probes. These probes are aided by a pair of six-axis robots to position them at the prime focus (f/5) of the converted MMT in 300 seconds, with an accuracy of $\approx 25 \mu\text{m}$. Each fiber with its 250 μm diameter, subtends an angle of 1.5" in the sky. Consecutive fibers can be placed at a minimum distance of 20". A refractive corrector positioned at f/5 focus yields a 1° field of view optimized for fiber-fed spectroscopy. It covers about 1° or 8.784 Mpc at the mean redshift of Abell 1882 ($z \approx 0.139$). This field is large enough at that redshift to include the SuperGroup and the infall region along with its feeding filaments, and samples a vast range of galaxy environments in a single pointing.

a. Target Selection

We have targeted the galaxy population down to $r \leq 21 (M_\star + 4)$ and $\log(M_\star/M_\odot) \geq 8.23$. This has enabled us to sample faint, low mass end of the galaxy spectrum out to a very large radius and deep into the feeding filaments, thus probing galaxy transformations in the far outskirts of the SuperGroup. This wide sampling of Σ as well as underlying large scale sub-structures facilitates the disentangling of the dominant drivers for galaxy transformations. It also enables us to identify the spatial locations and nature of the environmental mechanisms on galaxies at various mass ranges. Hence Hectospec is very well suited to study

the transformations due to environmental effects down to the very faint dwarf galaxies at this redshift.

b. Redshift Determination

We have determined the redshift of the galaxies using two independent methods and compared them with those obtained from the MMT pipeline (Figure 6).

c. Fourier Cross-Correlation (FXCOR)

We have used FXCOR, which is a task within the RV package in IRAF, developed by Tonry & Davis and distributed by the National Optical Astronomy Observatories (NOAO), Tucson, Arizona. FXCOR correlates a spectrum of unknown redshift and velocity dispersion, i.e. the object spectrum, to that of a template spectrum at zero redshift and a known velocity. FXCOR returns values for the heliocentric rest frame of the object spectrum, (where the rotation of Earth and orbital motions have been removed from the measured velocity) from the location of the cross-correlation peak as well as the FWHM of the peak, which is related to the velocity dispersion. It is important to note that FXCOR returns relative redshifts as default. We have applied FXCOR for the part of the spectrum shortward of atmospheric oxygen line (5577\AA) which includes a sufficient number of well-defined emission and absorption lines to provide an accurate galaxy redshift. The template spectra have been obtained from the Kennicutt atlas ([57]), which includes integrated spectrophotometry of 55 nearby galaxies of diverse morphological properties. The observations cover a spectral range of 3650\AA - 7100\AA with a large aperture, moderate resolution ($15\text{-}25\text{\AA}$), using the Intensified Reticon Scanner (IRS) on the 0.92 m telescope at Kitt Peak National Observatory

(KPNO). The observations also provide the continuum energy distributions and emission line fluxes. In order to measure the weak absorption/emission lines the long-slit drift scanning technique has been employed and a higher resolution data (5 -7Å) have been obtained using the 2.3 m Steward Observatory telescope. These spectra have been corrected for atmospheric extinction only, since these galaxies are located at high galactic latitude, where galactic reddening is negligible. The templates selected for comparison are as follows: NGC 3379 for absorption line galaxies (E, S0), NGC 6181 for emission line galaxies (Sc), NGC 7714 for starburst galaxies and NGC 4449 for post-starburst (k+A) galaxies.

d. Measuring Redshift Using The SPLOT Task

We compared the wavelengths of significant absorption and emission lines like $H\alpha$, $H\beta$, [NII], CaII K & H, [OII] and [OIII] with that in air at rest frames as described in the SDSS archive, to manually determine the redshift of each of the 1500 galaxies individually. We then compared these redshifts with that obtained from FXCOR as well as from the MMT pipeline. Values of redshifts obtained for the galaxies employing different techniques are consistent.

2.1.2 The Galaxy And Mass Assembly (GAMA) Survey

The Galaxy And Mass Assembly (GAMA) survey is a wide-area spectroscopic survey for about 300,000 galaxies for low to intermediate redshift galaxies, with a primary focus on large scale structure and galaxy formation and evolution. It is a panchromatic photometric and spectroscopic dataset which draws on and builds upon the already existing wide-field spectroscopic surveys like the Sloan Digital Sky Survey (SDSS), the 2dF Galaxy Redshift Survey (2dFGRS), and the

Millennium Galaxy Catalogue (MGC). It surveys an area of $\approx 280 \text{ deg}^2$ in the sky, down to an r-magnitude < 19.8 and M^*+2 . In addition, it has a high spectroscopic completeness of 96% as compared to $\sim 65\%$ in SDSS in the dense regions ([105]), thus allowing the study of structures like Abell 1882. The spectrometry has been carried out with the AAOmega spectrograph on the Anglo-Australian Telescope (AAT).

GAMA survey uses a dual-beam system, with a Blue arm that covers the full wavelength range of 370nm to 850nm, and a Red arm that covers the full wavelength range from 470nm to 950nm using a redder dichroic at low resolution and are tunable over these ranges at higher resolutions. The AAOmega spectrograph is fed by either the Two Degree Field (2dF) multi-object system or the SPIRAL integral field unit. The Two Degree Field system is a complex astronomical instrument, which can yield up to 392 simultaneous spectra of objects anywhere within a two degree field on the sky. It consists of a wide-field corrector, an atmospheric dispersion compensator and a robot gantry which positions optical fibers to $0.3''$ on the sky. A tumbling mechanism with two field plates allows the next field to be configured while the current field is being observed.

a. Target Selection

We have obtained our data from the GAMA first data release. This includes downloadable catalogues containing the pre-existing redshifts, self-consistent $u-K$ photometry and raw spectra for the majority of year 1 data. We pre-selected galaxies from between a redshift range of $0.133 \leq z \leq 0.144$, within a radius of 0.75° from the assumed center of Abell 1882. This has directly led to the coverage of the region under study up to 1.05° or 9.2 Mpc, and has added 170 new member

galaxies to our catalog. The flux scale of each has been normalized to be consistent with the SDSS data.

b. Determination of Equivalent Width Of Emission And Absorption Lines And Flux Reduction

The spectra are converted into one dimensional spectra and the equivalent widths (EW) of the emission and absorption lines have been obtained using the SPLOT function in IRAF in batch mode. The lines are fitted using Gaussian profiles (Figure 7). The continuum for each line has been selected using the recommendation in the SDSS archive. Only those lines which are within $\pm 10\text{\AA}$ from the recommended line centers are considered as detections. Several spectra from the GAMA survey have low S/N in the lower wavelength regime and hence detection of $H\delta$ at 4100\AA and $[OII]$ at 3726\AA are not reliable for those spectra and have been discarded. Manual measurements have been undertaken for the EW that were obtained incorrectly by the IRAF script due to discontinuity in the continuum of the spectra and/or low S/N.

TABLE 1: Upper and lower bounds of continuum for equivalent width:

Line Name	Line Center (\AA)	Lower bound (\AA)	Upper bound (\AA)
OII 3726	3726.032	3717.0	3737.0
H δ	4101.734	4092.0	4111.0
H γ	4340.464	4330.0	4350.0
H β	4861.325	4851.0	4871.0
OIII 5007	5006.843	4997.0	5017.0
NII 6548	6548.040	6533.0	6553.0
H α	6562.800	6553.0	6573.0
NII 6584	6583.460	6573.0	6593.0

By definition, line flux = equivalent width \times local continuum flux. The continuum fluxes have been retrieved by averaging across pixel regions on the z_0 spectra and multiplying by $(1+z)$. This was done in batch mode using the IMSTAT task in IRAF.

The spectra for the GAMA survey have been scaled centered at 6300\AA (6200\AA - 6400\AA) to match that of the MMT for consistency. Pixel number for a given wavelength (P) was obtained using the formula $P = \text{CRPIX1} + (\lambda - \text{CRVAL1}) / \text{CD1.1}$, where CRPIX1 is the reference pixel coordinates, CRVAL1 is the reference data coordinates corresponding to CRPIX1, and CD1.1 denotes the dispersion for spectral data. These are FITS header keywords and have been obtained from the header file.

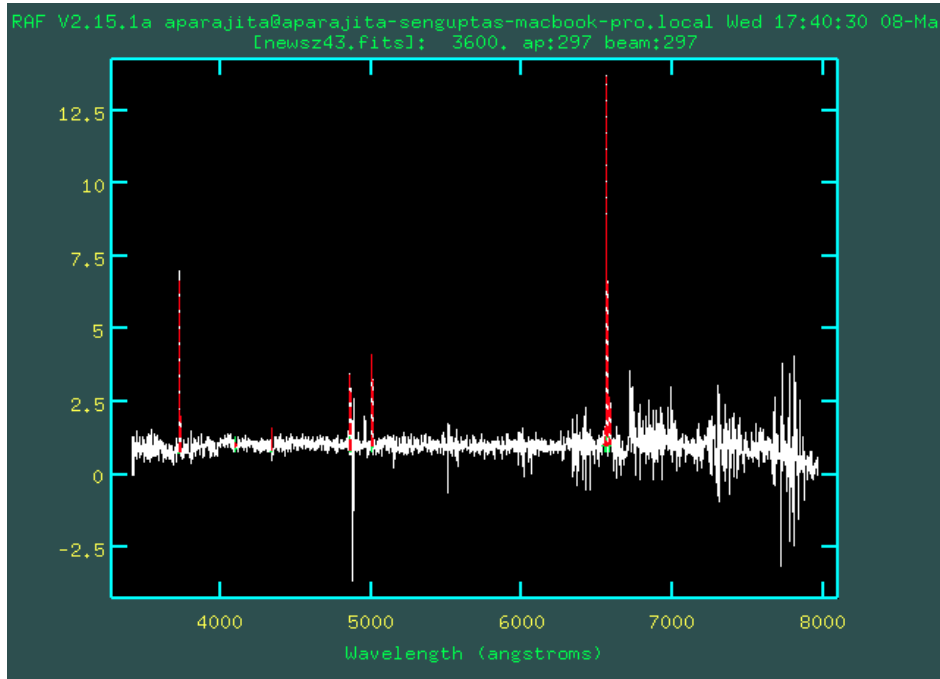


Figure 7: Determination of equivalent width using SPLIT

2.1.3 Sloan Digital Sky Survey (SDSS)

The Sloan Digital Sky Survey (SDSS) is a wide-field survey and has obtained deep, panchromatic images augmented by spectra for more than 930,000 galaxies. We have used archival data from Data Release 7 (DR7) which is the final data release of SDSS-II, and an extension of the original SDSS consisting of the subprojects The Legacy Survey, SEGUE and a Supernova survey. We have also used data from Data Release 8 (DR8) from the third Sloan Digital Sky Survey (SDSS-III), which is a program of four new surveys using SDSS facilities. DR 8 contains all images from the SDSS telescope and includes measurements for nearly 500 million stars and galaxies, and spectra of nearly two million. We retrieved galaxy data centered at $ra = 213.71^\circ$, $dec = -0.41^\circ$ with a radius of $45'$ within a redshift $0.133 < z < 0.144$. The SDSS spectroscopic sample is incomplete for

galaxies with nearby neighbors. This is due to the fact that the fibers cannot be close together. This makes it harder to define groups, and careful corrections are needed for the spectroscopic catalogues.

2.2 GALEX Data

The NUV and FUV data have been obtained from the GALEX archive selected within $5''$ radius of each optical galaxy. Galactic extinction in the UV has been calculated using the recipe from [?] using the following formulae,

$$A_{BV} = \left(a(x) + \frac{b(x)}{R_v} \right) \times E(B - V) \quad (2)$$

where, R_v parametrizes the extinction law and x is the wavelength. For most locations in the Milky Way, $R_v=3.1$ is a good value and galactic extinction is $E(B-V) = 0.041$ mag towards Abell 1882. We consider $x= 1350\text{\AA}$ for FUV and $x= 2800\text{\AA}$ for NUV. We found the galactic extinction for NUV to be equal to 0.08 mag and that of FUV to be 0.11 mag.

2.3 XMM Data

In Fig 4, the measured temperatures for clumps A, B, C, and D [Fig. 4] are 2.9 ± 0.2 , 1.5 ± 0.6 , 1.8 ± 0.16 , and 1.6 ± 0.6 keV, respectively, and 0.5–7.0 keV luminosities of $(2.4, 1.3, 1.2, 0.23) \times 10^{43} \text{ergs s}^{-1}$, respectively. Not all the groups are relaxed, cool core groups. The X-ray emission of Group A is broad and extended, and shows no evidence for a drop in temperature at the center, indicating this is a non-cool core group. Furthermore, the brightest group galaxy is offset from the centroid of the X-ray emission by $25''$ (60 kpc). Group B is much more com-

pact, although not point- like (as verified from existing archival Chandra data) and cooler in the center, indicative of a cool core group. Group C appears broad and somewhat distended, although the data are not sufficient to determine any temperature structure. Group D is a factor of five fainter and is located near the edge of the XMM-Newton FOV (it falls between the ACIS-S and ACIS-I arrays in existing *Chandra* data). At the center of Clump D is a small collection of galaxies with a central luminous elliptical galaxy with a spectroscopic redshift of 0.140. In addition to the four X-ray clumps, there is evidence for excess X-ray emission in the region between the three main clumps. The X Ray analysis is due to J. Irwin (private communication).

TABLE 2: Number of galaxies obtained from different surveys:

Survey	Galaxies with known z	Galaxies with spectra
MMT - Hectospec	210	210
Galaxy And Mass Assembly	170	149
Sloan Digital Sky Survey	85	78
Gemini Multi-Object Spectrographs	38	0
NASA/IPAC Extragalactic Database	23	0
Total	526	437

The last column denotes the number of galaxies for which we have the actual spectra.

3 DETERMINATION OF SPECTROSCOPIC PARAMETERS

Star formation is one of the most fundamental processes driving the evolution of galaxies. It processes and depletes the dust and gas in the galaxies, causing the metal enrichment of the interstellar (ISM) and intergalactic medium (IGM). It also regulates the radiative and mechanical feedback within the ISM and IGM. Hence, star formation and quenching are some of the most direct ways in which the environmental changes are manifested in the galaxies. Unlike the Milky Way, study of individual stars in the star-forming regions is limited even for local galaxies. Hence, it is imperative to study the star formation integrated over entire galaxies, that reflects the cumulative conversion of cold baryonic matter collapsing and fragmenting into stars, and the consequent electromagnetic energy radiated by the stars or re-radiated due to its interaction with dust particles.

3.1 Star Formation History And Star Formation Rate Indicators

A precise calculation of star formation rates (SFR) and star formation histories (SFH) of the galaxies as they trace different galaxy environments is imperative to understanding the dynamics of underlying framework of the Universe. In order to determine the SFR and SFH, we have taken a multi-band approach. This will help us obtain complementary information about the physical state of the clusters and mitigate the systematic errors in any single measurement.

SFR indicators for galaxies range across the spectrum from the X-ray to the radio wavelengths. The most energetic emissions are from X-Ray binaries and the hot ISM. The UV through NIR bands trace direct photospheric light from the stars. The IR traces the dust-processed star light. Synchrotron radiation in radio wavelengths probes the non-thermal emission, possibly from particles accelerated

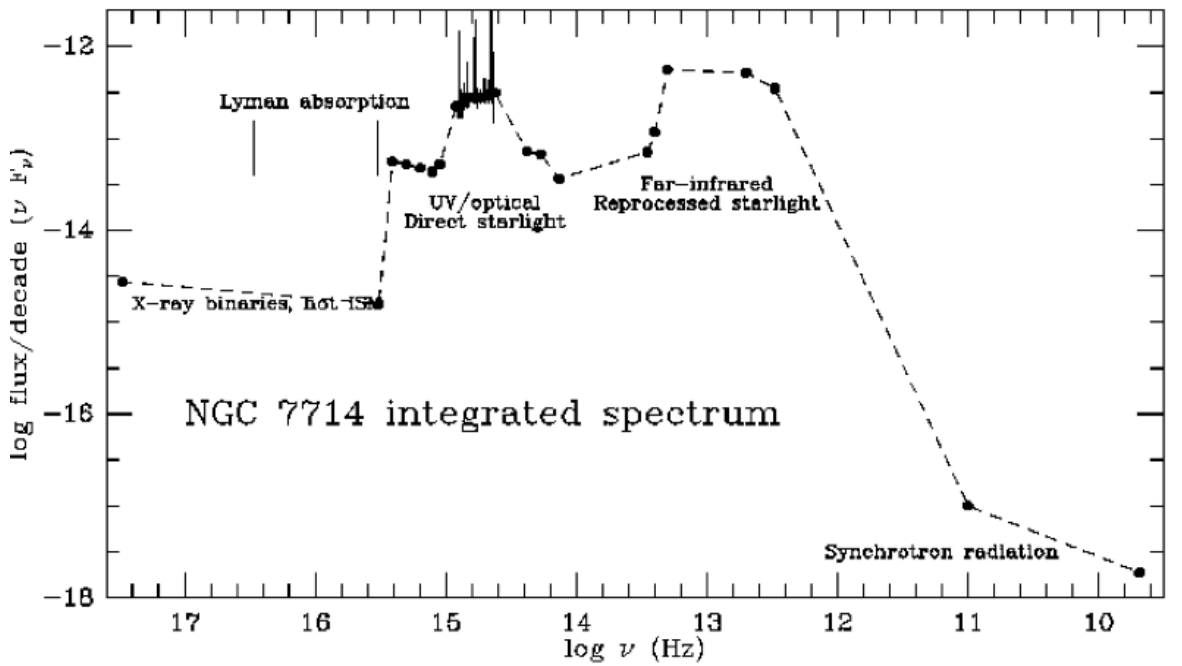


Figure 8: Stellar components emit mostly in UV and visible. Far-IR through dust emission. X-ray and radio emissions are produced by active nuclei.

in supernova remnants. Most indicators probe the SFR for massive stars. Hence they measure the instantaneous/recent SFR of a galaxy or system, and not the time-averaged SFR. To convert the measured luminosity at any wavelength to an SFR, we need to make an assumption for the stellar Initial Mass Function (IMF). The IMF is the distribution of stellar masses that form in one star-formation event in a given volume of space. It is a very important factor that decides the life and fate of a galaxy. Hence, the prescription for the IMF must be chosen very carefully. The Kroupa IMF provides a more realistic mass distribution for a population of stars. In this IMF $\alpha = 2.3$ above half a solar mass, $\alpha = 1.3$ between 0.08-0.5 solar masses and $\alpha = 0.3$ below 0.08 solar masses (Kroupa, 2000), where the total number of stars formed in one event is given by $M^{-\alpha}$. We will be using the Kroupa IMF in our study of Abell 1882.

The indicators have varying sensitivities to the high mass end of the IMF. This makes comparisons between different wavelengths complicated. The lower end of the IMF is extrapolated from the measurements of high mass stars, and hence has a very high degree of uncertainty and is a free parameter.

3.2 Effect Of Dust Obscuration

Luminosities from UV, optical, and near-infrared (NIR) wavelengths trace the stellar light that is not absorbed by dust. Hence we need to correct for dust attenuation for these wavelengths before calculating the SFR. Mid- and far-infrared luminosities, on the other hand, measure the stellar light that has been re-processed by dust and are emitted longward of a few μm and hence do not need to be corrected for dust attenuation. However, in older galaxies, most of the near-IR luminosities may arise from underlying old stars, thus adding to the

uncertainty in the measurement in MIR and FIR caused by recent star formation. Each calibration has its own advantages and limitations which are discussed in next few sections.

3.3 Recombination Emission Lines

Hydrogen recombination lines are emitted from the high mass O and early type B stars (mass $\geq 17 M_{\odot}$). Massive stars emit extremely energetic, highly ionizing UV (energy > 13.6 eV, $\lambda < 912$ Å) which ionizes the HII region. The electron thus released recombines with another proton to give rise to the $H\alpha$ line radiation, amongst others. Owing to their high mass, these stars have a short life span of 10 Myrs or less. The recombination lines trace the star formation over the lifetimes of these stars. Hence they trace the current SFR of the galaxy. The recombination lines mainly constitute of the Balmer lines $H\alpha$, $H\beta$; the Paschen lines $P\alpha$, $P\beta$ $Br\gamma$ and the forbidden emission lines [OII] and [OIII]. Their wavelengths range from $0.3 \mu\text{m}$ to $2.5 \mu\text{m}$. Amongst them, $H\alpha$ provides the most direct and sensitive probe for the young massive stellar population. It is emitted at 6563\AA and the gas in the ISM is largely transparent to $H\alpha$ light. The primary advantages of this method are its high sensitivity and the direct coupling between the nebular emission and the massive SFR. However, some of the $H\alpha$ emission is absorbed by interstellar dust, which processes the UV and re-emits it in IR wavelengths. If extinction corrections are neglected, the median SFR derived from $H\alpha$ emission of nearby galaxies will be underestimated by about a factor of 3. Also a small quantity of the ionizing UV might escape to the IGM and ionize it. It is also affected by contamination from an AGN.

3.4 UV Continuum

The ultraviolet ($\lambda \sim 912 - 3000\text{\AA}$) continuum emission from galaxies is extensively used as an SFR indicator. It is due to O through later-type B stars and early-A stars with mass $\geq 3 M_{\odot}$. These stars are not massive or hot enough to produce H II regions. It directly probes the bulk of the emission from young, massive stars with a life time of $\sim 10^8 - 10^9$ years. However it has a much higher sensitivity to dust reddening and attenuation when compared to $H\alpha$. Dust attenuation within a star-forming region is correlated with the SFR in the system. Hence, the galaxies that are most actively forming stars, and are important in obtaining the cosmic SFR census, also require the largest corrections for the effects of dust attenuation for their UV luminosity. Besides, stars are relatively luminous in the nonionizing UV wavelength range for a relatively long timescale (~ 100 Myr) as compared to other SFR indicators. Hence, cross-calibration of SFR(UV) with indicators at other wavelengths may be complicated. The UV continuum can also have contributions from the UV upturn caused by old massive red galaxies and AGN.

3.5 Thermal Infrared Emission

Interstellar dust absorbs and reprocesses approximately half of the UV and optical starlight in the universe ([62]), and re-emits it in the thermal IR ($\sim 10 - 300 \mu\text{m}$ (FIR)). The absorption cross section of the dust is strongly peaked in the ultraviolet, so FIR emission can be a sensitive tracer of the young stellar population and SFR. This extinction introduces the largest source of systematic error into measurements of the SFR in galaxies ([58]). Thermal MIR and FIR bands and continuum arise from massive stars which have a life span between 10^6

- 10^8 years.

The MIR Bands are emitted between $\lambda \sim 3.5 - 18 \mu\text{m}$ when the UV or optical wavelengths from the massive stars interact with polycyclic aromatic hydrocarbons (PAHs), which are 2-D molecules with dimensions $0.4\text{nm} \leq a \leq 1.2 \text{ nm}$. Interaction of the electromagnetic radiation with PAHs occur much closer to the star as compared to the larger grains. When the UV or optical wavelengths from the massive stars interact with Very Small Grains (VSGs), they undergo grey-body emission and emit the MIR continuum between $\lambda \sim 5 - 40 \mu\text{m}$. A body is said to undergo greybody emission if it does not absorb the entire incident radiation, emits lesser energy than a black body and has an emissivity of less than one. VSGs are 3D carbonaceous grains with dimensions $1.2\text{nm} \leq a \leq 15 \text{ nm}$, also caused due to single photon absorption. FIR radiation is emitted between $\lambda \sim 40 - 1100 \mu\text{m}$. When the UV or optical wavelengths from the massive stars interact with Big Grains (BGs), they undergo black body emission and emit in the FIR bands. BGs are 3-D silicate coated/mixed with carbonaceous material of sizes $15 \text{ nm} \leq a \leq 110 \text{ nm}$. FIR emission is insensitive to dust attenuation and hence can be a sensitive tracer of the young stellar population and SFR. The $8\mu\text{m}$ radiation emitted from PAHs appear in shell-like features around star-forming regions, whereas $24\mu\text{m}$ emission traces the star-forming regions. Observations with the Spitzer Space Telescope show that there might not be a one-to-one correlation of PAH emission at $8\mu\text{m}$ to hot dust emission at $24\mu\text{m}$ within individual galaxies ([109]). PAH $8\mu\text{m}$ emission is suppressed within strong star-forming regions ([18], [99]) compared to $24\mu\text{m}$ emission and disproportionately high in diffuse regions.

A drawbacks of this wavelength for calculation of the SFR is Infrared cirrus ($\lambda \geq 100 \mu\text{m}$) which is extended dust heated by the interstellar radiation field. Blue

galaxies are dominated by young stars. But in red galaxies, where the composite stellar continuum drops off steeply in the blue, dust heating from the visible spectra of older stars may be very important. It is also affected by contamination from AGN, like other wavelengths.

3.6 Combining The Tracers

For calculation of the SFR from infrared emission, we assume that all the energy from the UV is re-emitted in the infrared. This is a good approximation for large starburst galaxies with significant amounts of dust. However, for galaxies with lower masses not all the UV/optical emissions from the stars are absorbed by the dust. The sensitivity of the SFR indicator to variations in the dust content of the system can be removed by combining two tracers: one that probes the dust-obscured star formation (IR) and one that probes the unobscured one (UV/optical/radio). For optical/radio and IR, the following prescription has been proposed in Kennicutt et. al. ([59]).

$$SFR(M_{\odot}/year) = C(L(line, observed) + aL(dust)) \quad (3)$$

where C depends on an assumed IMF for the stellar population, and the luminosity function. The IMF assumed for the following calculations is the Kroupa IMF. $aL(dust)$ is simply a measure of dust obscured luminosity. The values of a for different wavelengths are summarized in Figure 9. We have followed the recipe for mixed tracers for our galaxies, in order to obtain the best estimate for the SFR.

Summary of Coefficients						
Relation	Adopted			Dispersion		
	SINGS	MK06	SINGS+MK06	SINGS	MK06	SINGS+MK06
$L(\text{H}\alpha)_{\text{obs}} + a^*L(24 \mu\text{m})$	0.015 \pm 0.004	0.021 \pm 0.005	0.020 \pm 0.005	0.140	0.108	0.119
$L(\text{H}\alpha)_{\text{obs}} + a^*L(\text{TIR})$	0.0020 \pm 0.0005	0.0025 \pm 0.0006	0.0024 \pm 0.0006	0.131	0.067	0.089
$L(\text{H}\alpha)_{\text{obs}} + a^*L(8 \mu\text{m})$	0.010 \pm 0.003	...	0.011* \pm 0.003	0.112	...	0.109
$L(\text{H}\alpha)_{\text{obs}} + a^*L_{1.4\text{GHz}}$	0.41 \pm 0.13	0.39 \pm 0.10	0.39 \pm 0.10	0.146	0.087	0.099

Figure 9: Values of 'a' for different combinations of wavelengths for calculation of star formation rate used in Equation 3 (Kennicutt et. al., 2009).

3.7 Classifying Different Galaxies Based On Their Star Formation Histories

The star formation rate (SFR) reflects the most recent changes in a galaxy's environment, while the star formation history (SFH) tracks the past histories of the galaxies to get their complete evolutionary picture. The following sub-sections summarize the different wavelengths or combinations of them, that can be used to study the SFH and also to identify the types of galaxies that are of interest to us, in order to trace the evolutionary path of these systems.

3.7.1 Post-Starburst (k+a) Galaxies

Post-Starburst (k+a) galaxies seem to occupy the transitional state between the star-forming and nonstar-forming populations. Their spectrum is a combination of an early-type galaxy spectrum and an A type stellar spectrum. These are galaxies where star formation (SF) has recently and rapidly shut down. A galaxy is more likely to become a k+a galaxy if it experiences a period of enhanced star formation prior to the quenching, as opposed to the rapid truncation of a low level of continuous star formation. 3-D hydrodynamic simulations suggest that they are primarily formed due to merger of spiral galaxies, and not due to AGN feedback ([97]). A typical duration of the k+a phase is $\leq 0.1 - 0.3$ Gyr for the

merger of equal- mass gas-rich progenitors.

Measurements of $H\delta$ strength are comparatively insensitive to dust absorption, because for the time averaged SFR over the 10^9 years timescale, the A - F stars that contribute most to the $H\delta$ signal are expected to have diffused out of the dusty regions in which they were born. Hence, k+a galaxies show moderate absorption in $H\delta$ and little or no emission in $H\alpha$ and [OII]. The k+a galaxies that we have identified are dominated by galaxies obtained using MMT/hectospec due to poor S/N of the GAMA spectrum in the low wavelength regime.

3.7.2 Calculating Star Formation History using [OII] λ 3727 And $H\delta$

A quantitative comparison of the strength of [OII] λ 3727 and $H\delta$ indicators measures whether the star formation rate has been steady over the previous $\tau \sim 10^9$ years or whether there has been a starburst with a rapid decline in the SFR over that timescale. The spectral classifications of galaxies have been adopted from Dressler ([28]). Negative values indicate an emission line, whereas positive values indicate an absorption line. For the k+a galaxies we have also applied an additional cut of $H\alpha > -3\text{\AA}$. The mass bins have been obtained using the KCORRECT package and has been described in more details in Section 4.2.2.

TABLE 3: Spectral types of galaxies versus different histories of star formation:

Class	EW([O II])	EW($H\delta$)	Stellar Population
k	absent	$< 3\text{\AA}$	passive
k+a	absent	3 - 8\AA	weak post-starburst
e(c)	-40 \AA - -5 \AA)	$< 4\text{\AA}$	continuous star formation
e(a)	(-40 \AA -5 \AA)	$\geq 4\text{\AA}$	ongoing starburst

TABLE 4: Spectral classifications of galaxies for this work:

Spectral type	Post-starburst (k+a)	Starburst	Passive
# high mass galaxies	0	0	63
# intermediate mass galaxies	19	30	169
# low mass or dwarf galaxies	9	12	30
Total	28	42	232

4 DETERMINATION OF PHOTOMETRIC PARAMETERS

Galaxy color, which is defined as the magnitude difference between the intensity of radiation at two different wavelengths emitted by a galaxy, reflects the ongoing star formation as well as the star formation history (SFH) of a galaxy (eg. [53], [93], [90]). It traces the chemical evolution in terms of its dust components and metallicity. It is one of the most basic and direct galaxy diagnostics. Galaxies in the local Universe follow a well defined color–magnitude relation (CMR) (eg. [95], [2]; [11]; [12]; [106]; [46]); [66]; [6]; [8]; [72]; [36]). The color–magnitude relation shows a bimodal distribution that separates the galaxies into a tight red sequence (with $\sigma(g - r) \approx 0.04$ mag from [107]; $\sigma(g - r) \approx 0.05$ mag from [8], a blue cloud, and an intermediate green valley region in optical colors. The red sequence primarily consists of the early type galaxies (ellipticals and lenticulars) with very low or no recent star formation, while the blue cloud contains the later type galaxies (spirals) which are actively forming stars or have had star formation episodes at least in the past 10^8 years. Galaxies within the blue cloud are not as tightly sequenced in the color-magnitude space and show a larger scatter than the red sequence. The small scatter within the red sequence is possibly due to lack of recent star-forming activity in the early type galaxies ([12]). However they show a systematic variation in the relation. Galaxy bimodality may have its origin in the metallicity sequence of the galaxies, where the more luminous early type galaxies are more metal rich ([64]; [13]; [60]). However, [52], [55] show that age may play an even more important role in the formation of galaxy bimodality.

4.1 Origin of Galaxy Bimodality

Models proposed to understand the bimodality of galaxies can be broadly classified into two categories: (i) hierarchical merger of galaxies, where the galaxy mergers can cause the combined dark matter halo to cross a critical halo mass ($> 10^{12} M_{\odot}$), generating a shock in the accreting gas, heating and thus preventing it from cooling and forming stars, rendering them red and dead by $z \sim 0$. If the galaxies reside in smaller halos, the gas will not be shock heated. This allows for the star formation and subsequent regulation of the same by several feedback mechanisms. This model seems to favor the hierarchical structure formation theory in the Λ CDM model; (ii) a monolithic progression of blue galaxies into the more redder and luminous ones with eventual quenching of star formation as their gas reservoirs deplete with time. This is not likely to cause the large number of disk red galaxies observed in the present day Universe. The brightest red galaxies are brighter than the brightest blue galaxies. Combined with the fact that these red galaxies form a tight narrow sequence, it strongly implies dry mergers as driving force in the formation of observed bimodality of the galaxies. Dry mergers are defined as the mergers between already gas-poor galaxies, usually in the red sequence, that already have their stellar population in place prior to the merging. Hence the merger does not produce any significant star formation. However, it causes the stellar mass growth of the galaxies.

The Universe is not old enough for passive galaxies to have faded in u -band as in UV bands. In optical colors $g - r$ reflects the average star forming behavior of a galaxy over most of the cosmic time ~ 10 Gyrs (Figure 10); whereas $u - r$ is more sensitive to recent star formation over ~ 2 -3 Gyrs (Figure 11). The u -band lies short-ward of 4000\AA and are emitted from younger, hotter, short-lived stars.

The UV is far more sensitive to the presence of younger stars than the u-band, indicating the presence of 0.3 - 1 Gyr old populations. High UV flux indicates the presence of young stars with a life time of ~ 100 Myr. Hence, $(NUV - r)$ has greater sensitivity of the colors to very low specific star formation rates as compared to optical colors (Figure 12) and traces recent star formation history better than $u - r$ color. $(NUV - r)$ produces a scatter of more than ~ 1 mag in the CMD as compared to the optical CMD ([8]). The scatter cannot be completely explained by the photometric uncertainty, which is ≈ 0.1 mag in NUV, and the k-correction (discussed in 4.2.2) for each band. The blue sequence shows a tighter peak than in optical colors (eg. [2]; [110], [104]). Yi et al. ([104]) shows that 15% of bright early-type galaxies $\sim M(r) < -22$ show signs of recent star formation in the UV continuum. This effectively rules out monolithic galaxy formation models. For small galaxies, star formation is stochastic. Hence, galaxy color averaged over longer periods (i.e. $g - r$) gives smaller error in color.

TABLE 5: Implied timescales for different wavelengths and colors:

Color/Wavelength	Implied timescales (in years)
H α	$\approx 10^6$
FUV	$\approx 10^8$
NUV	$\approx 10^9$
$u - r$	$\approx 2 - 3 \times 10^9$
$g - r$	$\approx 10^{10}$ (i.e. entire star forming life of a galaxy)

4.2 Color-Magnitude Diagram

The r-band absolute magnitude and the color defined by $u - r$, $g - r$ and $NUV - r$ have been calculated using the following formulae prescribed in Baldry et al., 2004 ([2]).

$$M_r = PetroMag_r - kcor_\lambda - 5\log(D_L(pc)/10) \quad (4)$$

$$C_{\lambda-r} = (ModelMag_\lambda - kcor_\lambda) - (ModelMag_r - kcor_\lambda) \quad (5)$$

where, $\lambda = ugriz$ & NUV , M is absolute magnitude, C is rest frame color, $kcor$ is K-correction, $ModelMag$ is Model magnitude and $PetroMag$ is Milkyway extinction corrected Petrosian magnitude ([81]).

The number of red, blue and green galaxies in both the optical colors ($u - r$ and $g - r$) are comparable. $g - r$ color receives most of its flux from the older population and hence is more representative of the same. NUV on the other hand receives a much higher flux from the younger population of stars as compared to the older population and reflects recent stellar activity.

The NUV flux limit in our data from GALEX cuts so strongly that we lose most of the galaxies below the mass range of $10^{10}M_\odot$ (Figure 12). This severely undercounts the number of red galaxies in $NUV - r$ color (Table 5). We see almost double the number of green valley galaxies in $NUV - r$ as compared to the $g - r$ and $u - r$. Given that the flux limit will result in reduction of observed green valley galaxies in the $NUV - r$, this over-abundance of $NUV - r$ green valley galaxies indicate that the UV colors are much better diagnostics of more recent star formation episodes between 0.3 - 1 Gyrs. And hence, the galaxies that appear in the red sequence in the optical colors, can occur in the green valley region in

$NUV - r$ color if they had recent star formation, even if they are optically red.

4.2.1 Petrosian And Model magnitudes

The Petrosian magnitude measures the summed flux in an aperture that depends on the surface-brightness profile of the object. Galaxies do not have the same radial surface brightness profile, and lack sharp edges. This makes the flux measurement in galaxies far more complicated than that of stars. In order to avoid such biases and measure the galaxy flux independent of its position and distance a constant fraction of the total light is measured. This is a modified version of the flux quantity defined by Petrosian (1976). Galaxy fluxes are measured within a circular aperture whose radius is defined by the shape of the azimuthally averaged light profile. The Petrosian ratio R_P at a radius r from the center of an object is the ratio of the local surface brightness in an annulus at r to the mean surface brightness within r ([10]):

$$R_P \equiv \frac{\int_{0.8r}^{1.25r} dr' 2\pi r' I(r') / [\pi(1.25^2 - 0.8^2)r^2]}{\int_0^r dr' 2\pi r' I(r') / (\pi r^2)} \quad (6)$$

where $I(r)$ is the azimuthally averaged surface brightness profile. The Petrosian radius is then defined as the radius at which $R_P \equiv 0.2$. The Petrosian flux in any band is then defined as the flux within 0.2 Petrosian radii:

$$F_P \equiv \int_0^{0.2r_P} 2\pi r' dr' I(r'). \quad (7)$$

In the SDSS five-band photometry (*ugriz*), the aperture in all bands is set by the profile of the galaxy in the r-band alone so that the color measured by comparing the Petrosian flux in different bands is measured through a consistent aperture. The aperture which is twice the Petrosian radius is large enough to contain nearly all of the flux for typical galaxy profiles, but small enough that the sky noise in the flux is small. Hence, even substantial errors in Petrosian radius cause only small errors in the Petrosian flux ($< 5\%$ at $r \sim 17.7$). The Petrosian magnitudes are expected to recover almost all of the flux of an exponential galaxy profile and about 80% of the flux for a de Vaucouleurs $r^{1/4}$ profile ([24]). This implies that the fraction of flux measured for exponential profiles decreases while the fraction of flux measured for de Vaucouleurs profiles increases as a function of distance. However, for galaxies in the spectroscopic sample ($r < 17.7$), these effects are small. Hence the Petrosian radius measured in the SDSS catalog is extraordinarily constant in physical size as a function of redshift. Model magnitude is a fit to the flux using the better fit of a de Vaucouleurs and an exponential profile.

4.2.2 K-Correction

Spectral energy distributions of distant galaxies are redshifted in a manner such that with increasing galaxy distance, the observed bandpass is increasingly blue-shifted relative to the rest-frame spectral energy distribution of the object observed. This can be accounted for by using K-corrections to the observed magnitudes. Hence, the K-correction can be defined as a correction to an astronomical object's magnitude/flux that allows a measurement of a quantity of light from an object at a redshift to be converted to an equivalent measurement in the rest frame of the object. The need for a K-correction arises because measurements

are through a single filter or a single bandpass and hence one sees only a fraction of the total spectrum, redshifted into the frame of the observer. K represents the reduction factor in magnitude due to this effect. The calculation requires the knowledge of the type of filter used to make the observation and the shape of the object's spectrum. The K-correction for this work has been obtained using the IDL package `kcorrect.v4.2` ([11]). In this analysis a function $K(z)$ is added to the standard cosmological bolometric distance modulus $DM(z)$ to obtain the relationship between the apparent magnitude m_R of band R and the absolute magnitude M of band λ :

$$m_r = M_Q + DM(z) + kcor_{\lambda R}(z) \quad (8)$$

`kcorrect.v4.2` fits very restricted spectral energy distribution models to galaxy photometry in the rest frame UV, optical and near-infrared. The templates it uses are based on Bruzual-Charlot stellar evolution synthesis codes and hence for each fitted galaxy one can obtain an estimate of the stellar mass-to-light ratio. The code requires an input of galaxy redshifts, magnitudes in AB and Galactic-reddening corrected SDSS systems and their errors. The outputs are k-corrections in *ugriz* satisfying the above equation, current stellar mass-to-light ratios from the model in each band, average metallicity in current stars, total integrated star formation history, and star-formation within last 0.3-1 Gyrs relative to average star-formation rate. Since all our magnitudes are obtained from SDSS, we have used the `SDSS_KCORRECT` code.

4.2.3 Galaxy Stellar Mass

The total current stellar mass of the galaxies in solar masses has been obtained with the KCORRECT package which uses the Bell and de Jong stellar mass model ([7]). We have divided the galaxy mass into three bins: the high mass galaxies ($> 10^{10.5} M_{\odot}$), the intermediate mass bin ($10^{9.5} M_{\odot} < \text{Mass} < 10^{10.5} M_{\odot}$) and the low mass bin or the dwarf galaxies ($< 10^{9.5} M_{\odot}$). There are external motivations for the mass division. Several studies have drawn attention to the galaxies in the mass range of $< 10^{9.5}$ which show especially strong environmental transformations. The dwarf galaxies can be defined by the recipe provided by [9] ($z\text{-mag} > 15$; $M_z > M^* + 2.3$ for Coma Supercluster, where $M_z^* = -22.32$). Using the above recipe for Abell 1882 at $z\text{-mag}=0.138$ we get $z > 19.1$ for dwarf galaxies. The low mass galaxies correspond reasonably well with this $z\text{-mag}$ limit defined for dwarf galaxies in Coma cluster.

The MMT sampling goes fainter than the SDSS and GAMA survey limits, but covers only 1° in the sky. We have gone further out up to almost $\sim 2^\circ$ in the sky using SDSS and GAMA surveys. Hence dwarf sampling is sparse in the outskirts.

4.2.4 Distance Indicators

Luminosity distance D_L is an important distance indicator that is based on the flux received from an object, and it is defined as follows,

$$D_L = \sqrt{\frac{L}{4\pi F}} \quad (9)$$

where L and F are bolometric luminosity and bolometric flux respectively. The luminosity distance for Abell 1882 is 654.2 Mpc or 2.134 Gly. Luminosity distance

is required for conversion of Petrosian magnitude into absolute magnitude.

We have estimated the size of the SuperGroup Abell 1882 using the angular diameter distance (D_A) formula. The angular diameter distance D_A is dened as the ratio of an objects physical transverse size (S) to its angular size (θ) in radians and is defined as follows

$$D_A \approx S/\theta(\text{radian}) \quad (10)$$

Luminosity distance and angular distance are related by the following formula,

$$D_A = \frac{D_L}{(1+z)^2} \quad (11)$$

At the assumed center of Abell 1882 (RA = 213.71° and Dec = -0.41°, $z \approx 0.138$), the angular size distance D_A is 503.4 Mpc or 1.6 Gly. This gives a scale of 2.440 kpc/arcsec. Hence, the transverse size for the entire SuperGroup 1882 along with its feeding filaments for an angular size of 1.05° at $z = 0.138$ is 9.2 Mpc.

4.2.5 AB Correction

The SDSS photometry is intended to be on the AB system ([78]), by which a magnitude 0 object should have the same counts as a source of $F_\nu = 3631$ Jy. However, the photometric zeropoints are slightly off the AB standard. We use the following formulae to obtain the corrected magnitudes as recommended in the SDSS archive:

$$\lambda_{corrected} = \lambda_{AB} - \lambda_{extinction} - k_{cor\lambda} \quad (12)$$

where, $u_{AB} = u_{SDSS} - 0.04$; $z_{AB} = z_{SDSS} + 0.02$; $gri_{AB} \approx gri_{SDSS}$.

4.2.6 Galactic Extinction Correction

The magnitudes are extinction-corrected using the values from SDSS archive which have been calculated using the the dust maps of [94]. This corrects for the foreground extinction of the Milky Way. The internal dust correction is accounted for each galaxy by considering the FIR (24 μm) emission from the hot dust.

4.3 Best Fits For Bimodal Distribution In the Galaxies

The best fits for the colors of red sequence and blue cloud galaxies for the $u-r$, $g-r$ and $NUV-r$ colors are obtained from Baldry et al., 2003 ([?]Baldry04),

$$(u-r) : T(x) = p_0 + p_1x + q_{x0}\tanh\left(\frac{x - q_1}{q_2}\right) \quad (13)$$

where, the T -function is a \tanh plus *straightline function*. $p_{0,1}$ are the *straightline* parameters and $q_{0,1,2}$ are \tanh parameters. The values of above parameters for red sequence and blue cloud are obtained from [2].

$$Red : (g-r) > -0.025 \times (M_{0.1r} - 5\log(h)) + 0.42 \quad (14)$$

$$Blue : (g-r) < -0.025 \times (M_{0.1r} - 5\log(h)) + 0.35 \quad (15)$$

$$Red : (NUV-r) > -0.143 \times (M_{0.1r} - 5\log(h)) + 2.57 \quad (16)$$

$$Blue : (NUV-r) < -0.429 \times (M_{0.1r} - 5\log(h)) - 6.29 \quad (17)$$

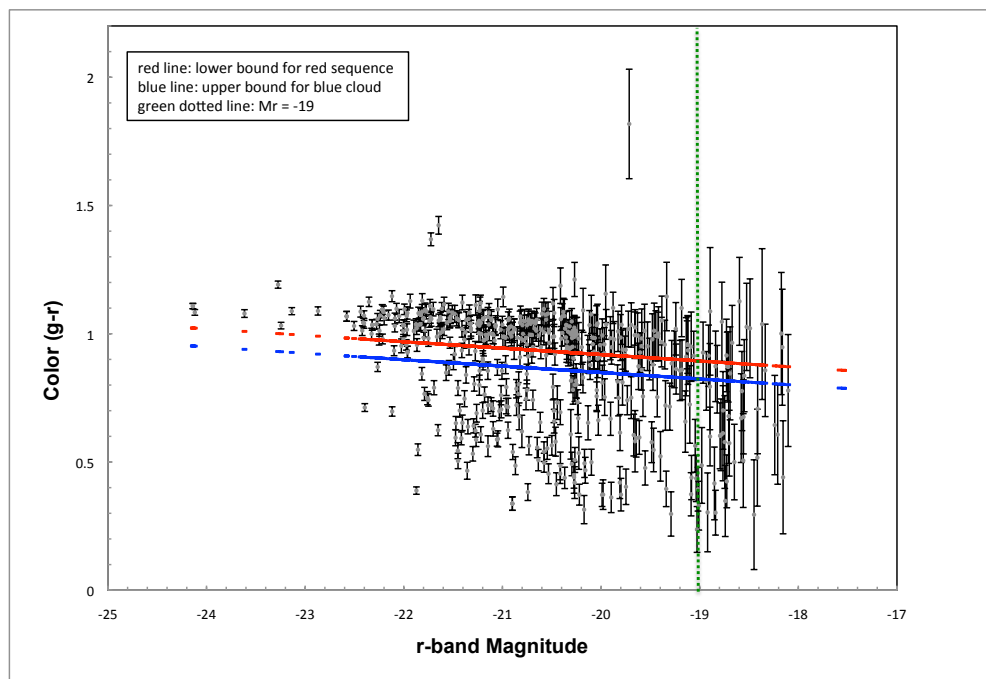


Figure 10: Color (g-r) - Magnitude Diagram for the member galaxies of Abell 1882. The red line shows the lower cut of for the red sequence galaxies. The blue line shows the upper cut for blue cloud galaxies (Best fit recipes obtained from Baldry et al., 2004 [2]).

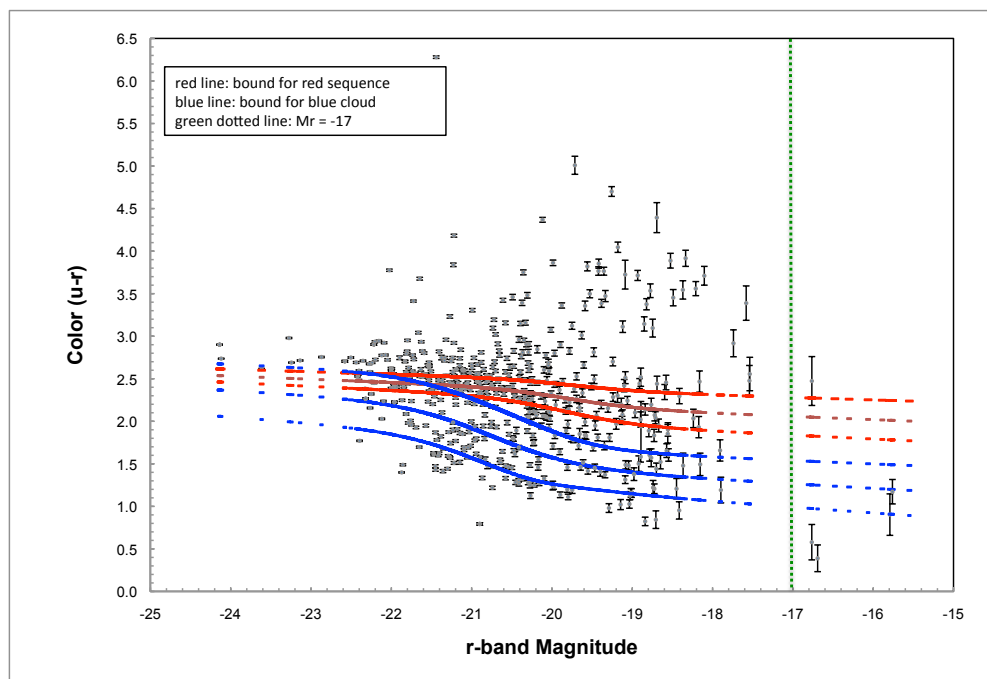


Figure 11: Color ($u-r$) - Magnitude Diagram for the member galaxies of Abell 1882. The red lines show the best fit for red sequence and 1σ boundaries. The blue lines show the best fit for the blue cloud galaxies and its 1σ boundaries (Best fit recipes obtained from Baldry et al., 2004 [2]).

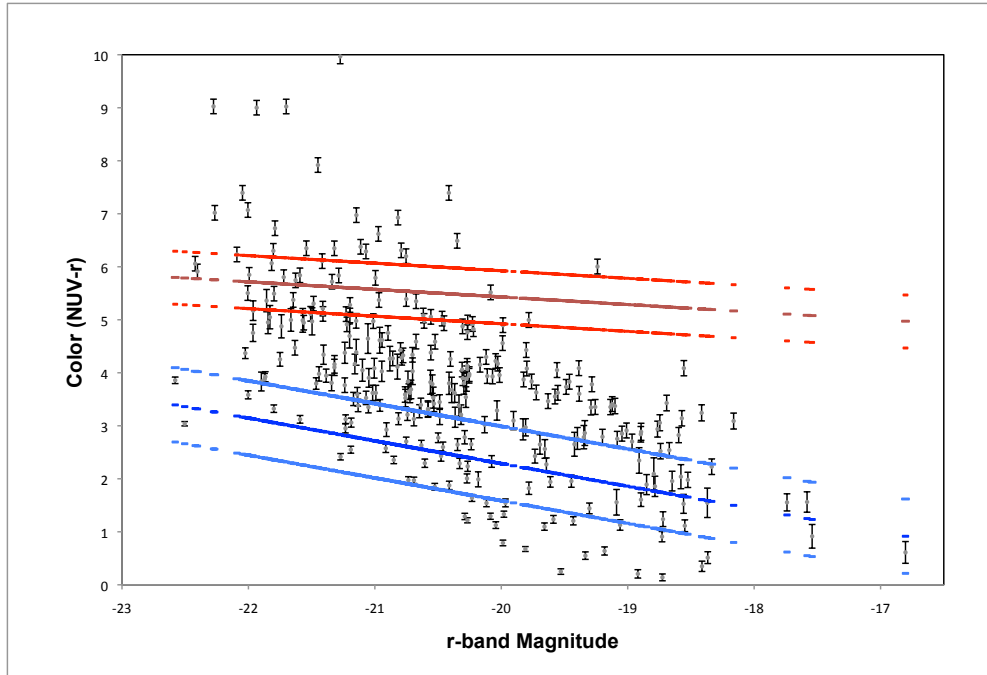


Figure 12: Color (NUV-r) - Magnitude Diagram for the member galaxies of Abell 1882. The red lines show the best fit for red sequence and 1σ boundaries. The blue lines show the best fit for blue cloud galaxies and its 1σ boundaries. (Best fit recipes obtained from [?]). The NUV flux limit in GALEX cuts strongly enough to severely undercount the number of red galaxies in NUV-r color. However, we see almost double the number of green valley galaxies in NUV-r as compared to the optical color-magnitude diagrams indicating that the UV colors are much better diagnostics of more recent star formation episodes between 0.3 - 1 Gyrs..

TABLE 6: Fractional Number Of Galaxies In Optical And UV Colors

Color	No.(Red Galaxies)	No.(Blue Galaxies)	No.(Green Galaxies)
$u - r$	290	193	43
$g - r$	295	187	44
$NUV - r$	52	148	88

4.4 Color Derived Mass Plots

Galaxy stellar mass affects its star formation histories, colors, morphologies etc. (e.g. [14]; [50]). Galaxies with higher stellar masses experience earlier, shorter and more intense initial star formation episodes. At a later cosmic time, the less massive galaxies exhibit increased star formation activity i.e. archaeological downsizing (e.g. [17]). Stellar masses for this work have been obtained from the KCORRECT package. It uses stellar population synthesis models and calculates the current mass of stars. The color derived mass relation of galaxies is one step closer to a more physical picture of galaxy evolution as compared to that of the color-magnitude plot. It removes the luminosity favoritism in the older population which have higher mass and hence more luminosities. Flux to mass transformation is more affected by details of star formation as we consider shorter and shorter time scales. Hence the $g - r$ color shows a tighter mass-color relation (Figure 13) as compared to $u - r$ color (Figure 14). And in the $NUV - r$ color-mass diagram, the red galaxies are even less densely packed as the optical color-mass diagrams (Figure 15). This follows from the fact that $NUV - r$ reflects the recent star formation between 0.3-1 Gyr that the longer time scale diagnostics fail to detect.

TABLE 7: Mass Bins Of The Galaxies Defined for this work:

Mass bin	Mass Range (in Solar Masses)	#
# high mass galaxies	$> 10^{10.5}$	84
# intermediate mass galaxies	$10^{9.5} < M < 10^{10.5}$	326
# low mass or dwarf galaxies	$< 10^{9.5}$	116
Total		526

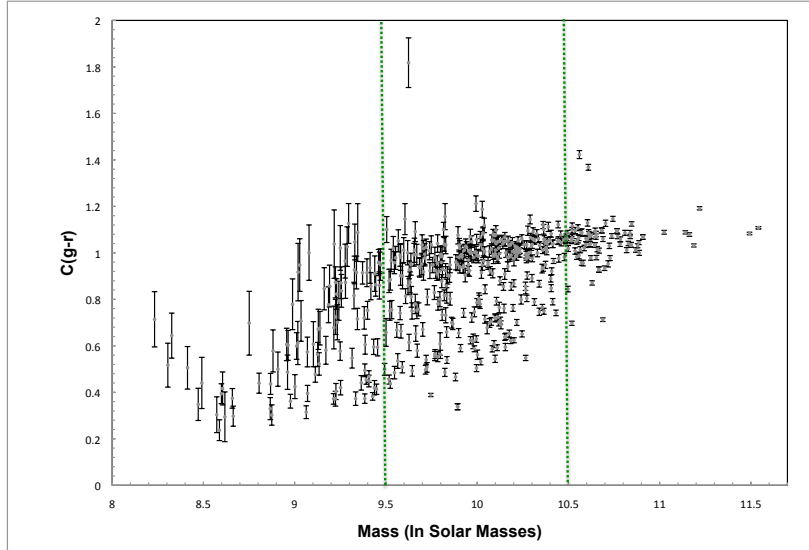


Figure 13: Color (g-r) - Mass of Abell 1882 galaxies. Green vertical lines show the different mass regimes, i.e. dwarf galaxies ($< 10^{9.5} M_{\odot}$), intermediate mass galaxies ($10^{9.5} M_{\odot} < M < 10^{10.5} M_{\odot}$) and high mass galaxies ($> 10^{10.5} M_{\odot}$).

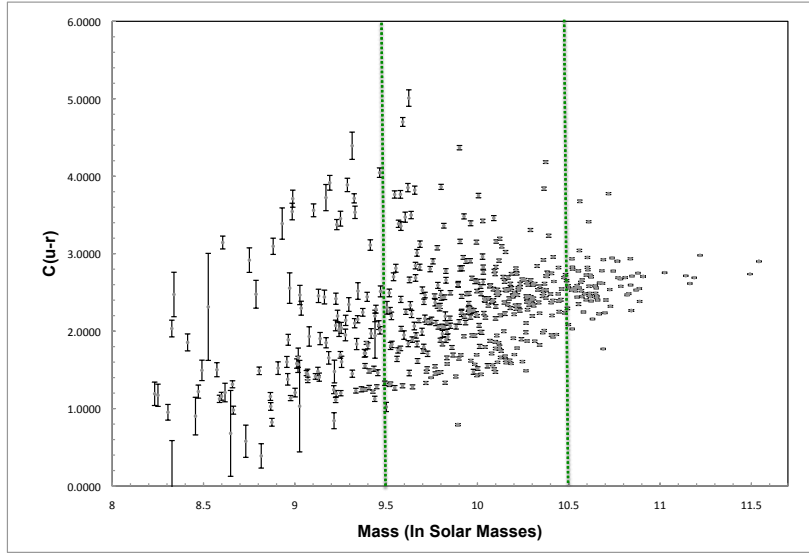


Figure 14: Color (u-r) - Mass Relation of Abell 1882 galaxies. Green vertical lines show the different mass regimes.

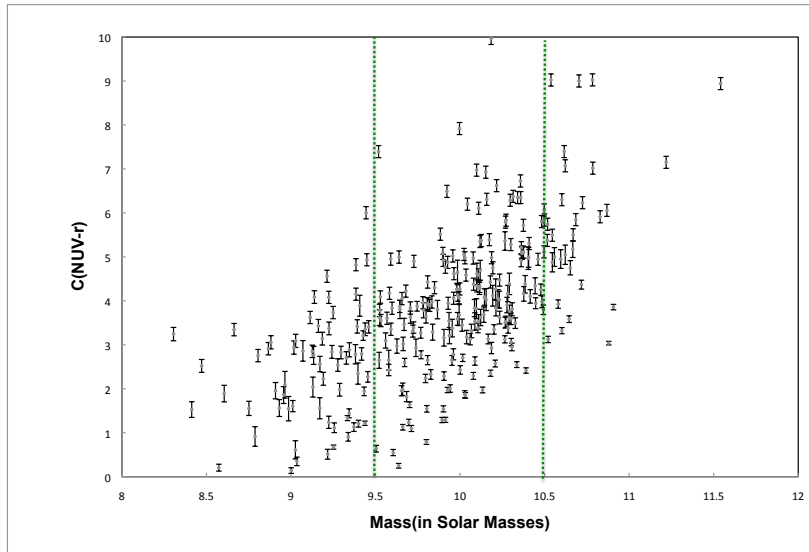


Figure 15: Color (NUV-r) - Mass Relation of Abell 1882 galaxies. Green vertical lines show the different mass regimes. Redder galaxies are less densely packed as compared to the optical color-mass diagrams. This follows from the fact that NUV-r reflects the recent star formation between 0.3-1 Gyr that the longer time scale diagnostics fail to detect.

5 STRUCTURE DETERMINATION

In this chapter we discuss the determination of local galaxy density using the recipe given by Baldry et al., 2006 ([3]). We also determine the filamentary structures of the cosmic web made up of galaxies that feed into the Supergroup Abell 1882, using Friends-of-Friends algorithm. We further discuss the caustic diagram of Abell 1882 which traces the redshift of galaxies as a function of projected cluster-centric radius.

5.1 Local Galaxy Density (Σ) Profile

The morphology-density relation of galaxies has proven to be remarkably robust in both clusters up to redshift ≈ 1 as well as local groups ([26], [27], [85], [86], [103]; [96]) (Figure 16). Elliptical galaxies preferentially reside in the high density regions, whereas the spiral galaxies mostly reside in the low density regions. The S0 galaxies maintain a constant fractional number within the virial radius of a cluster, irrespective of the cluster density.

The star formation-density relation and other galaxy properties related to star formation, eg. color-density, average stellar age-density (eg. [98]), star formation history-density, at least at low redshifts have been shown to exist not only within the cluster virial radius, but also in the cluster outskirts, groups and fields ([44], [65], [38], [53], [4], [82], [3], [67], [68]) Higher density regions harbor red, older populations with significantly suppressed star formation rate as compared to the lower density regions. The color-density relation appears to be sealed at least as early as $z \approx 1.5$ ([22]; [20]; [32]).

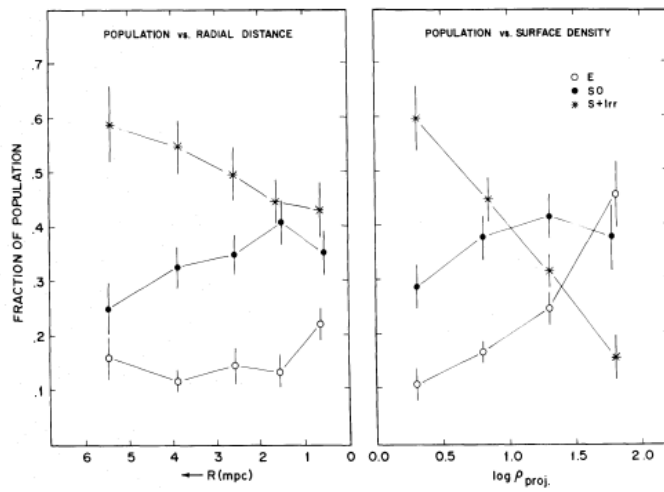


Figure 16: The morphology-projected radial distance (*left*) and morphology-density relation (*right*) reproduced from Dressler, 1980. The fractions of E, S0, and spiral plus irregular galaxies are shown as functions of the projected local density ($\#galaxies/Mpc^2$) and projected radial distance (Mpc). The histograms show the number distribution of galaxies found in various environments, for a sample of over 6000 galaxies in 55 rich clusters. The fraction of spiral galaxies falls steadily for increasing local density and decreasing projected radial distance, complimented by a corresponding rise in the fraction of elliptical and S0 galaxies.

5.1.1 Determination Of Local Galaxy Density (Σ)

The Σ for each galaxy is given by (Baldry, 2006) ([3])

$$\Sigma_N = \frac{N}{\pi d_N^2}, \quad (18)$$

where d_N is the averaged projected co-moving distance of a galaxy from its 4th and 5th nearest neighbors that is a member of a density defining population (DDP). We identify the density defining population (DDP) which are given by the galaxies which satisfy the following relations ([11]),

$$M_r < M_{r,limit} - Q(z - z_0) \quad (19)$$

where $M_{r,limit} = -20$, $z_0 = 0.05$ and $Q = 1.6$. Luminosity density is a measure of the contents of the local Universe and Q is the parameter describing the evolution of the galaxy luminosity density assuming that galaxies of all luminosities evolve identically.

Although Σ sharply increases with decreasing projected radius, there are distinct over-dense structures in the outskirts and the infall regions of Abell 1882 (Figure 17). It indicates that this SuperGroup is still in the process of growing and accreting, and is still highly unvirialized.

5.2 Friends-Of-Friends Algorithm To Determine The Feeding Filaments

In order to identify the feeding filaments in the cluster outskirts, we have used the Friends-Of-Friends (FOF) percolation algorithm developed by Huchra & Geller ([47]). This technique recursively links all the galaxies within a linking length,

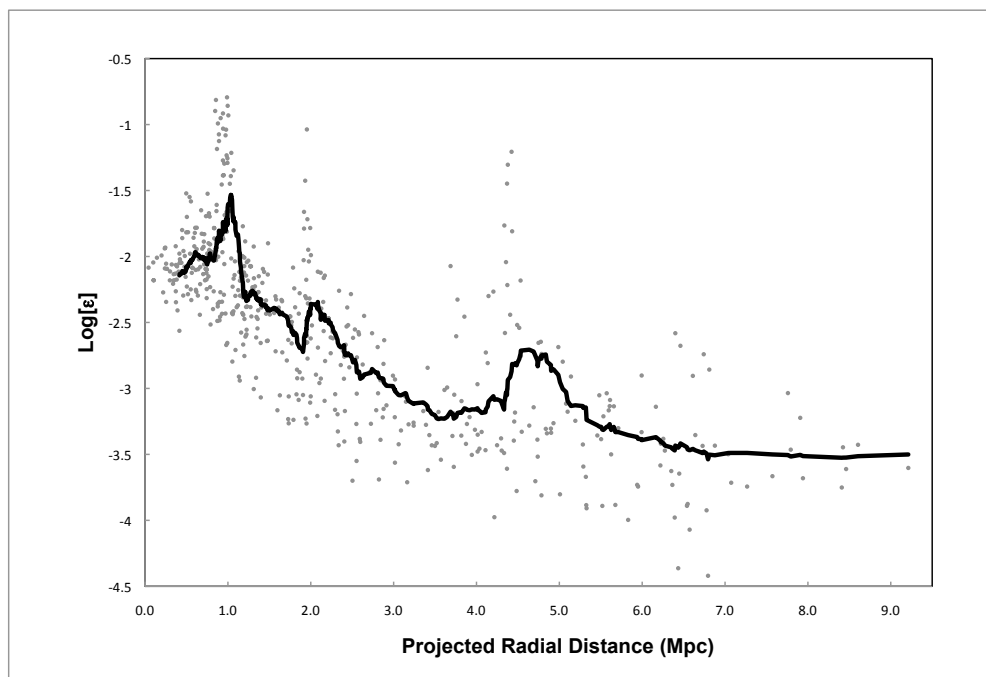


Figure 17: Projected radial distance from the adopted center of Abell 1882 Versus $\text{Log}[\Sigma]$ (local galaxy density) of the galaxies. In this plot, the three groups (A,B and C) lie at ~ 1 Mpc. The Σ correlates well with the projected radial distance. However, the plot shows clumpiness in Σ at ~ 2 Mpc, that coincides with the fourth X-Ray group (D). There is also a region of increased density at the further outskirts at ~ 5 Mpc.

b, nominally such that the dynamical parameters of the structures are stable. There are several approaches to the FOF algorithm, although the basic principal remains the same. Different algorithms employ different criteria for linking length, and each one contains its own checks against galaxy density variation which is inherent in flux-limited surveys. In our case, we use photometric data drawn from SDSS archive, which is a magnitude-limited survey.

The projected transverse distance separation ($D_{\perp,ij}$) and line-of sight separation ($D_{\parallel,ij}$) of the galaxies is given by:

$$D_{\perp,ij} = (c/H_0)(z_i + z_j)\sin(\theta_{ij}/2) \quad (20)$$

$$D_{\parallel,ij} = (c/H_0)|z_i - z_j| \quad (21)$$

Since we have already imposed a redshift constraint on our galaxy catalog based on the redshift histogram to find the cluster membership, $D_{\parallel,ij}$ does not play any further role and has been set to zero for the this algorithm. We define a filament as a structure containing 3 or more galaxies connected by a linking length. For a given linking length, the FOF will return a unique set of filaments. The algorithm also satisfies a nesting condition. Hence, a filament identified with a linking length is also identified as belonging to the same set when we use a larger linking length. The galaxies are connected to a single structure if their projected transverse distance separation ($D_{\perp,ij}$) satisfies the following relation:

$$D_{\perp,ij} \leq b_{\perp}\bar{n}_g^{-1/3} \quad (22)$$

where, \bar{n}_g is the mean number density of galaxies. Optimizing the linking length

lies at the heart of the FOF method. If the linking length is too short, it will detect a single structure as multiple smaller structures. On the other hand, if it is too long, it will merge distinct substructures into one single big structure. A linking length is not a constant that can be applied to all structures uniformly. It needs to be carefully selected keeping in mind the structure under consideration. To find the correct linking length, we created several mock galaxy catalogs, and compared the number of galaxies in the longest detected filament (N) in each of the galaxy catalog with that of the original observed galaxy catalogs. We then constructed a cumulative of the number of galaxies in the largest filament of the mock galaxies, where the threshold N gives the probability of the structures detected in real galaxy catalog for a given linking length. The confidence level of the FOF detected filaments is measured at 99%. As an approximation, $b = 0.2$ is a good place to start since this value is used to identify halos in the N-body simulations.

The FOF algorithm requires the linkage length in distance (Mpc), linkage length in velocity (km/s), limiting magnitude for the survey, and parameters to evaluate Schechter luminosity function as its inputs. Abell 1882 is highly unvirialized and hence the total velocity dispersion of the system is not reflective of the central potential. However, our catalog is well constrained in redshift. Hence we provided a large velocity dispersion or linkage velocity in order to include all the catalog galaxies (≈ 650 km/s). The in-falling filaments in the system detected by the FOF method matches very well with the Σ profile (Figure 19).

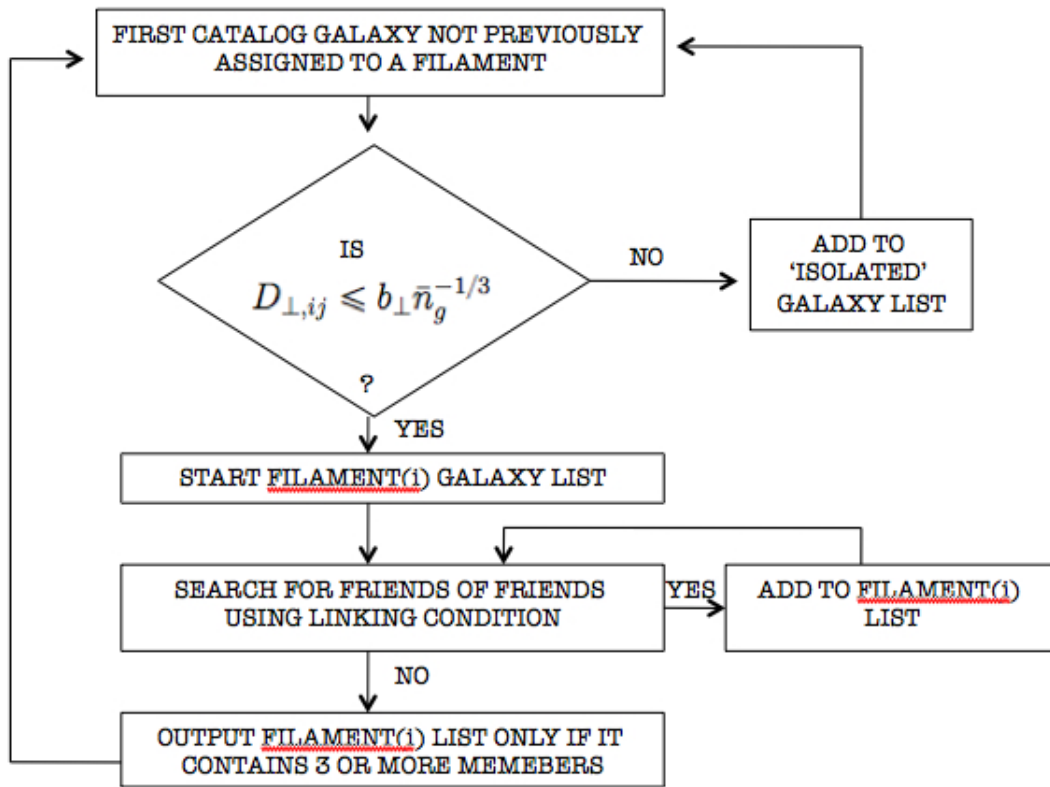


Figure 18: Friends-Of-Friends Algorithm (Recipe from Huchra & Geller, 1982).

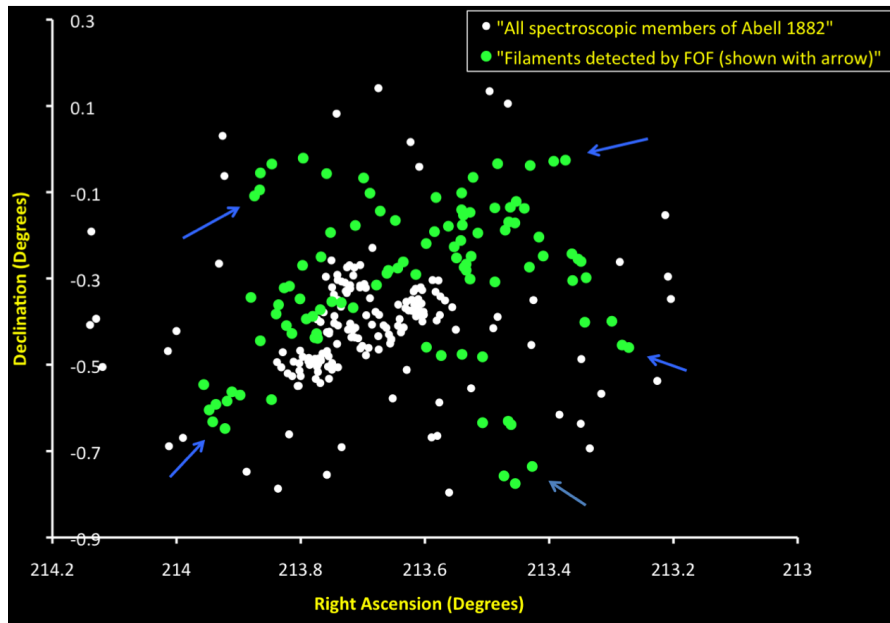


Figure 19: Friends-Of-Friends Detected Filaments in green. The white dots represent all the galaxies. Only the inner 1° region has been shown for clarity.

5.3 Caustic Diagram

A caustic diagram traces the redshift of galaxies as a function of projected cluster-centric radius. For a rich cluster, the infall pattern of the galaxies has a characteristic trumpet shape, whose amplitude increases with decreasing projected radius ([51]). Galaxies make their way from the filaments into the cluster/proto-cluster potential accelerated by the gravity. The effect of the cluster gravity extends well beyond the virial radius, which separates the filaments and the infall regions from the Hubble expansion of the Universe out to 10-20 Mpc. This causes an accelerated galaxy transformation even before a galaxy falls into the virialized core of a cluster.

The galaxies within the caustic diagram lie within the sphere of influence of the cluster which can extend up to several virial radii. As the galaxies fall into

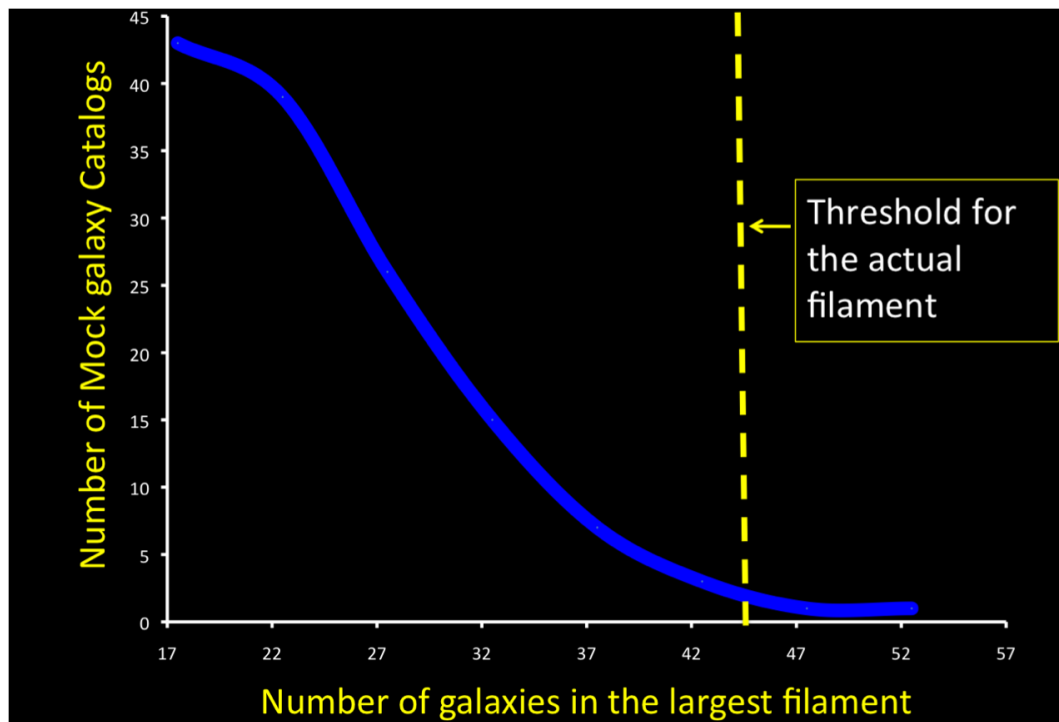


Figure 20: Confidence Level For Friends-Of-Friends Algorithm obtained using the Markov Chain Monte Carlo technique by generating 200 catalogs of galaxies. The catalogs are created by assigning random angular values that correspond to the radial distances of our original galaxy catalog. The confidence level is then determined by counting the number of galaxy catalogs whose longest filament contains at least as many galaxies as the original catalog of galaxies.

Abell 1882 accelerated by the gravitational potential of the SuperGroup, they reach the maximal velocity as they transit the cluster for the first time. Hence the galaxies within the virial radius, with high velocities, lying along the caustics are currently falling into the SuperGroup potential for the first time. They will eventually become virialized members of the cluster and will be in tight orbits around the cluster. The infall and the orbiting of galaxies together produce the trumpet shaped velocity profile in a cluster region. Some galaxies exhibit low line-of-sight velocities and lie well within the virial radius with line-of-sight velocity $\leq 1\sigma$. These might be galaxies that have been accreted at an earlier time when the cluster mass was much lower and hence had lower infall velocity. They might have further slowed down due to dynamical friction at the core. These galaxies might have also formed locally. There are also those galaxies that are close to the pericenter, and might be the backsplash galaxies that have completed their first pericenter and are now looping outward ([69], [83]).

In the SuperGroup Abell 1882 where the structures are extremely clumpy and diverse over a large dynamical and spatial scale, with possible degeneracy between Σ and projected cluster-centric radius, caustics provide a unique opportunity to trace the sub-structures and mass profile by creating a map of the SuperGroup core along with its feeding filaments which are otherwise difficult to detect. And since the caustics method is independent of the dynamical state of the system, recent mergers etc. do not affect the results. With multi-object spectroscopy, we have a large set of galaxies to which the caustic method can be applied.

The width of the profile at a given projected radius gives us the escape velocity for a galaxy at that distance from the assumed SuperGroup center. The position of the galaxies within the caustics on the other hand, contain information about when

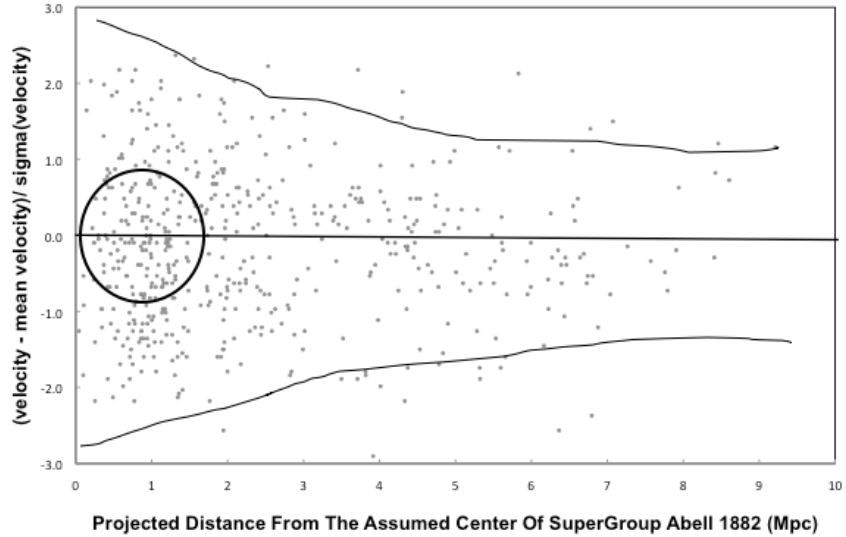


Figure 21: Caustic diagram of Abell 1882 showing the redshift of galaxies as a function of projected cluster-centric radius. The trumpet shaped velocity profile is due to the combination of infall and the orbiting of galaxies in a cluster region. The galaxies with high velocities, lying along the caustics, are currently falling into the SuperGroup potential for the first time. Galaxies with low line-of-sight velocities within the virial radius, denoted by the circle, have been accreted at an earlier time. The galaxies close to the pericenter might be the backsplash galaxies that have completed their first pericenter and are now looping outward.

it was accreted into the SuperGroup. The process of galaxy accretion in a cluster is along preferred directions (i.e. anisotropic along the filaments) and are episodic. Cluster outskirts can also host strong tidal fields. Besides, most accreted galaxies reside in groups within the filaments, and have their own internal motions. Hence the assumption of a simple spherical infall model due to gravitational instability is not satisfied in the cluster outskirts.

The caustic diagrams assume spherical symmetry of the infalling structure. However, most of the real clusters cannot be approximated as such. The caustic mass derived from such a diagram may vary with the observed orientation of the structure. Hence the uncertainties on the caustics are due to projection

effects. The caustic pattern appears to be robust for galaxies of all mass and brightness (see also Geller et al. 1999). It does not require the baryonic and the dark matter components to be in a dynamical equilibrium ([25]). The caustics require the galaxy co-ordinates and their redshifts only, and hence structure determination using this technique is independent of the mean cluster redshift. X-Ray mapping, optical scaling and Sunyaev-Zeldovich scaling relations provide masses within a radius that is smaller than the virial radius and hence do not give us any information about the cluster outskirts. Besides, the X-Ray mass is unreliable in an unvirialized structure as Abell 1882. The caustic technique agrees very well with results of gravitational lensing. It is a powerful tool to study the complicated network of large scale structures much beyond the virial radius of a cluster/proto-cluster region.

6 RESULTS AND DISCUSSIONS

In Section 6.1, we discuss the color evolution of galaxies with projected radial distance and local galaxy density (Σ). Abell 1882 is highly clumpy and unvirialized. Therefore, ideally the two above mentioned parameters can be disentangled, and their effect on galaxy transformations can be studied separately as shown in Section 6.2. Section 6.1 shows a galaxy stellar mass dependence on the color evolution of the galaxies as they move from the low density outskirts to the high density core of Abell 1882. Section 6.3 compares the evolution of birth rate parameter within two different timescales and estimates the timescale for galaxy transformations for at least some of the low mass dwarf galaxies (between 0.3 – 1 Gyrs). It also identifies a set of dwarf galaxies which have been suddenly quenched very close to the groups in past 0.3 Gyrs. Using our spectral data, we have confirmed that these galaxies are not dusty starburst galaxies, which can cause the galaxies to appear more reddened photometrically. Section 6.4 discusses the occurrence of spectroscopically identified starburst, post-starburst and passive galaxies in the dynamic phase space of Abell 1882 (Section 6.4.1), density-radial distance phase space (Section 6.4.2) and color-color space (Sections 6.4.3, 6.4.4), and their implications in terms of galaxy transformation. Section 6.5 discusses the evolution of mean equivalent width of $H\alpha$ which is a proxy for star formation rate. It shows a suppression of star formation rate with increasing density and decreasing radial distance. In Section 6.6 we show that the spectroscopically identified starburst, post-starburst and passive galaxies exhibit a spatio-temporal sequencing, where most of the post-starburst galaxies appear within the high density groups, and the starburst galaxies appear in the group-infall region or within the filaments in the far outskirts.

6.1 Optical Color Evolution Of Galaxies With Projected Radial Distance and Local Galaxy Density (Σ)

Our results show that similar to the findings of the past three decades of the study of galaxy evolution, local galaxy density is the primary driving mechanism of galaxy transformation even in a highly complex and unvirialized structure like SuperGroup Abell 1882 (Figure 22 , Figure 23). The colors have been defined and obtained in Section 4. This is analogous to the morphology-density relation in rich clusters as shown by Dressler,1980 (Figure 16). However, due to the unique structure of this SuperGroup, it provides an interesting laboratory where secondary drivers of galaxy transformation may be disentangled.

From the results of Section 6.1.2, mass appears to be the second most dominant transformational effect after Σ . The lower the galaxy mass, the stronger is the forced evolution experienced by the galaxy as evidenced by its color evolution (Figures 26, 27). The moving average of galaxy color in each mass/color bin do not intersect and show distinct identifiable trends with projected radial distance and Σ .

The redward trend in the dwarf galaxies ($< 10^{9.5}M_{\odot}$) start at least as far out as 3 Mpc, much further out from the observed X-Ray emissions associated with the groups (Figure 27), indicating that the star-forming galaxies are being quenched even before they enter the groups. The blue color in $g - r$ for SDSS galaxies peak at ~ 0.4 ([11]). Hence, there is not much room for the moving average for the dwarf galaxies to go any bluer beyond 3 Mpc.

The highest mass bin (mass $>10^{10.5}M_{\odot}$) does not show any evolution as far out as 9 Mpc from the assumed center of the SuperGroup. Keeping with the 'archaeological downsizing' of galaxies, the star formation in more massive galaxies

tends to occur at an earlier epoch and over a shorter time span, and hence such galaxies a very low star formation rate at lower redshifts ([21], [100]). This effect is observed in elliptical galaxies in large surveys like Sloan Digital Sky Survey ([45], [50], [77]). This is consistent with our observation that we detect practically no color evolution in the most massive galaxies.

The projected radial distance-color correlation appears to have a second order effect on the galaxy transformation (Figures 24, 25). The dependence of projected radial distance-color can be observed even when we remove the Σ dependence and select galaxies within a narrow density range (Figure 38) as shown in Section 6.2.

We have used running mean or forward moving average to determine the trends in our data. It smoothens out data fluctuations over shorter scales/bins and emphasizes large scale trends. Given a sequence of values $\{a_i\}_{i=1}^N$, an n -moving average is given by a new sequence of values $\{s_i\}_{i=1}^{N-n+1}$. It is calculated by taking the arithmetic mean of subsequences of terms in a_i ,

$$s_i = \frac{1}{n} \sum_{j=1}^{i+n-1} a_j \quad (23)$$

6.1.1 Fractional Number Evolution Of Galaxies With Color

The optically red galaxies in $u-r$ and $g-r$ colors begin to dominate the galaxy population between $-3.5 < \log(\Sigma) < -2.5$ and continue to increase in fractional number with increasing Σ (Figure 22, Figure 23). The projected radial distance-color relation shows an over-abundance of red galaxies at least at a distance of 2 Mpc from the assumed center of the structure in both the optical colors (Figure 24, Figure 25). As evidenced from the figures, the fractional color of the galaxies shows a much stronger dependence on Σ as compared to that on the projected

radial distance. No color dependence on the radial distance can be observed at least beyond 4 Mpc.

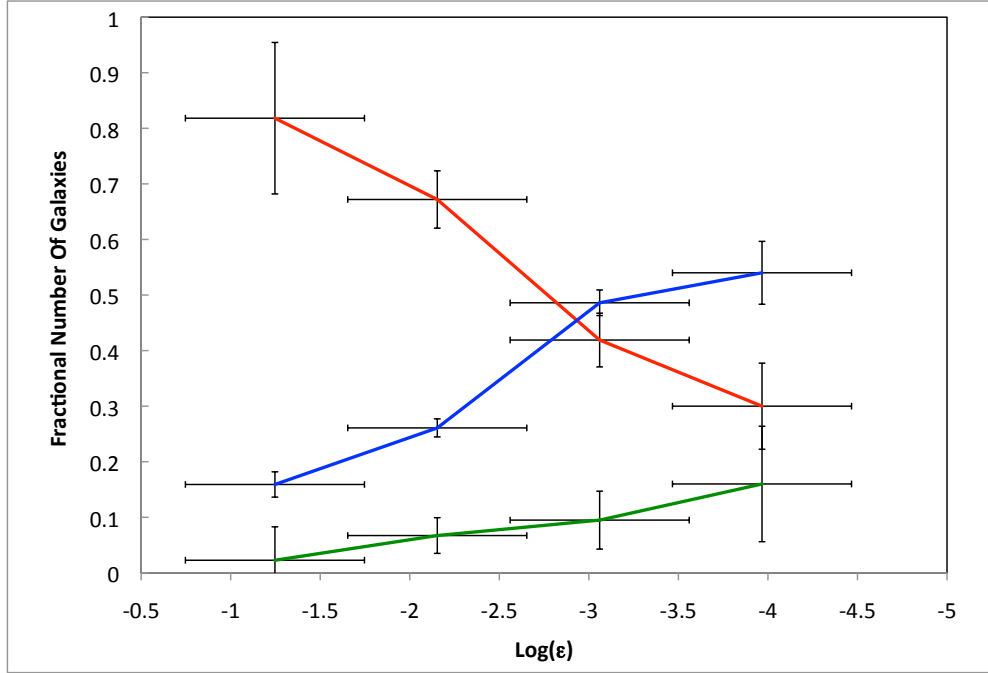


Figure 22: Fractional numbers of $g - r$ color plotted against Σ show that the color- Σ relation is sealed in Abell 1882. Red, blue and green lines denote the evolution of fractional numbers of red, blue and green galaxies respectively.

6.1.2 Mass Dependent Optical Color Evolution Of Galaxies

The moving average of optical ($g - r$) colors of the galaxies shows a significant redward trend with increasing Σ and decreasing projected distance from the assumed center of the system (Figures 26, 27) for galaxies with mass $< 10^{10.5} M_{\odot}$. This indicates a quenching of star formation as the galaxies approach the core and/or with increasing density. Interestingly, we detect the redward trend of the galaxies much beyond the detected X-ray clumps associated with the groups.

Color evolution appears to be much stronger in low mass dwarf galaxies (mass

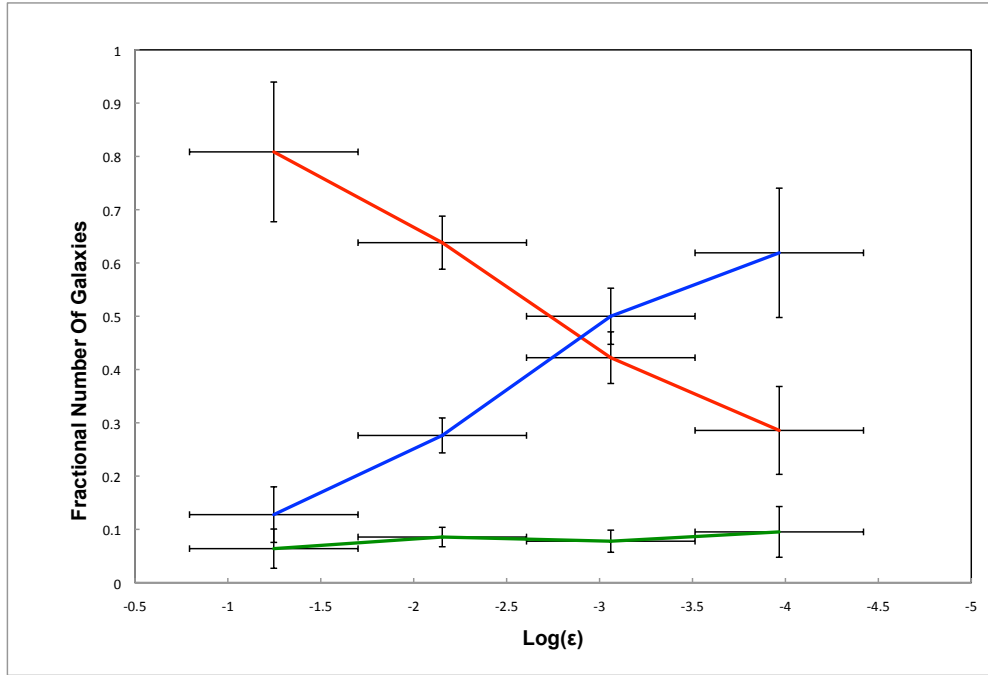


Figure 23: Fractional numbers of $u - r$ color plotted against Σ show that the color- Σ relation is sealed in Abell 1882. Red, blue and green lines denote the evolution of fractional numbers of red, blue and green galaxies respectively.

$< 10^{9.5} M_{\odot}$) as compared to the galaxies with mass between $10^{9.5} M_{\odot} < \text{mass} < 10^{10.5} M_{\odot}$. Hence, the lower mass galaxies show a stronger suppression of star formation as inferred from the observed redward trend in $g - r$ color, as compared to the intermediate mass galaxies. Additionally, the low mass galaxies exhibit a sharp redward trend at $\log(\Sigma) \approx -2.2$. This indicates star formation quenching within a short time scale ($< \text{few billion years}$). The intermediate mass galaxies also appear to show significant redward trend at the same Σ . Galaxies with mass $> 10^{10.5} M_{\odot}$ show little or no redward trend with increasing Σ and appear to have already moved on to the red sequence long before their accretion into the system.

For the dwarf galaxies, the mean $g - r$ color increases from ≈ 0.45 in the low density regions to ≈ 0.75 in the high density regions, with an average error

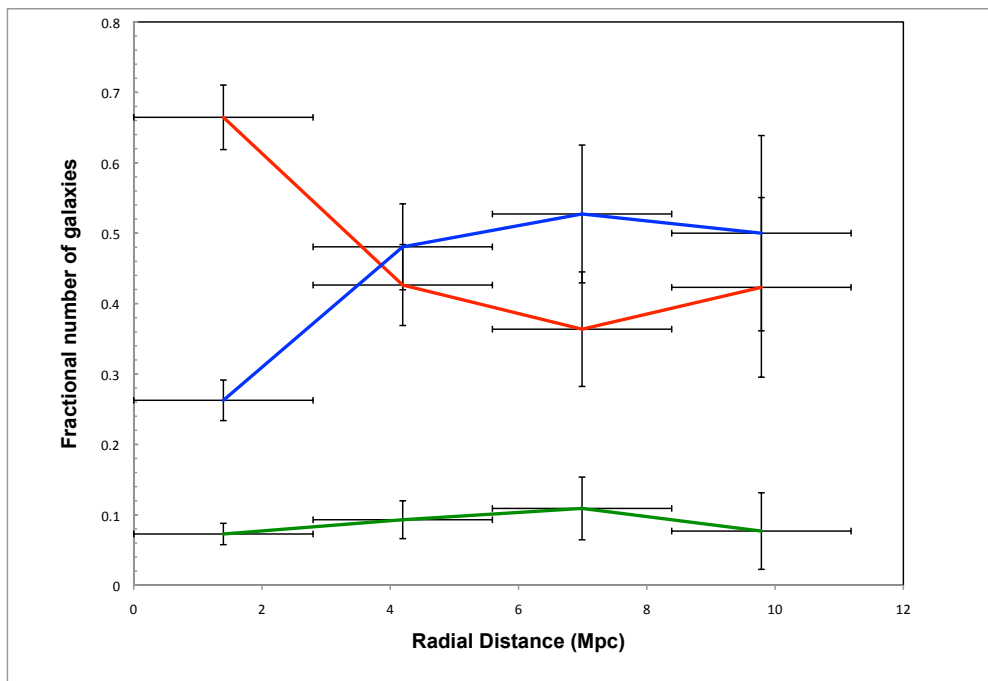


Figure 24: Fractional numbers of $g - r$ color plotted against projected radial distance show that the color is more strongly tied to the density parameter than the projected radial distance. Red, blue and green lines denote the evolution of fractional numbers of red, blue and green galaxies respectively.

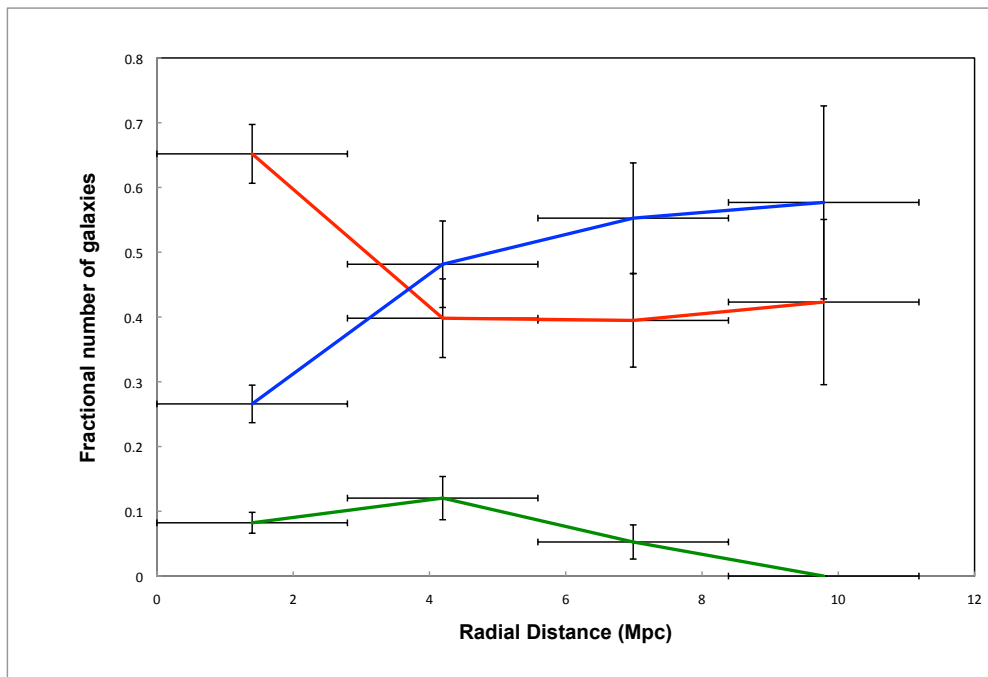


Figure 25: Fractional numbers of $u - r$ color plotted against projected radial distance show that the color is more strongly tied to the density parameter than the projected radial distance. Red, blue and green lines denote the evolution of fractional numbers of red, blue and green galaxies respectively.

in $g - r$ color of ≈ 0.112 , whereas for the intermediate mass galaxies the mean $g - r$ color increases from ≈ 0.8 in the low density regions to ≈ 1.0 in the high density regions with an average error in $g - r$ color of ≈ 0.025 . The projected radial distance-color has a mean $g - r$ color of ≈ 1 at the groups and $\approx 0.75 - 0.85$ beyond 3.5 Mpc, where the average error in $g - r$ color is ≈ 0.112 . For the dwarf galaxies the mean $g - r$ color increases from ≈ 0.4 in the cluster outskirts to ≈ 0.6 at the low radial distance. Whereas, for the intermediate mass galaxies the mean $g - r$ color increases from ≈ 0.8 in the outskirts to ≈ 1.0 at the low radial distance with an average error in $g - r$ color of ≈ 0.025 .

The color - projected radial distance plot clearly shows redward-peaks in galaxy color at 1 Mpc and 2 Mpc, which correspond to the projected distances of the groups from the center with a significant increase in Σ . Hence the redward trends in galaxy colors are possibly caused by to quenching of star formation which appears to be tied more strongly to the Σ than projected radial distance, and appears to be suppressed at high density regions. The high mass galaxies do not exhibit any significant trend with radial distance even as far out as 9 Mpc from the assumed center, and already appear to have merged into the red sequence possibly because they have used up their gas content to make stars early in their evolutionary history and are already quenched.

a. Optical Color Evolution Of Low Mass Galaxies As A Function Of Σ And Projected Radial Distance

The color-magnitude diagram for the dwarf galaxies shows that most of the dwarf galaxies are optically blue, and their red sequence is still in the process of being assembled (Figure 28).

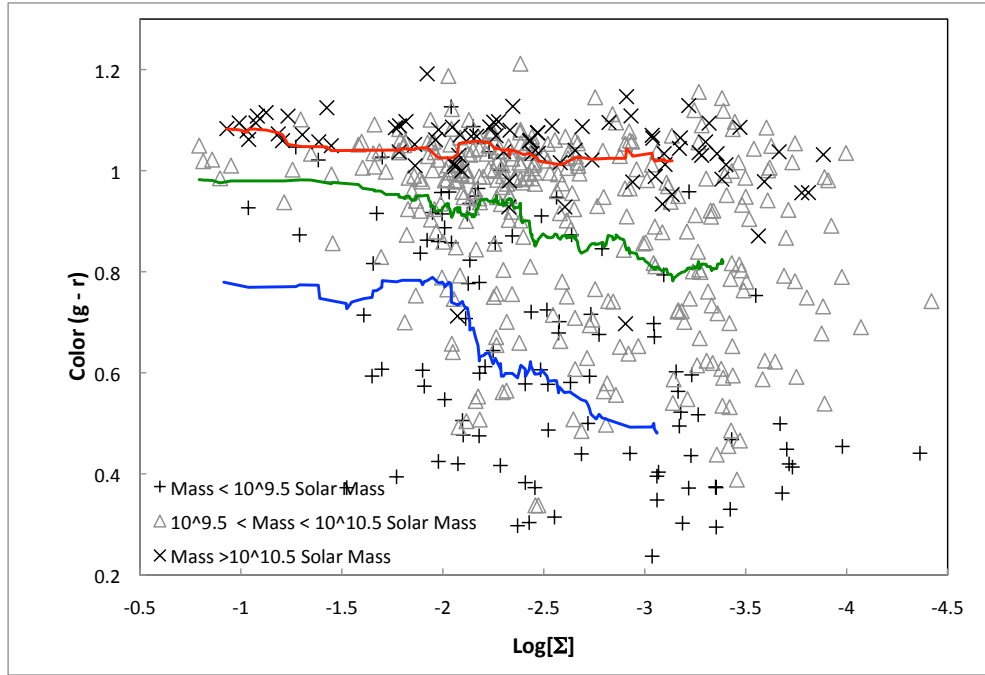


Figure 26: Moving average Of $g - r$ color plotted against Σ . Moving averages of low, intermediate and high mass galaxies are shown in blue, green and red respectively. The low mass galaxies ($M < 10^{9.5} M_{\odot}$) and the intermediate galaxies ($10^{9.5} M_{\odot} < M < 10^{10.5} M_{\odot}$) show redward trend of galaxy color with increasing Σ . The massive galaxies with mass $> M_{\odot}$ already appear to be quenched.

Figures 29, 30 show the optical color evolution of dwarf galaxies as a function of Σ and projected radial distance. The number of blue dwarf galaxies drastically decreases at $\log(\Sigma) \sim -2$, although they do not seem to have any radial distance preference. Mean color of the blue dwarf galaxies show a significant redward trend from a value of 0.4 at lowest Σ to 0.65 at the highest Σ , and redward trend from 0.4 at the outskirts to 0.6 in the groups.

All the red and green dwarf galaxies appear to be clustered at $-2.5 < \log(\Sigma) < -1$ and confined within a radius < 1.5 Mpc (shown in rectangular boxes in Figure 29 and Figure 30). This density range corresponds to the groups and the immediate infall region of the groups. This indicates that the dwarf galaxies

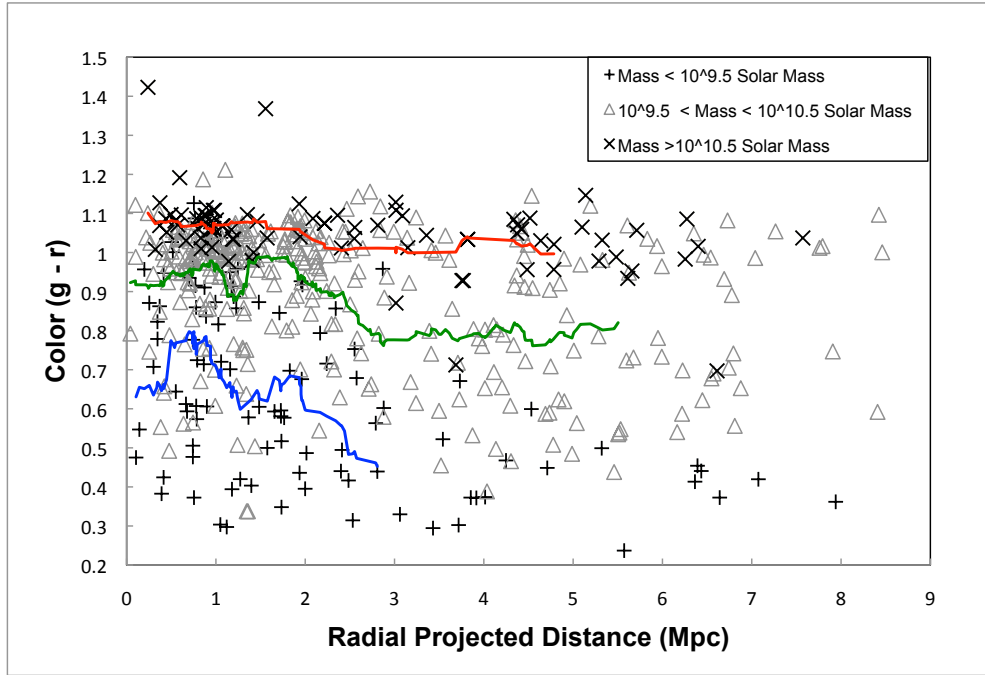


Figure 27: Moving average of $g-r$ color plotted against projected radial distance. Moving averages of low, intermediate and high mass galaxies are shown in blue, green and red respectively. The low mass galaxies ($M < 10^{9.5} M_{\odot}$) and the intermediate galaxies ($10^{9.5} M_{\odot} < M < 10^{10.5} M_{\odot}$) show redward trend of galaxy color with increasing projected radial distance. The peaks denote redward trend due to higher density regions implying a stronger density-color correlation as compared to the color-projected distance correlation. On the other hand, the massive galaxies with mass $> 10^{10.5} M_{\odot}$ already appear to be quenched before the galaxies enter the SuperGroup environment.

are quenched in the high density groups. This is unlikely due to a selection effect since one is more likely to detect faint red dwarf galaxies in the sparsely populated outskirts. No significant color evolution is observed for red dwarf galaxies.

b. Optical Color Evolution Of Intermediate Mass Galaxies

In the intermediate mass range, the red sequence is well formed as seen from the color-magnitude relation (Figure 31). There is also a significant blue cloud

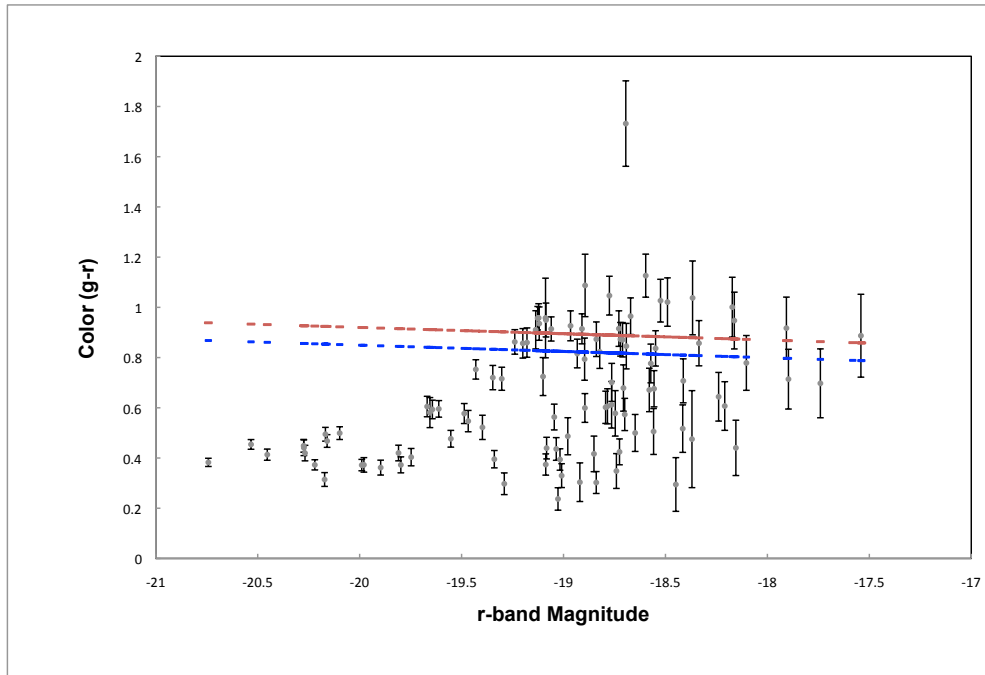


Figure 28: Color-Magnitude Diagram for dwarf galaxies. The red line shows the lower cut of for the red sequence galaxies. The blue line shows the upper cut for blue cloud galaxies. Most galaxies lie in the blue cloud (Best fit recipes obtained from Baldry et al., 2004 [2]).

population. Similar to the dwarf galaxies, there appears to be a lack of optically blue intermediate mass galaxies at $\log(\Sigma) < -2$. The intermediate mass red galaxies mostly cluster at a projected radial distance of less than 3 Mpc (see rectangular box in Figure 33). The color evolution within the intermediate mass regime is not very obvious (Figure 32 and Figure 33).

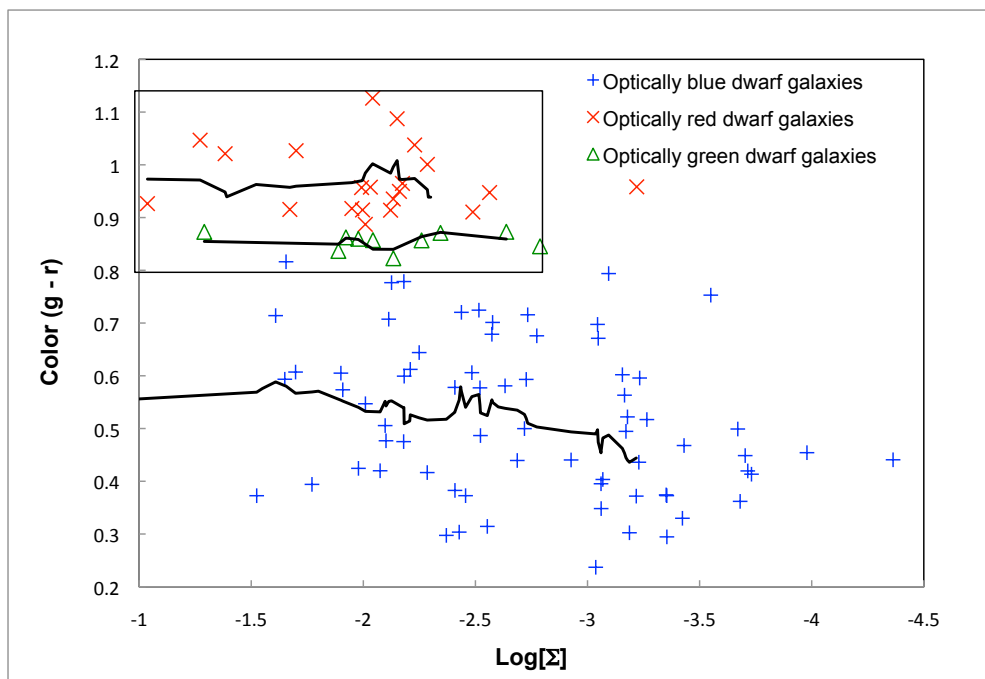


Figure 29: Moving averages of blue, green and red $g - r$ color plotted against Σ for dwarf galaxies ($M < 10^{9.5} M_{\odot}$) are shown in black. All but one optically red and green galaxies are confined within high density region shown by the black rectangular box.

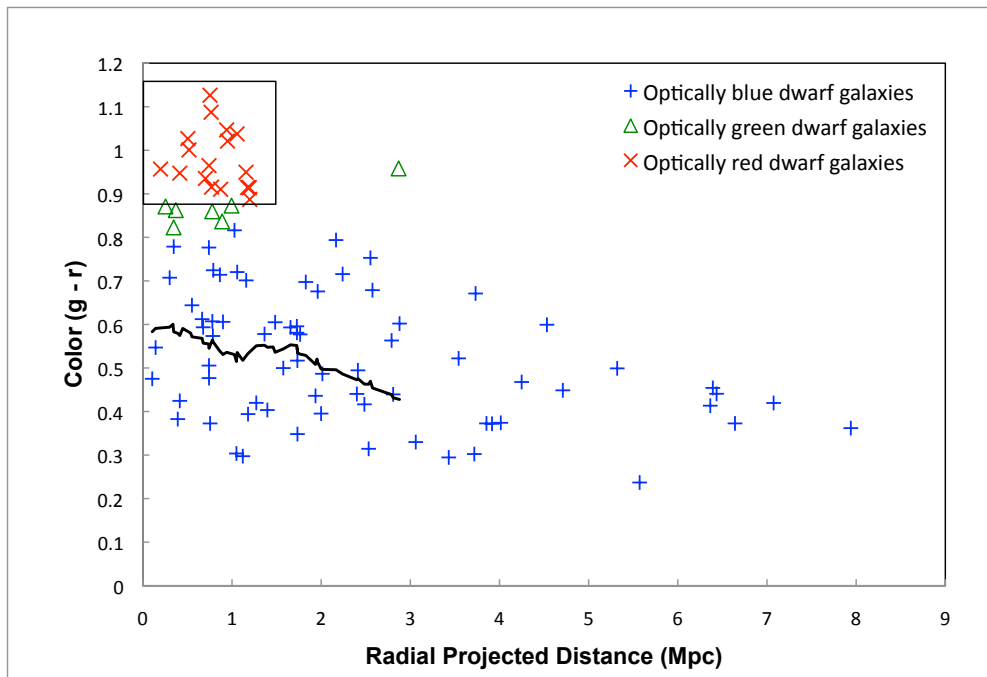


Figure 30: Moving averages of blue, green and red $g - r$ color plotted against projected radial distance for dwarf galaxies ($M < 10^{9.5} M_{\odot}$) are shown in black. All but one optically red and green galaxies are confined within a small projected distance from the assumed center, shown by the black rectangular box.

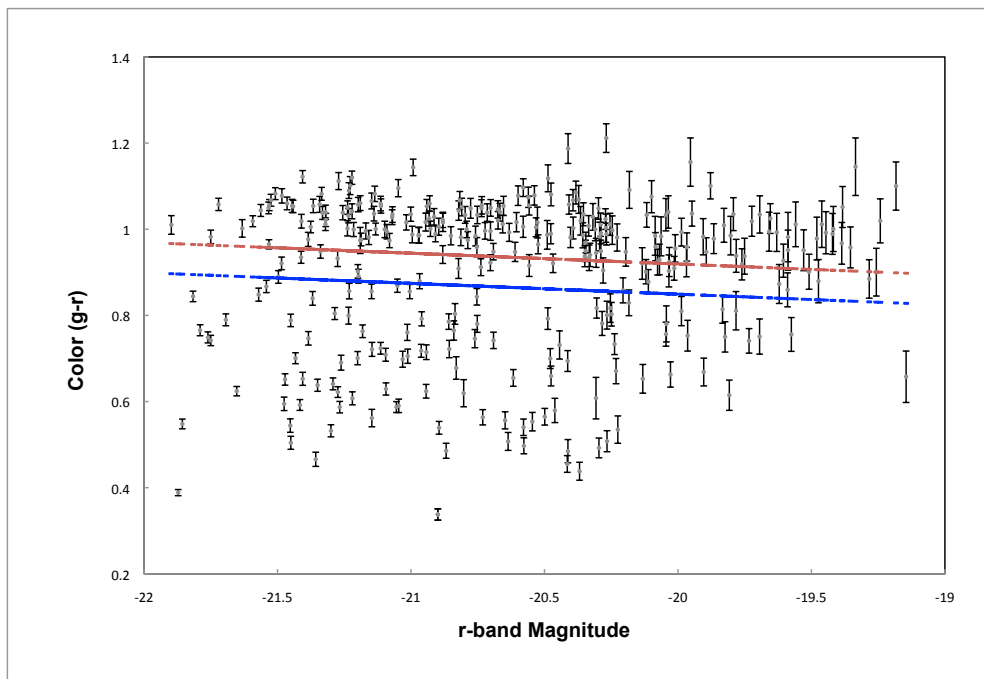


Figure 31: $(g-r)$ color-magnitude diagram for intermediate mass galaxies of Abell 1882. The red line shows the lower cut of for the red sequence galaxies. The blue line shows the upper cut for blue cloud galaxies. Most galaxies lie in the red sequence (Best fit recipes obtained from Baldry et al., 2004 [2]).

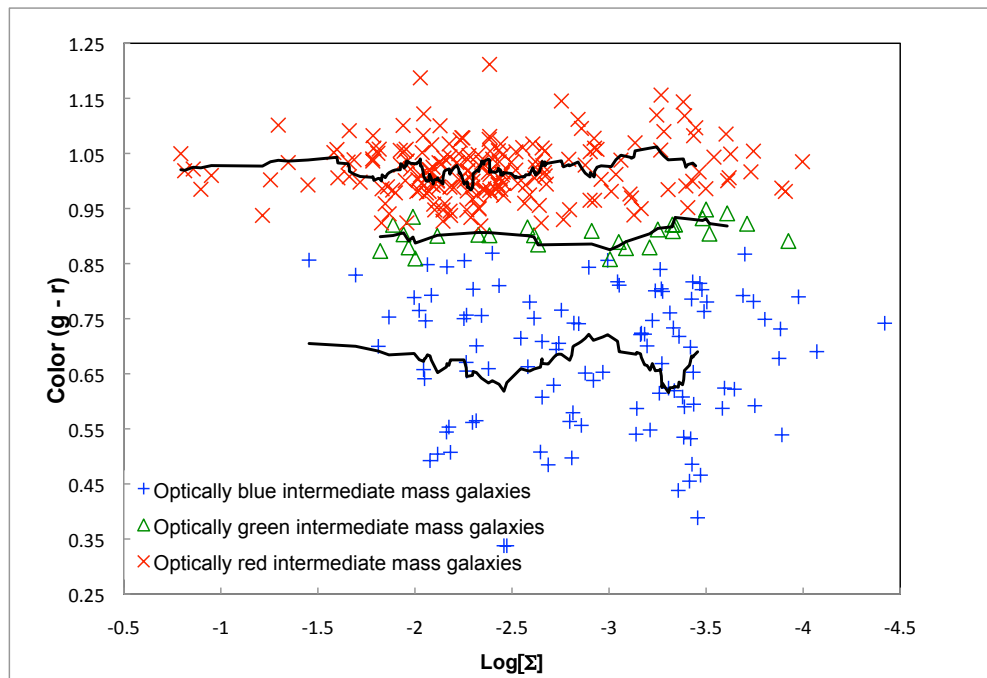


Figure 32: Moving averages of blue, green and red $g - r$ color plotted against Σ for intermediate mass galaxies ($10^{9.5}M_{\odot} < M < 10^{10.5}M_{\odot}$) are shown in black.

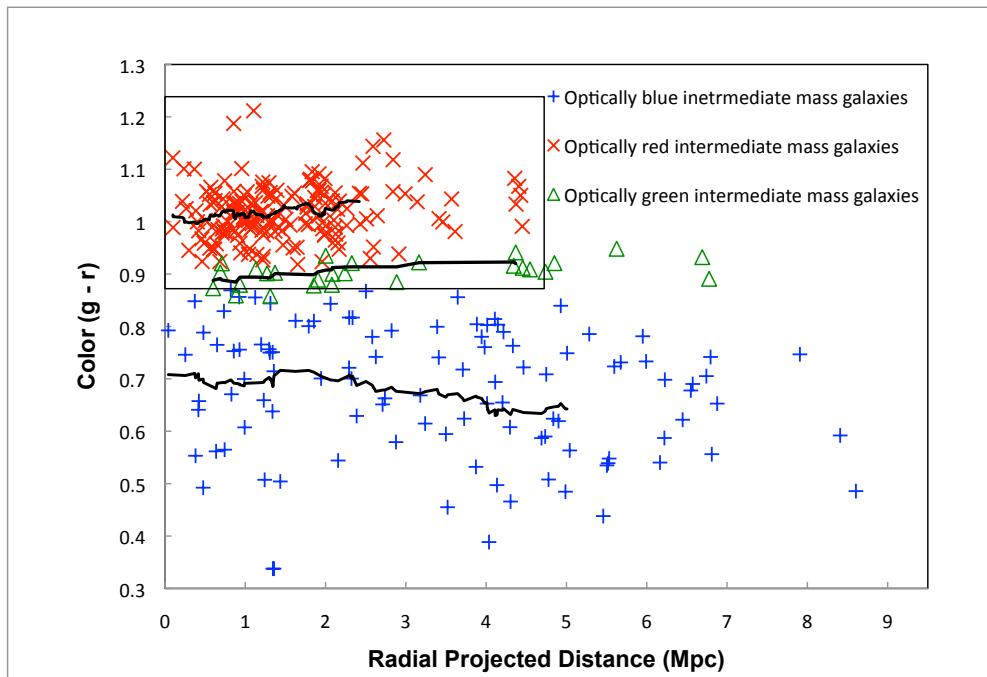


Figure 33: Moving averages of blue, green and red $g - r$ color plotted against projected radial distance for intermediate mass galaxies ($10^{9.5}M_{\odot} < M < 10^{10.5}M_{\odot}$) are shown in black.

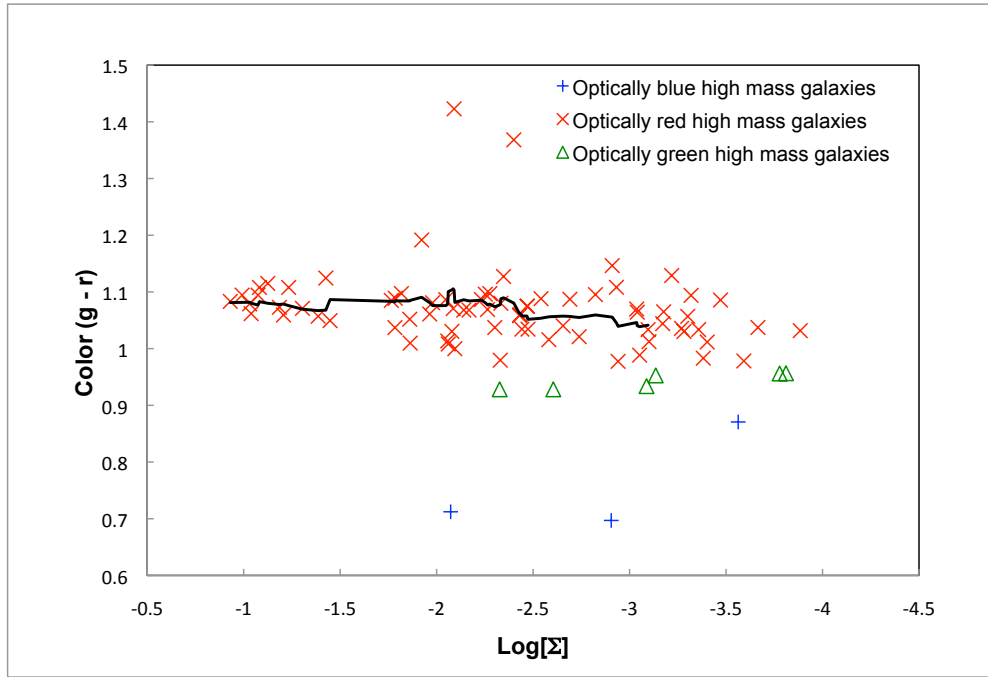


Figure 34: Moving average of $g - r$ Color - Σ for high mass galaxies ($M > 10^{10.5} M_{\odot}$). Running mean for optically red galaxies is plotted in black.

c. Optical Color Evolution Of High Mass Galaxies

Almost all the high mass galaxies are optically red in $g - r$ color. It has a well formed red sequence Hence the evolution of blue cloud galaxies to the red sequence appears to be almost complete in this mass regime. The high mass galaxies may have possibly reached a threshold potential beyond which any accreted gas is shock heated and fail to cool down enough to form stars (Figure 34 and Figure 35)

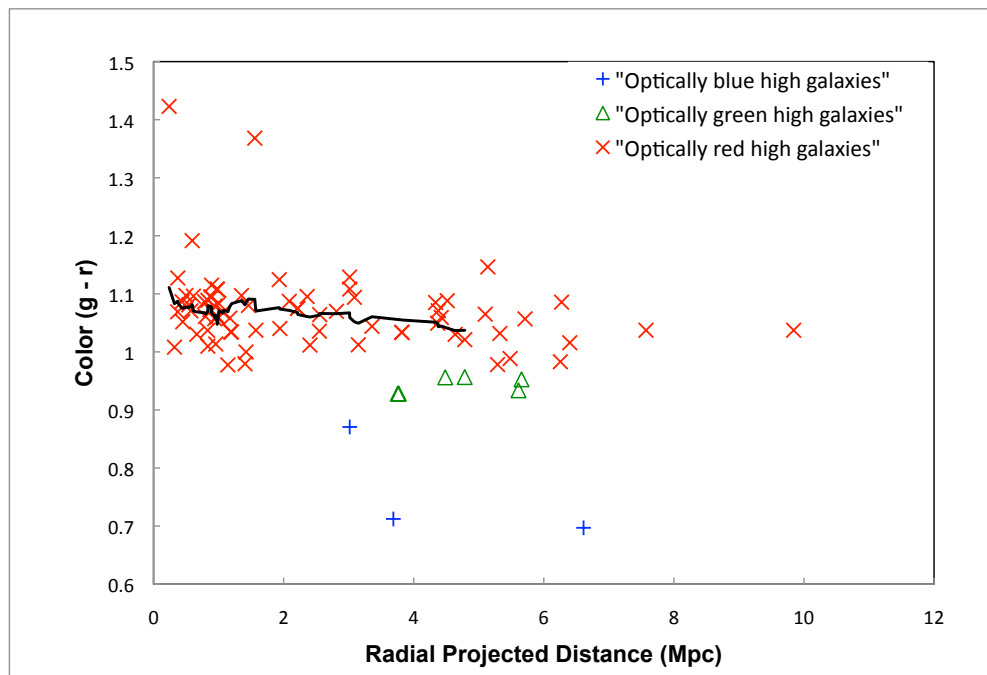


Figure 35: Moving average of $g - r$ Color - projected radial distance for high mass galaxies ($M > 10^{10.5} M_{\odot}$). Running mean for optically red galaxies is plotted in black.

6.2 Disentangling Local Galaxy Density (Σ) Effect And Projected Radial Distance Effect On Galaxy Transformations

We observe a second order effect of radial distance on galaxy color transformation even after removing the first order effect of Σ . In order to isolate the transformational effects due to the projected distance of a galaxy from the SuperGroup core and the Σ , we select galaxies within a narrow range of local galaxy density ($-3.5 < \log(\Sigma) < -2.5$) (Figure 36). Within this narrow Σ range we do not see any color evolution with Σ (Figure 37). However, the dwarf and intermediate mass galaxies show significant trend towards red in $g-r$ color at small radii (Figures 38, 39). The fractional number of blue galaxies dominates the outskirts of the SuperGroup, whereas the gap between the fractional number of red and blue galaxies closes near the groups.

6.3 Birth Rate Parameter Evolution Of Galaxies

The birth rate parameter is defined as the star formation rate in a galaxy averaged over total integrated star formation history and is expressed as follows,

$$b_{300} = \frac{\int_0^{0.3Gyr} SFR(t) dt}{\int_0^T SFR(t) dt} \quad (24)$$

$$b_{1000} = \frac{\int_0^{1Gyr} SFR(t) dt}{\int_0^T SFR(t) dt} \quad (25)$$

where T is the age of the Universe. Birth rate parameters can be thought of as specific star formation rate (star formation rate scaled by stellar mass of the galaxy) over different time scales. We have obtained the birth rate parameters from the KCORRECT package. This package determines birth rate parameters

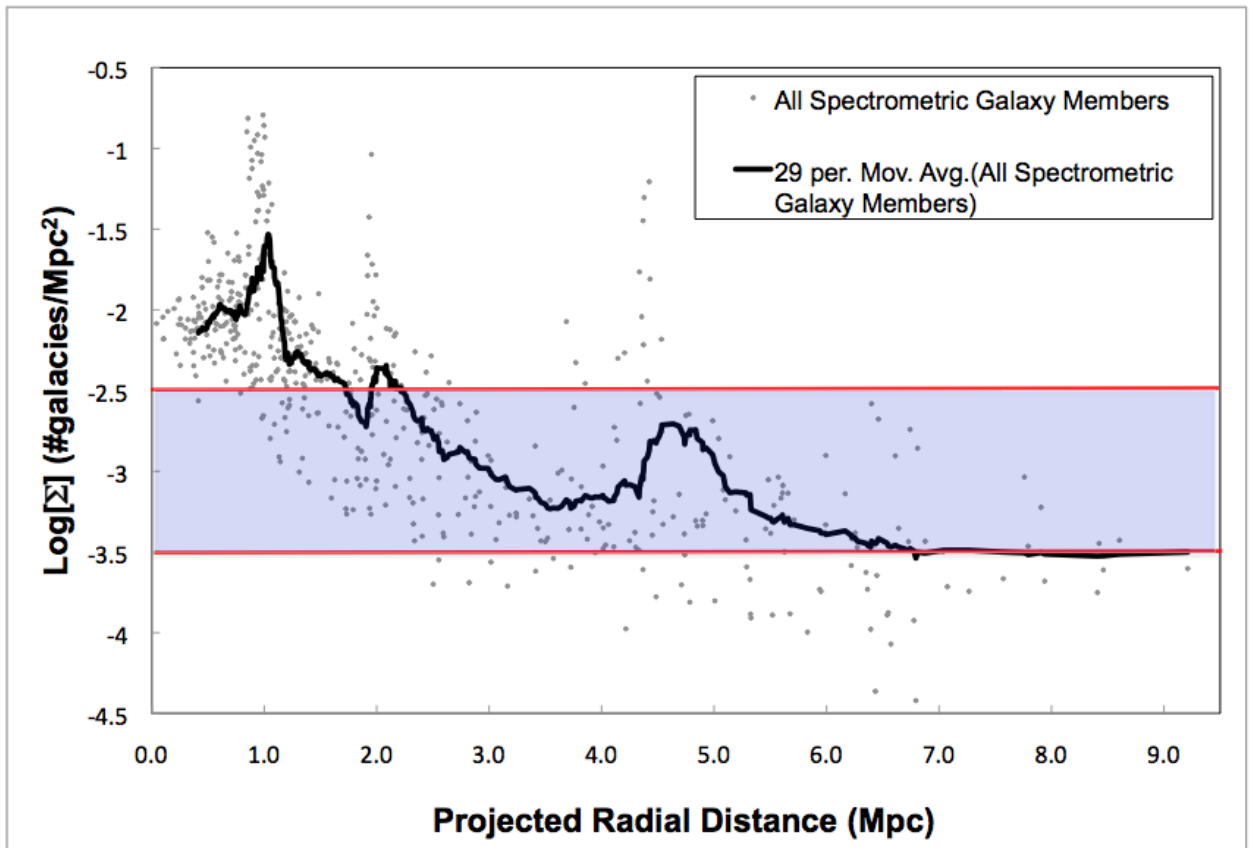


Figure 36: The figure shows the color- projected radius relation in a narrow range of local galaxy density selected in shaded region, and sampled as far out in the radial bin in order to disentangle the effect of projected radial distance from the local galaxy density.

based on the fitting templates to arbitrary sets of spectra and broadband fluxes to each galaxy, thus recovering a small set of templates based on models. The nonnegative linear combinations of these templates can explain a much larger set of inhomogeneous observations.

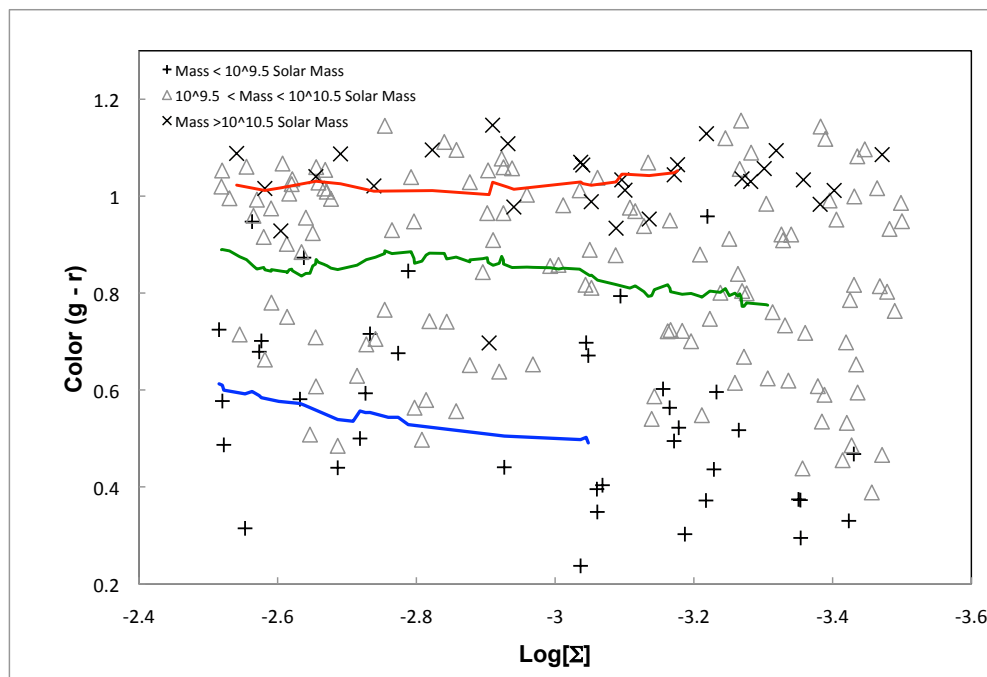


Figure 37: Moving average of $g-r$ color - Σ within the narrow range of Σ . Moving averages for dwarf, intermediate and high mass galaxies are plotted in blue, green and red respectively.

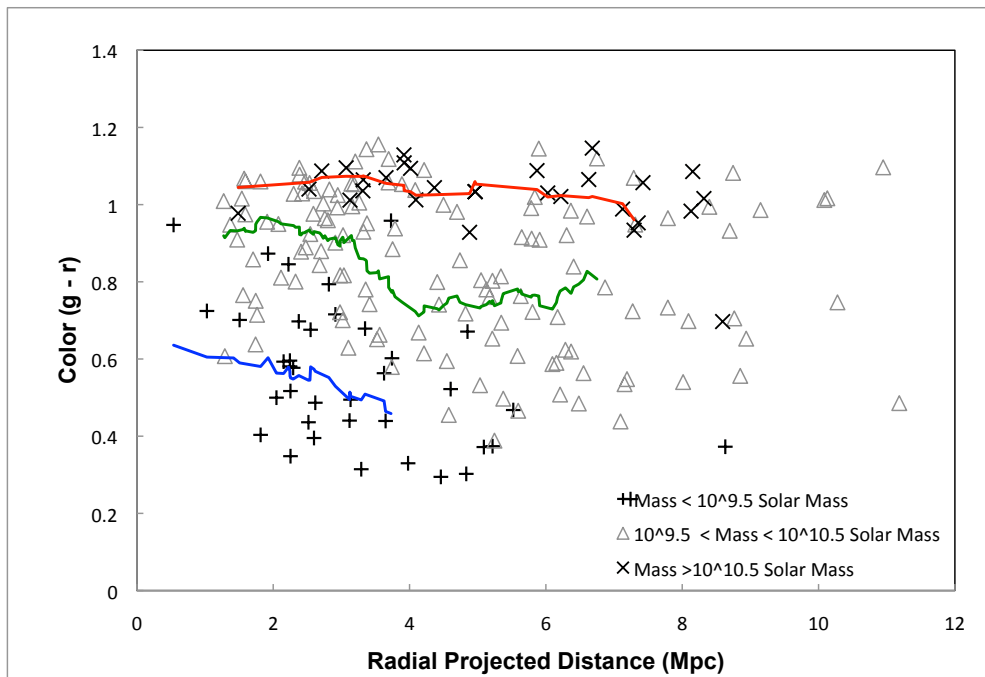


Figure 38: Moving average of $g-r$ color - projected radial distance within the narrow range of Σ . Moving averages for dwarf, intermediate and high mass galaxies are plotted in blue, green and red respectively.

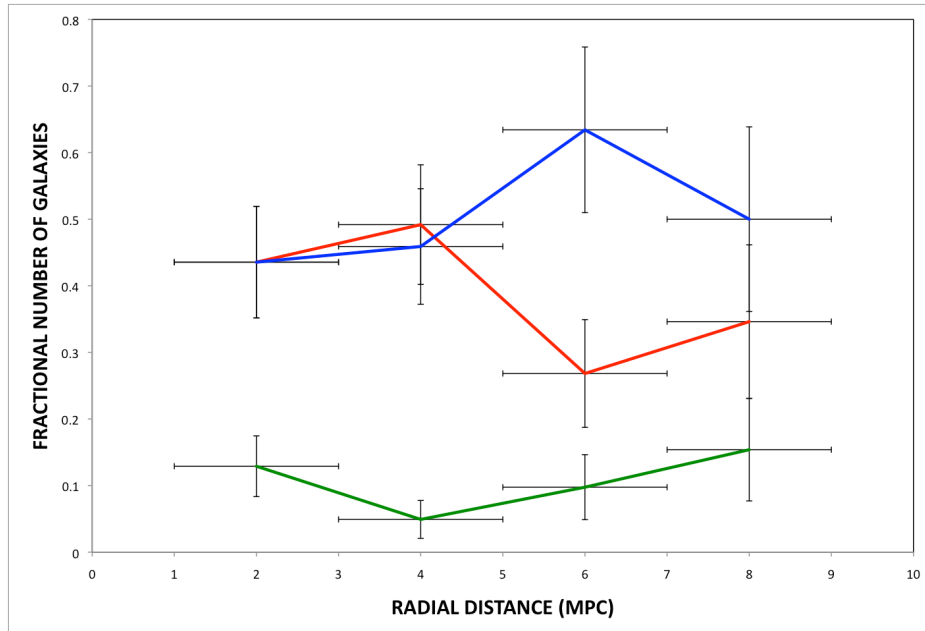


Figure 39: The fractional color evolution of galaxies plotted against projected radial distance. Red, blue and green lines denote the evolution of fractional numbers of red, blue and green galaxies respectively. Error bars represent Poisson statistics.

6.3.1 Birth Rate Parameter Evolution Over Past 300 Myrs (b_{300})

The birth rate parameter evolution over past 300 Myrs shows a drop in the star formation rate at all mass ranges with increasing Σ and decreasing projected radial distance (Figures 40, 41). More interestingly, we observe a bimodality in b_{300} in the dwarf galaxies. Although the mean b_{300} for the dwarf galaxies is higher than that of intermediate and high mass galaxies, we observe about 22 galaxies (out of which, we have spectroscopic information for 16 galaxies) with extremely low value of b_{300} within $-3 < \log(\Sigma) < -1$ at projected radial distance of less than 2 Mpc from the assumed center of Abell 1882. At least some of these galaxies are dusty starburst galaxies as indicated by the strong EW[H α]. However most of these galaxies are passive and at least two are k+a galaxies. This indicates

a significant suppression of star formation rate in past 300 Myrs in at least the dwarf galaxies in the vicinity of the groups.

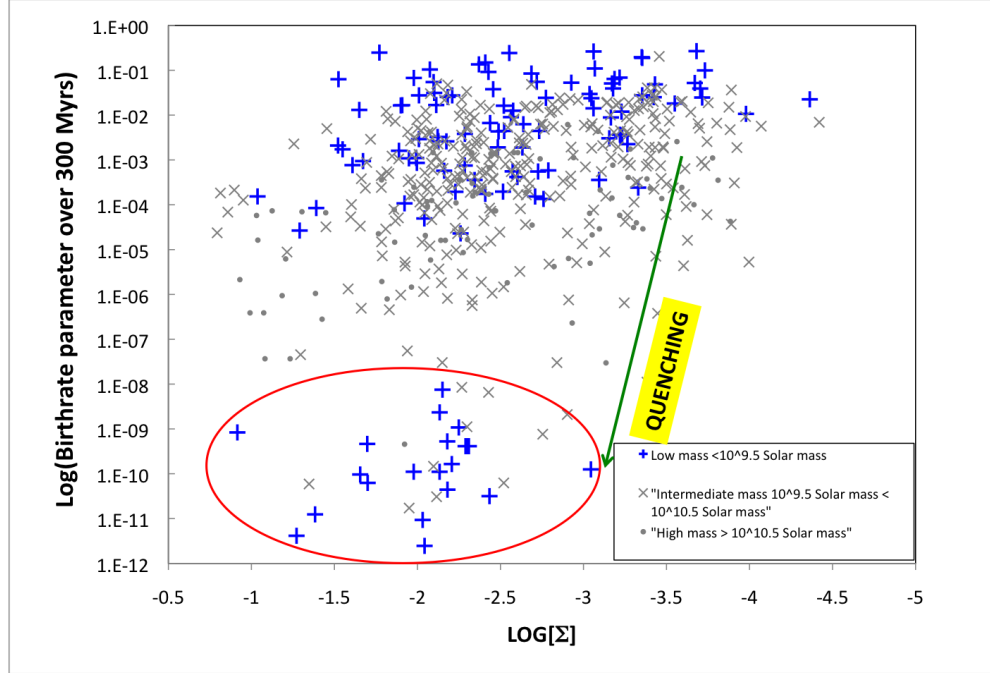


Figure 40: Birth rate parameter over B300- Σ . A clear bimodality in the birth rate parameter of dwarf galaxies over past 0.3 Gyrs due to quenching can be observed.

6.3.2 Birth Rate Parameter Evolution Over Past 1 Gyr (b_{1000})

The birth rate parameter evolution over past 1000 Myrs show a similar trend in b_{1000} for both high and intermediate mass galaxies. However, one can clearly see the dwarf galaxies migrating to the low birth rate regime close to the groups in similar Σ and projected radial distance range as in b_{300} (Figures 42, 43).

Section 6.3.1 and Section 6.3.2 indicate a temporal sequence where we are likely observing a thorough quenching of star formation in some of the dwarf galaxies close to the group environment within past 300 -1000 Myrs. These galaxies lie mostly in the groups or very close to them (Figure 44).

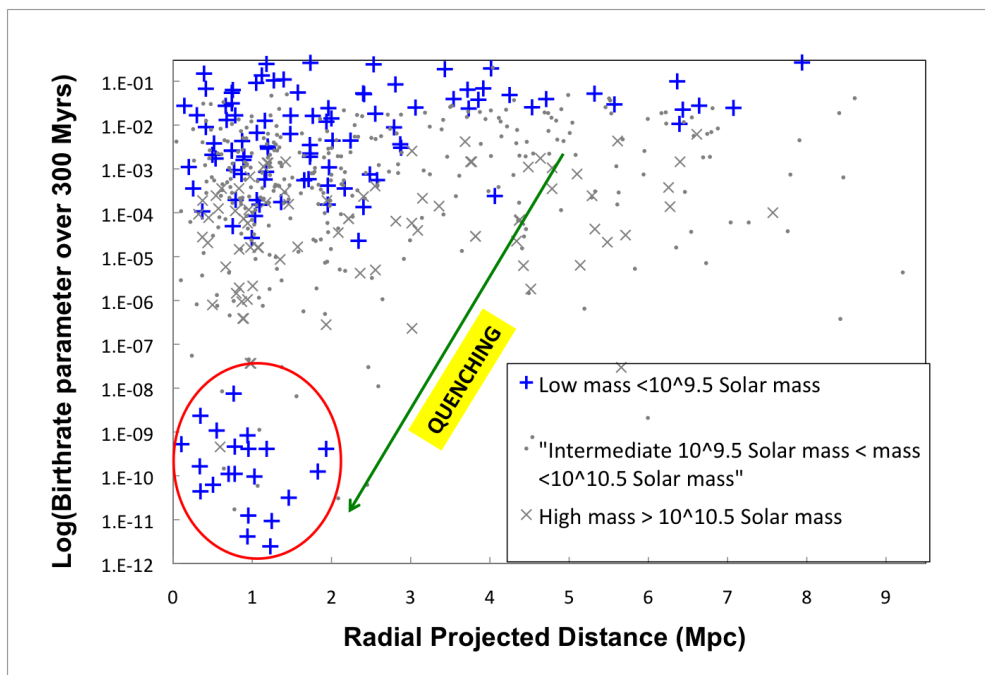


Figure 41: B300-Projected Radial Distance for all galaxies. Quenching over past 0.3 Gyr is much more tightly correlated with the radial distance than the local galaxy density.

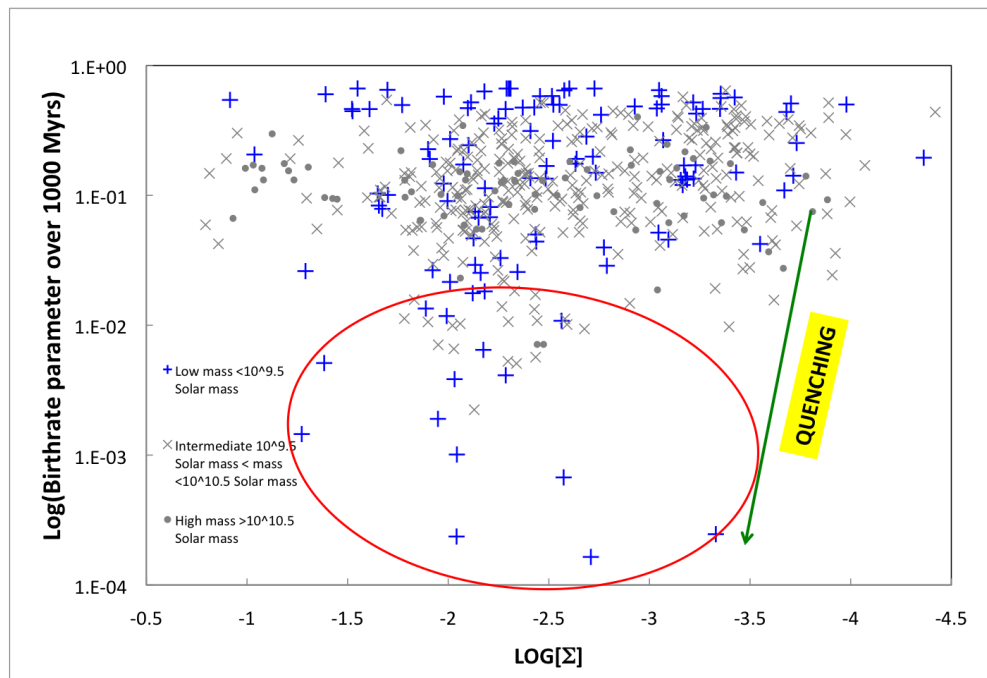


Figure 42: B1000- Σ for all galaxies. Blue plus signs represent the dwarf galaxies which show a gradual quenching at the higher local galaxy density.

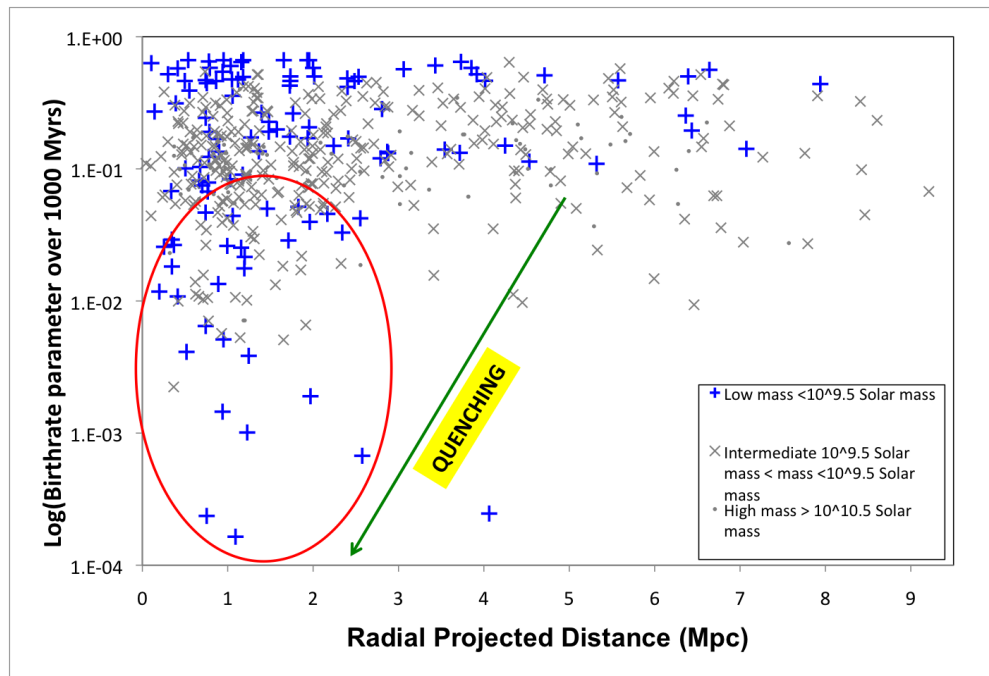


Figure 43: B1000-Projected Radial Distance for all galaxies. Blue plus signs represent the dwarf galaxies which show a gradual quenching near the groups.

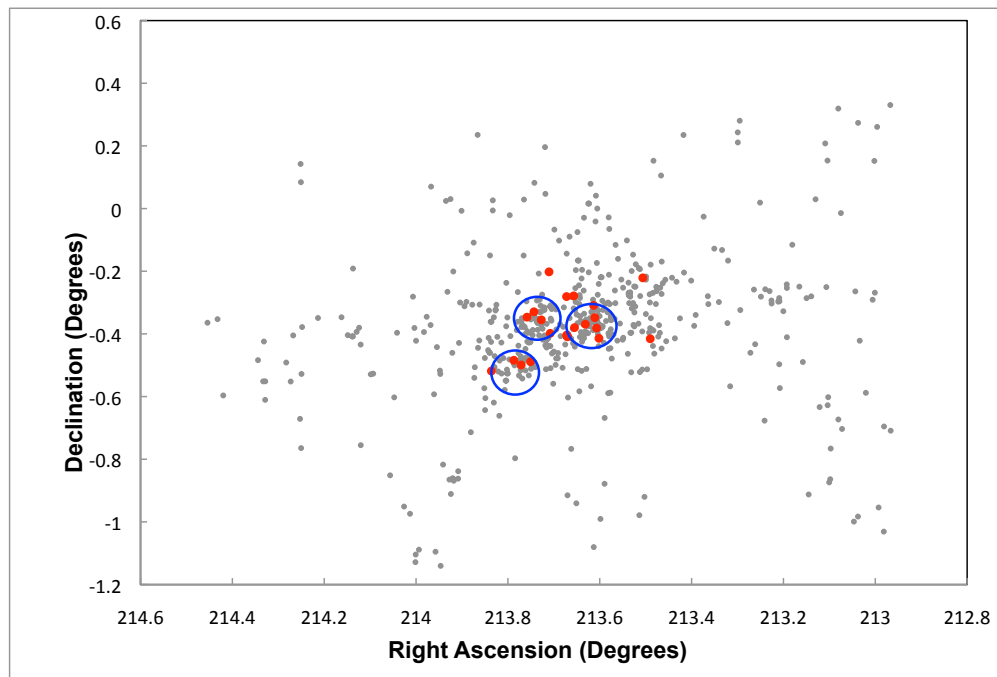


Figure 44: The red dots show spatial location of the dwarf galaxies showing very low birth rate parameter ($\log(B_{300}) < -7$) over past 0.3 Gyr. The grey dots represent all the galaxies in the catalog.

6.4 Photometric Evolution And Spectral Data

This section ties the results obtained from the photometric data and the spectroscopic data. Photometric colors reflect longer dynamic timescales (in the order of Gyrs), whereas spectral features reflect much shorter time scales (few Myrs to a Gyr). Hence, spectral features can identify the spatial and temporal scales for transformations in the system much more accurately. We have plotted the positions of starburst galaxies, post-starburst galaxies and low b_{300} dwarf galaxies on the photometric figures in order to tie the redward trend of galaxies with their spectral features.

One of the striking observations in this section is the clustering of the quenched or quenching galaxies (k+a and low b_{300} galaxies) at around $\log(\Sigma) \sim 2.2$, which coincides with the sharp and sudden redward trend of the low and intermediate mass galaxies (Figure 50). This indicates that the redward trend of galaxies at this density is at least partly due to these suddenly quenched galaxies. The low mass galaxies begin to show a redward trend at least from ~ 3 Mpc, which is a couple of virial radii away from center (Figure 51).

6.4.1 Caustics

The caustic diagram shows that some starburst galaxies occur away from the core, several virial radii away and/or along the edge of the trumpet shape (Figure 45). These are falling into the cluster for the first time. Most of the quenching or recently quenched galaxies reside well within the core of Abell 1882. At least some of these galaxies, that have low projected distance and low velocity dispersion, appear to have been accreted at an earlier time. None of these galaxies has a mass $> 10^{10.5} M_{\odot}$. Additionally, at least some of the starburst galaxies in

the infall region may be progenitors of the quenching or quenched post-starburst dwarf galaxies that reside in the deep recesses of the three groups that constitute the core of Abell 1882. There are three intermediate mass post-starburst galaxies at several virial radii away from the core. This indicates that at least in some cases, the quenching happens much before the initial infall for intermediate mass galaxies.

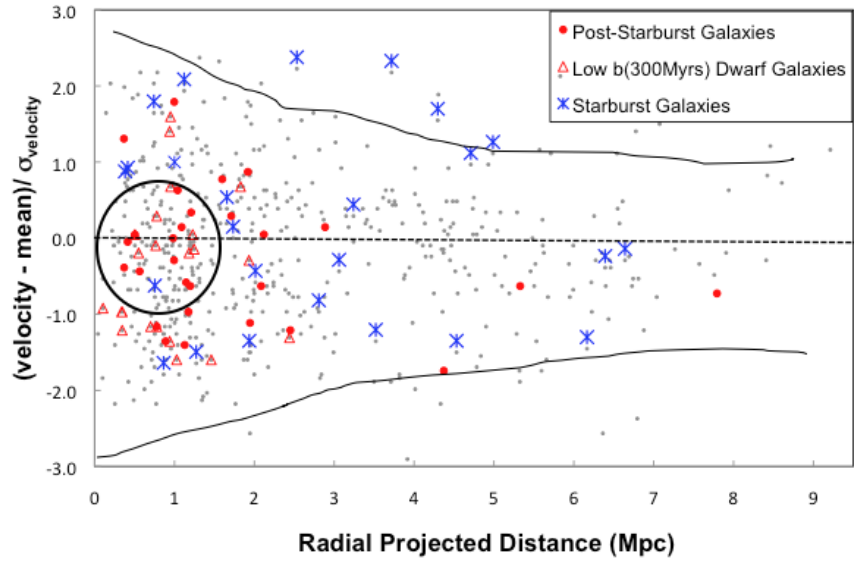


Figure 45: Caustic diagram of Abell 1882. The black circle represents the low velocity, low projected radial distance region. The lines represent approximate boundaries of the trumpet shaped caustic diagram.

6.4.2 Projected Radial Distance- Σ Relation

The radial distance - Σ structure of Abell 1882 is complicated. The galaxies migrate inward in distance and to higher Σ regions. Figure 46 show the starburst galaxies, post-starburst galaxies and the low b_{300} dwarf galaxies in the Σ -radial distance phase space. The k+a galaxies and the low b_{300} dwarf galaxies i.e. the quenching or recently quenched galaxies tend to mostly prefer the high density

peaks and are mostly confined to the groups which are denoted by the peaks in Σ at 1 and 2 Mpc respectively. The starburst galaxies populate out to at least 6.5 Mpc.

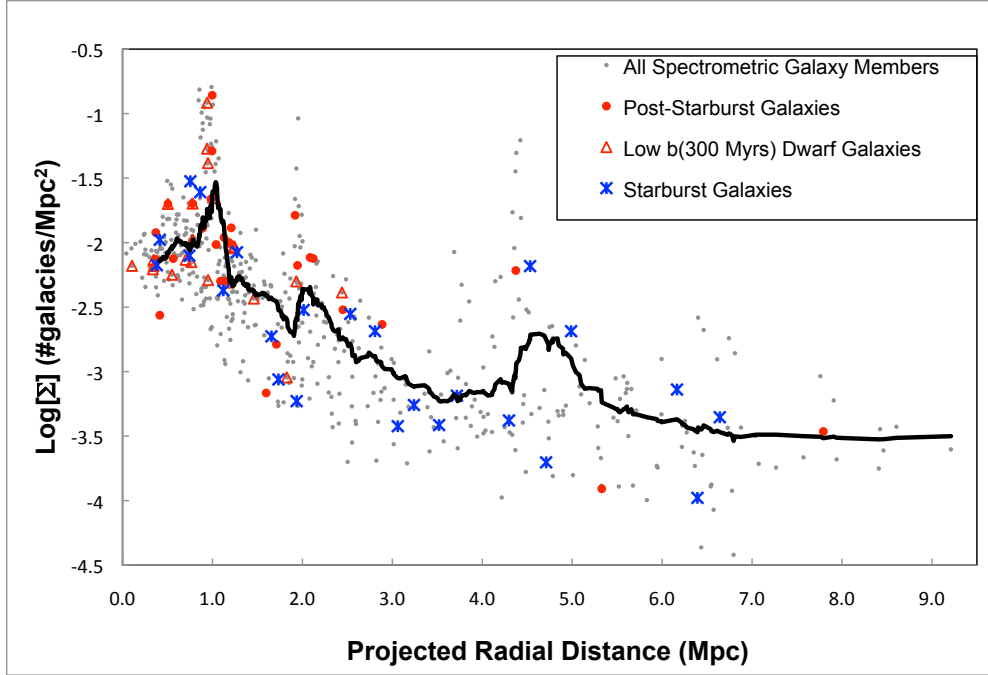


Figure 46: Projected Radial Distance- Σ Relation

6.4.3 Post-starburst Galaxies In Optical And UV Colors

The post-starburst galaxies have been plotted on the color-magnitude diagrams for $g - r$ (Figure 47), $u - r$ colors (Figure 48) and $NUV - r$ color (Figure 49). In the optical colors, almost all the post-starburst galaxies lie along the red sequence. However, in the $NUV - r$ color, most of the k+a galaxies occur in the green valley or blue cloud regions indicating more recent star formations. NUV is more sensitive to recent star formation is a much more powerful diagnostic of color distribution k+a galaxies.

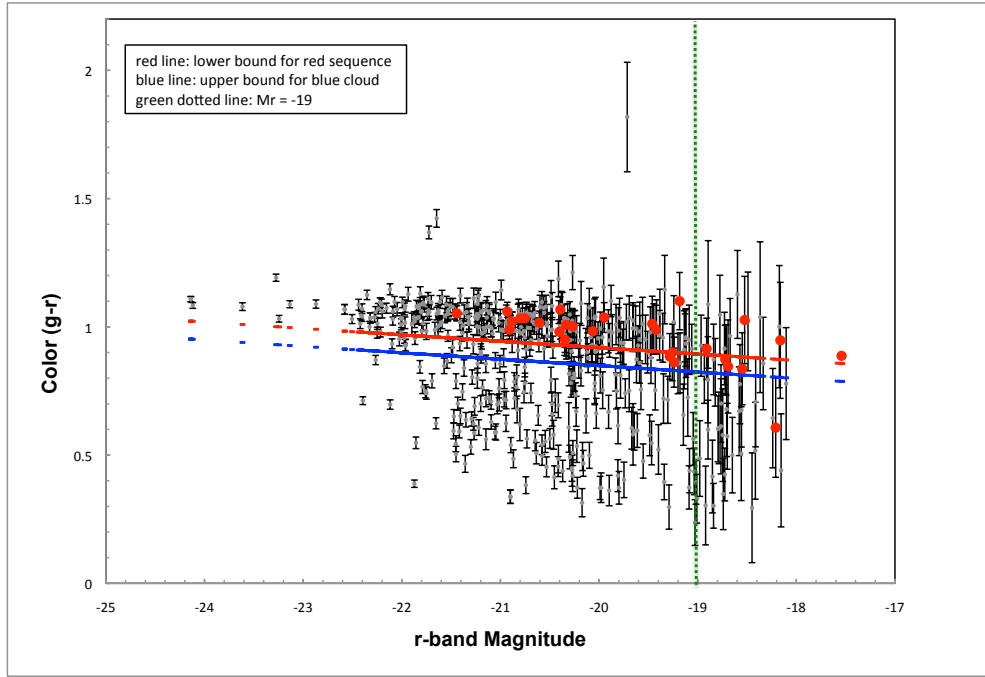


Figure 47: $(g-r)$ Color-mass relation with post-starburst galaxies plotted in red circles.

6.4.4 Optical Color Evolution Of Galaxies As A Function Of Σ And Projected Radial Distance

In Figure 50, post-starburst galaxies appear to cluster at $\log(\Sigma) \approx -2$, which coincides with the sharp redward trend of dwarf galaxies and the intermediate mass galaxies. The dwarf galaxies appear to be suppressed at the groups and the infall region since the post-starburst and low b_{300} galaxies are confined entirely within 2 Mpc from the assumed center of Abell 1882 and at $\log(\Sigma) > -2.5$ (Figure 52, Figure 53). There are very few starburst galaxies detected at this mass range and they extend all the way to the outskirts. For the intermediate mass galaxies however, the post-starburst galaxies can be found as far out as 8 Mpc, although most of them are confined within the groups or in the infall region of the groups (Figure 54, Figure 55).

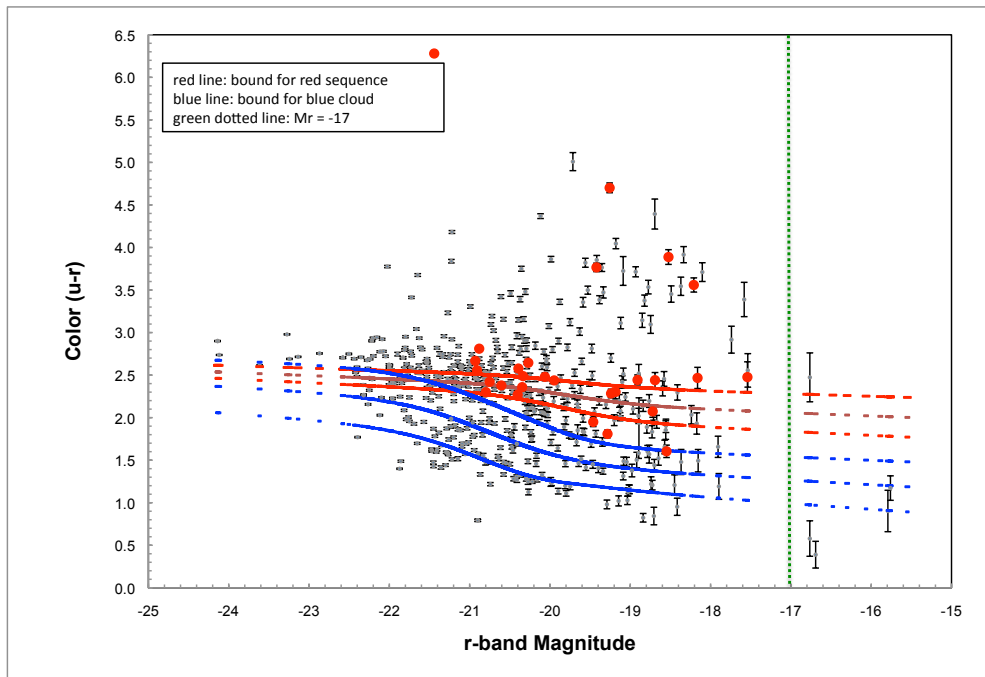


Figure 48: (u-r) Color-mass relation with post-starburst galaxies plotted in red circles

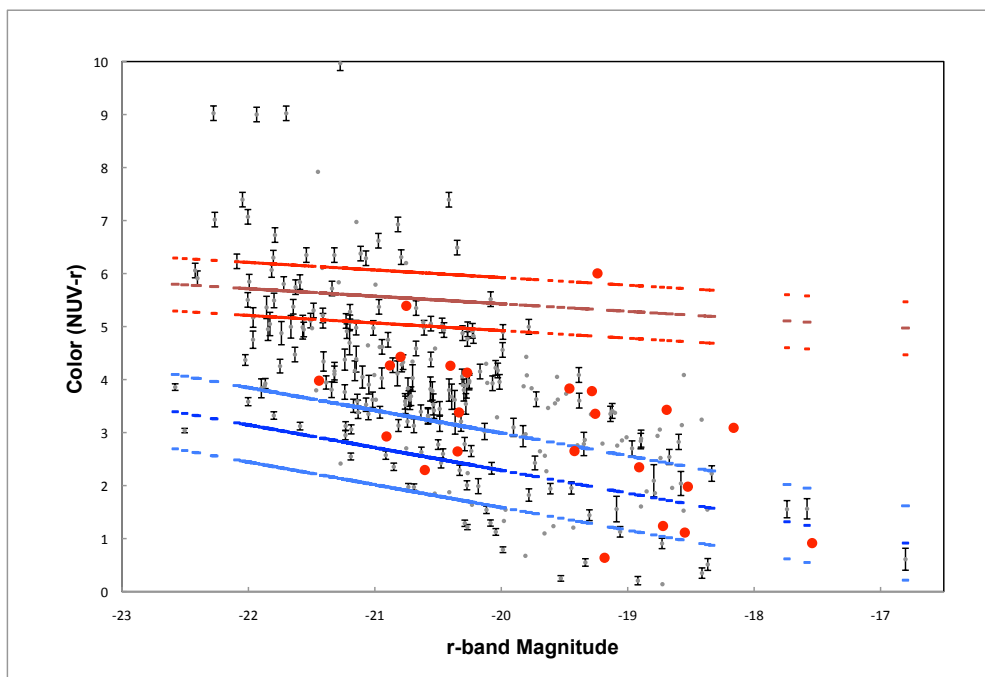


Figure 49: (NUV-r) Color-mass relation with post-starburst galaxies plotted in red circles

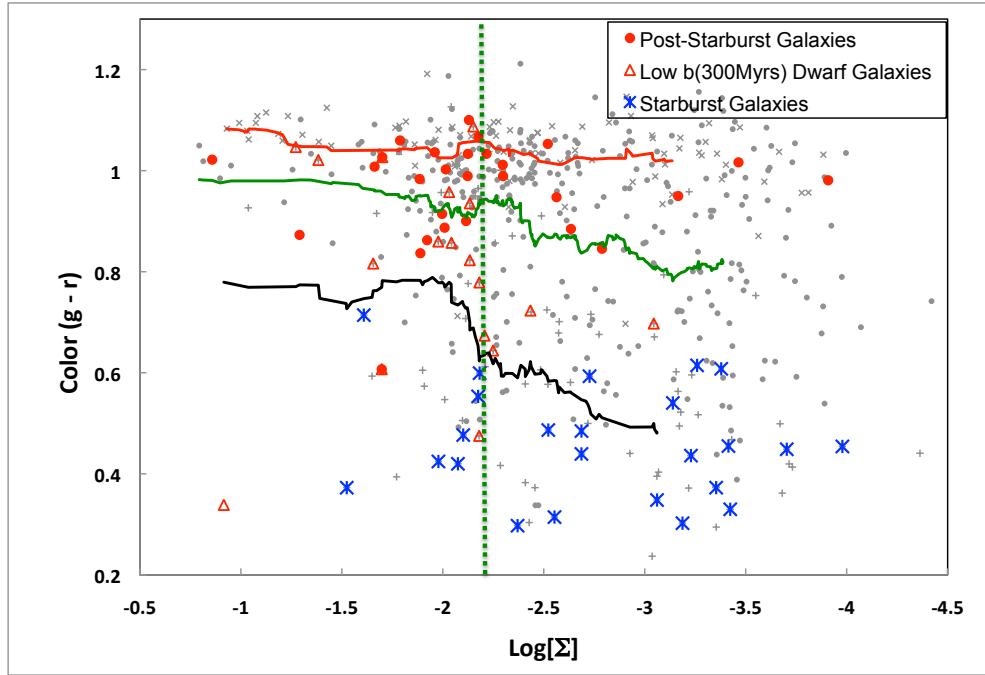


Figure 50: Moving average of $g-r$ Color - Σ for all galaxies. Black, green and red lines represent moving averages for dwarf, intermediate and high mass galaxies.

This indicates that the quenching of the galaxies with mass $< 10^{10.5} M_{\odot}$ is, at least in part, caused by the transitional (i.e. post-starburst) and quenched (low b_{300} galaxies at $\log(\Sigma) \geq -2$). The starburst galaxies appear to lie in a different region as compared to most of the post-starburst and low b_{300} dwarf galaxies, leading to the idea that the starburst phase of the galaxies might have led to the formation of the quenching/quenched galaxies and the subsequent redward trend of the galaxies. This observation is further supported by the results discussed in Section 6.6.

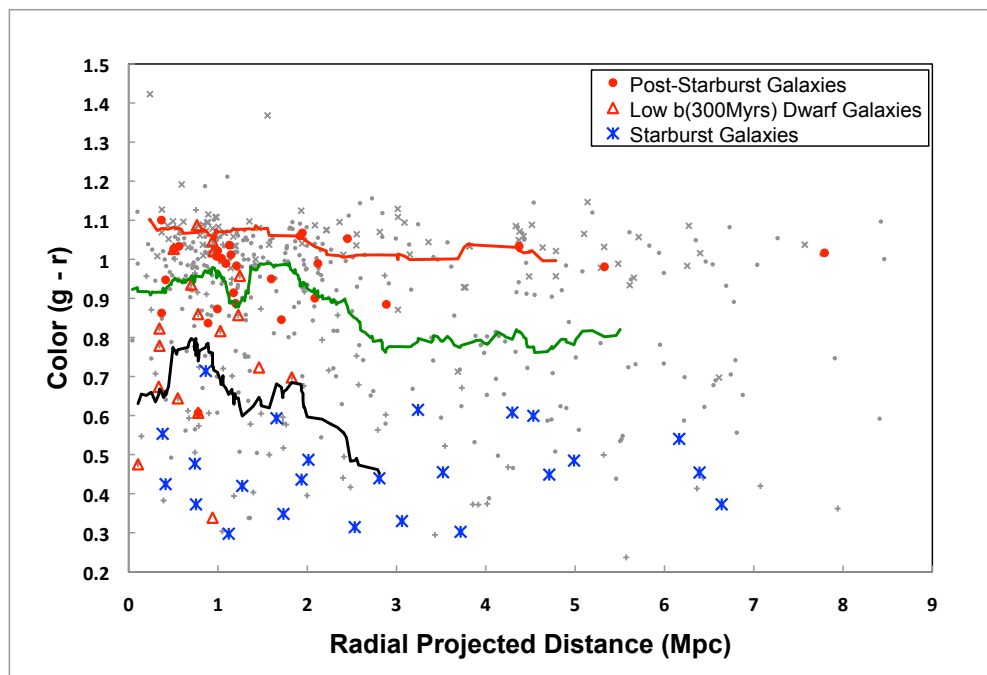


Figure 51: Moving average of $g-r$ Color - projected radial distance for all galaxies. Black, green and red lines represent moving averages for dwarf, intermediate and high mass galaxies.

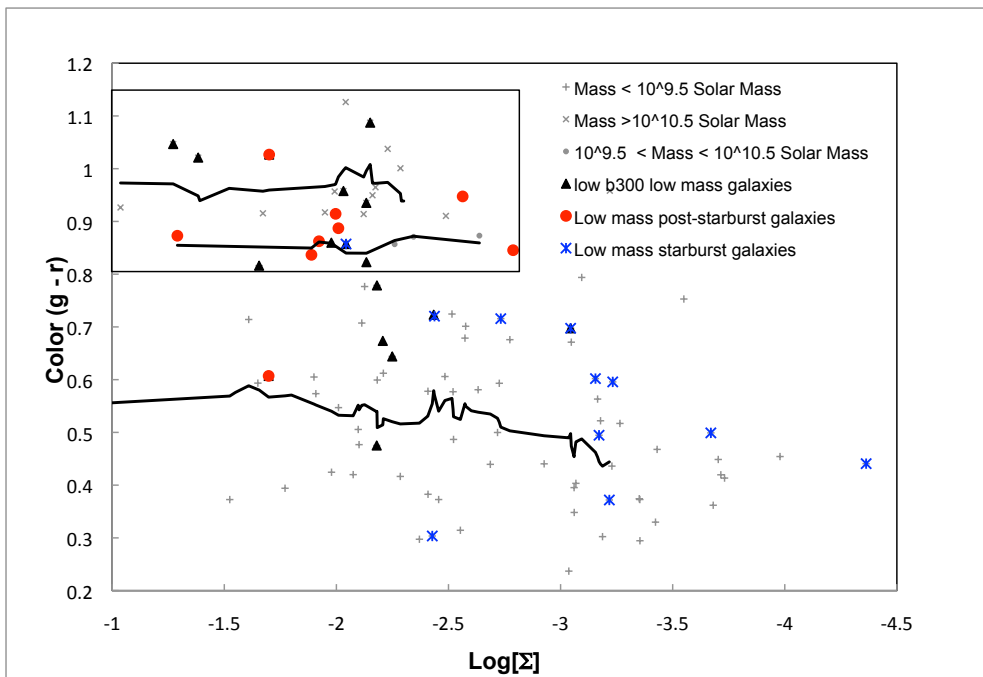


Figure 52: Moving average of $g-r$ Color - Σ for dwarf galaxies

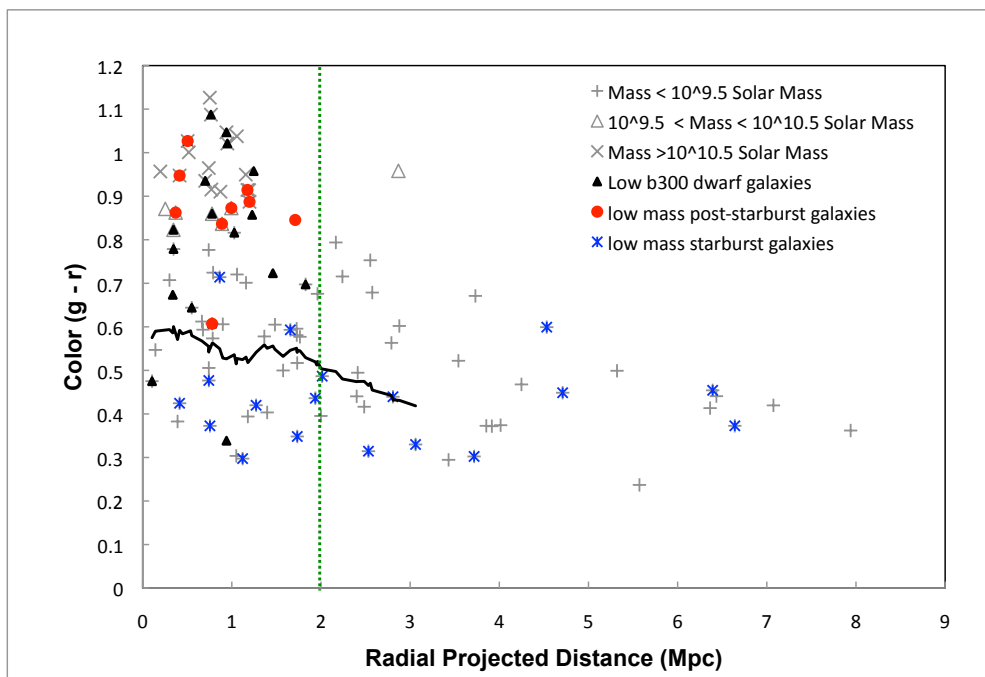


Figure 53: Moving average of $g-r$ Color - projected radial distance for dwarf galaxies

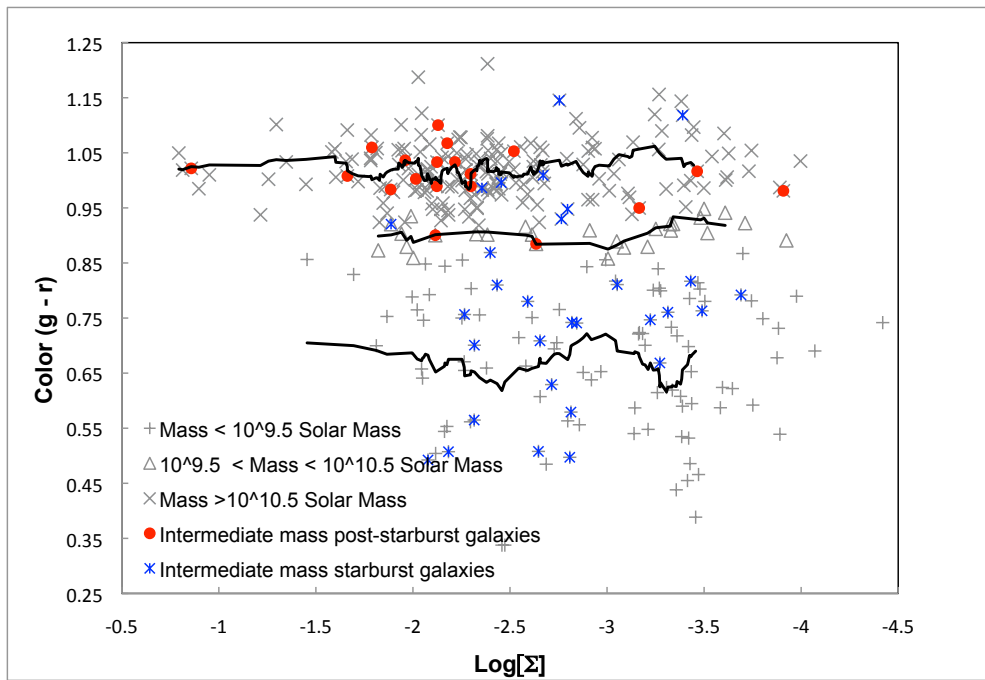


Figure 54: Moving average of $g-r$ Color - Σ for intermediate mass galaxies

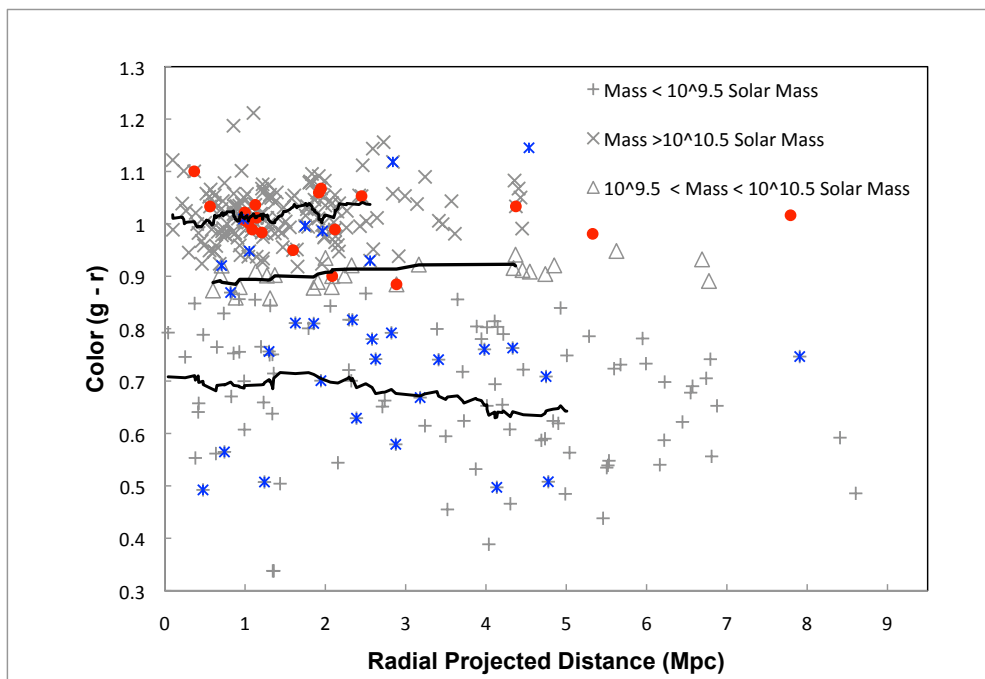


Figure 55: Moving average of $g-r$ Color - projected radial distance for intermediate mass galaxies

6.5 Evolution of Mean Equivalent Width Of $H\alpha$

The equivalent width of the $H\alpha$ ($EW[H\alpha]$) emission line is closely tied to the star formation rate of a galaxy (Figure 56). It reflects the star formation over past 10^6 years and hence can be used as a proxy for star formation in a galaxy. If galaxies are slowly quenched by interactions with their environment, we should see a decline in the mean $EW[H\alpha]$ (Balogh04). On the other hand, if star formation is triggered due to the impact of environment, the mean should increase. Hence, $EW[H\alpha]$ is tied closely to the birth rate parameter as well. Figure ?? shows a plot of $EW[H\alpha]$ against birth rate parameter over past 300 Myrs. We expect them to correlate. Although most of the data points show a correlation, some galaxies appear to have an extremely low b_{300} , while they have a huge spread in the value of $EW[H\alpha]$. The galaxies with low $EW[H\alpha]$ are forming few or no stars at present. The galaxies with high $EW[H\alpha]$ and low b_{300} are dusty starburst galaxies that do not show up well in optical colors.

The mean $EW[H\alpha]$ shows a steady decline from about a distance of 4 Mpc from the assumed center (Figure 57) indicating quenching in star formation in the galaxies as far out as 4 Mpc. It appears to have a uniform value in the outskirts beyond 4 Mpc, indicating no significant quenching beyond that radius. The majority of the post-starburst galaxies occur after the suppression of the mean $EW[H\alpha]$, closer to the groups, as expected. The starburst galaxies appear to avoid the densest regions in the structure (Figure 58). Here, positive values indicate an absorption in $H\alpha$, whereas a negative value indicates an emission.

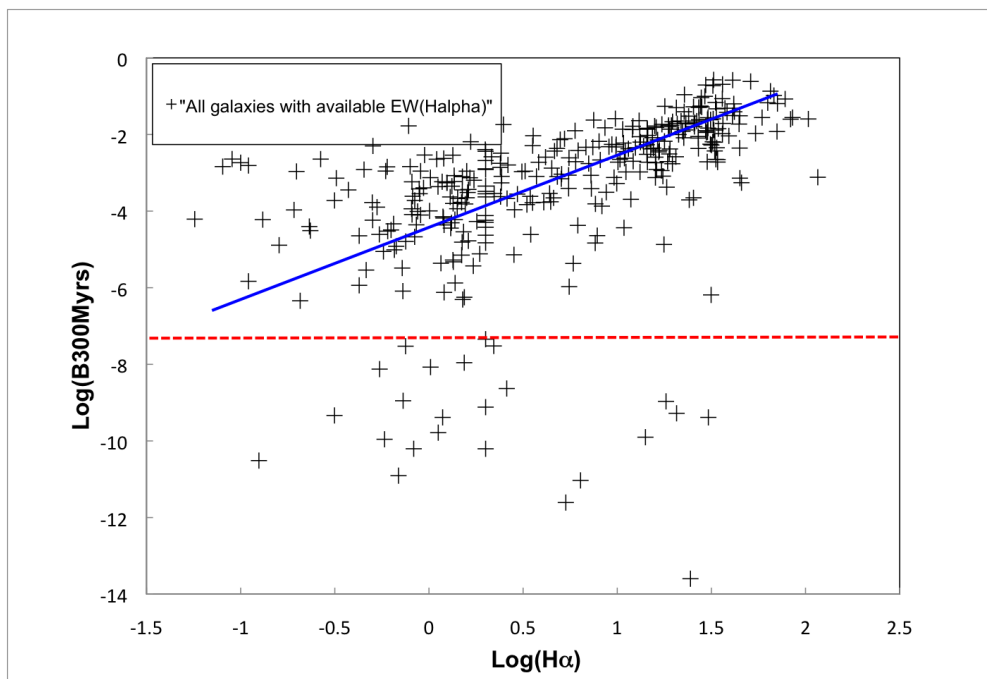


Figure 56: $\text{EW}(H\alpha)$ plotted against birth rate parameter over past 300 Myrs. Most of the galaxies show a correlation (blue line). Most of the galaxies below the red dashed line are severely quenched. Some of them are dusty starburst galaxies.

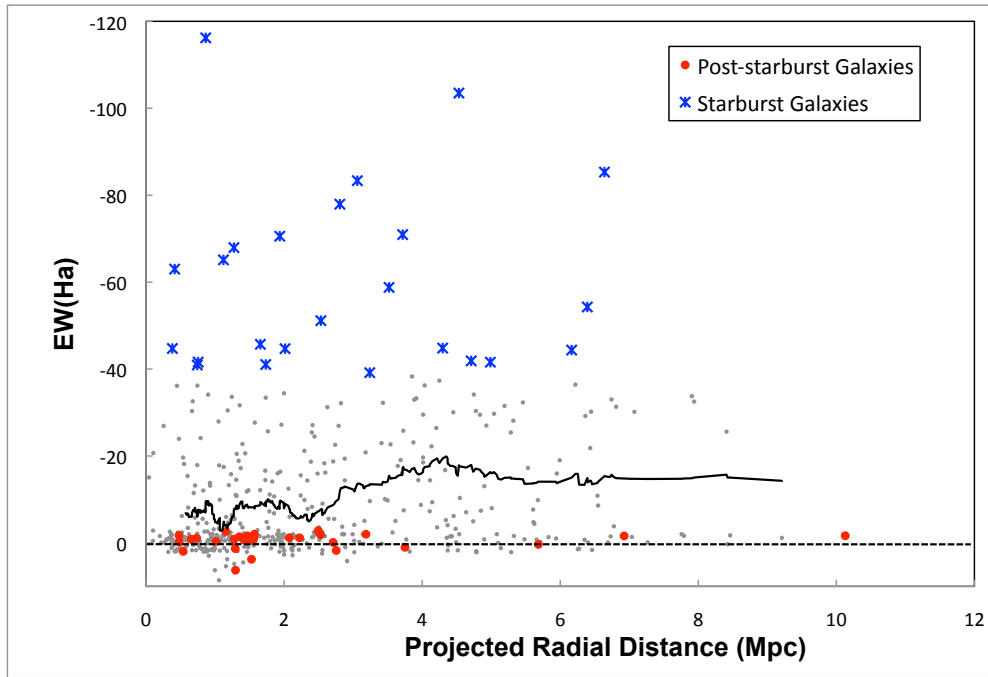


Figure 57: $EW(H\alpha)$ evolution with projected radial distance

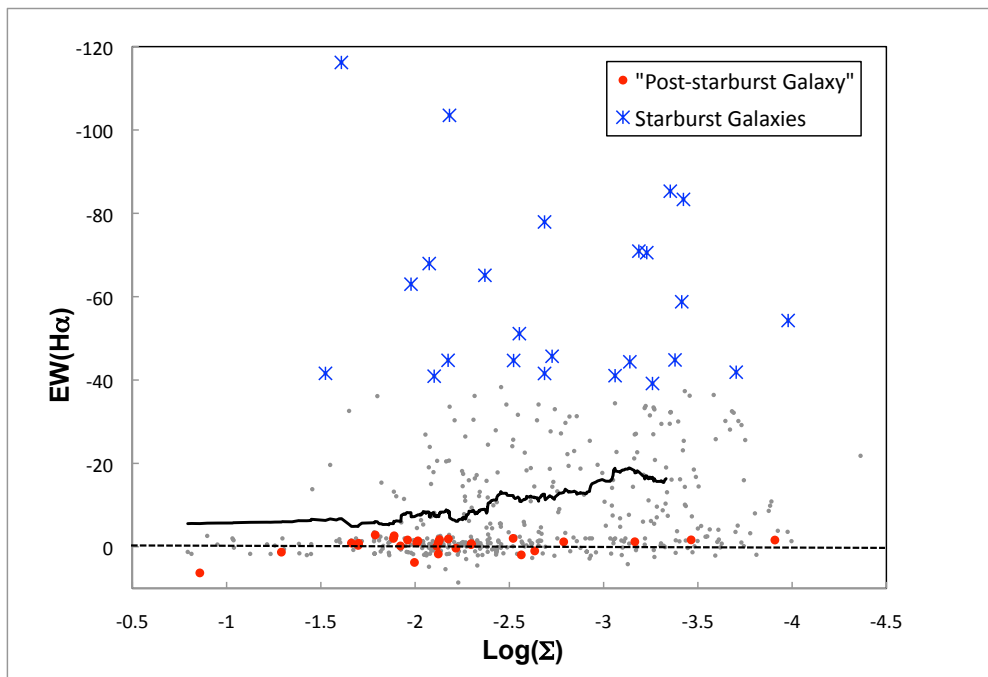


Figure 58: $EW(H\alpha)$ evolution with Σ

6.6 Spatial Sequencing Of Spectroscopically Classified Galaxies

We have spectroscopically classified the galaxies based on their emission and absorption lines as prescribed in Section 3. We have detected 28 k+a galaxies in the system, out of which 19 galaxies are intermediate mass galaxies and 9 galaxies are dwarf galaxies. We have also identified 24 galaxies as starburst galaxies, out of which 6 galaxies have an intermediate mass range and 18 galaxies are dwarf galaxies. None of the galaxies with mass $> 10^{10.5} (M_{\odot})$ show either starburst or post-starburst phases.

The starburst population preferentially lies within the cluster infall region and the FOF detected filaments, whereas the post-starburst galaxies are mostly confined within the groups (Figure 59). This shows a spatio-temporal sequencing of starburst and post-starburst galaxies and indicates an epoch of starburst far from the ICM associated with the group potential. We conclude that significant transformations in galaxies occur before reaching X-ray groups, thus ruling out ram pressure stripping due to group ICM as a mechanism for triggering these starburst galaxies. This is followed by sudden quenching close to the groups and/or within the groups themselves, which is possibly due to harassment and/or ram pressure stripping. The spatio-temporal sequence of the starburst galaxies far from the ICM and the post-starburst galaxies in the inner, denser region indicates that at least a subset of which must be progenitors of the quenched galaxies at the core of Abell 1882.

We next explore the possibility of a mass dependent quenching signature in the galaxy spectra. Even though the galaxies may traverse similar environments as they move from the filaments into the deeper recesses of the SuperGroup, the galaxy mass itself may be a crucial factor in determining the effect of the

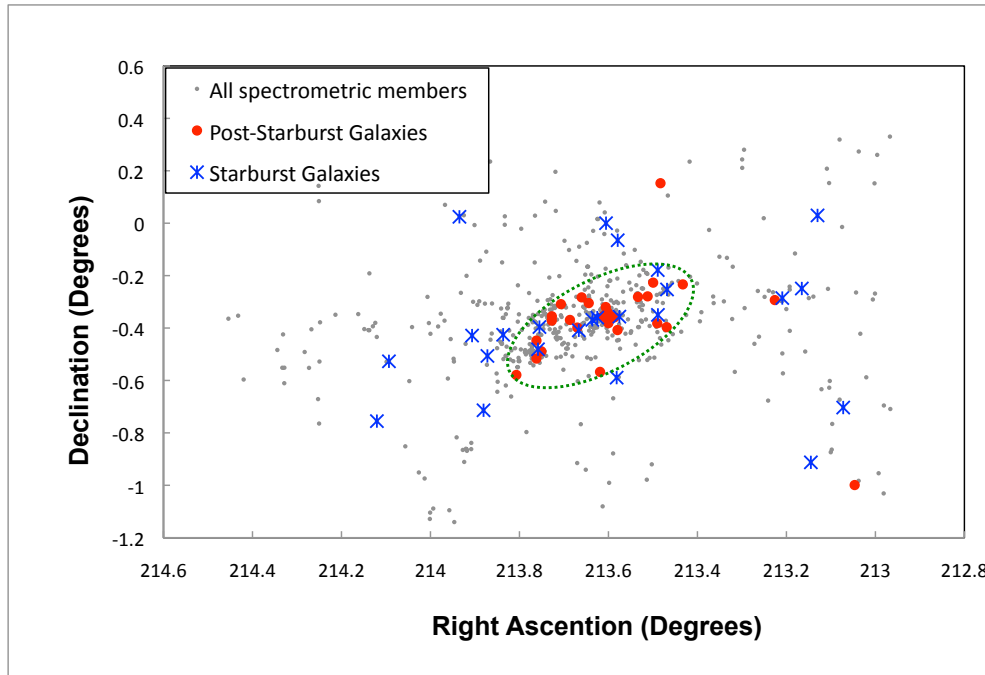


Figure 59: Spatial Distribution Of Starburst and Post-Starburst (k+a) Galaxies

environmental mechanisms on the transformation of galaxies.

For the dwarf galaxies, the thoroughly quenched post-starburst galaxies (quenched within 0.1-0.3 Gyrs) and the low b_{300} galaxies (quenched within 0.3-1 Gyrs) are confined within the groups (Figure 60). These populations have very different time scales for quenching and hence must have taken place at different times and possibly at different locations. While the intermediate mass quenched galaxies can be found in the groups and the immediate infall regions of the groups, they can also be found in the outskirts. We propose mergers as the mechanism for the intermediate mass galaxies that are quenched in the low density, low velocity environment in the outskirts, where the galaxies have enough time to be gravitationally bound and eventually merge.

However, the spatial location of the quenched dwarf galaxies is counter-intuitive

because we expect the shallow potential wells of the dwarf galaxies to be more susceptible to the gravitational interference much further out in the filaments and quench earlier than the higher mass galaxies which have deeper potential wells and hence are more difficult to quench. Below are some possible explanations and caveats.

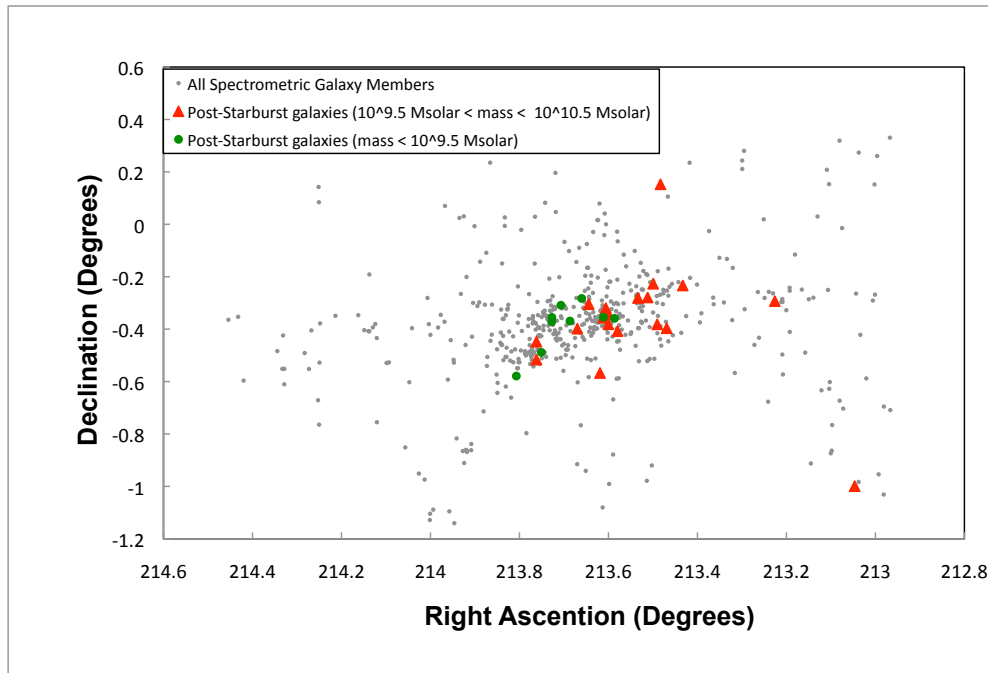


Figure 60: Spatial Distribution Of Post-Starburst (k+a) Galaxies For All Galaxies

For the low mass quenched galaxies, it is possible that these galaxies are remnants of intermediate mass galaxies which were quenched and simultaneously stripped of their gas and stars in the outer halo, turning them into low mass galaxies by the time they entered the group environment. However, we observe low mass starburst galaxies close to the groups, suggesting that at least some of the dwarf galaxies make it deep into the SuperGroup potential with their gas reservoir and hence at least some of the post-starburst galaxies are indeed quenched dwarf

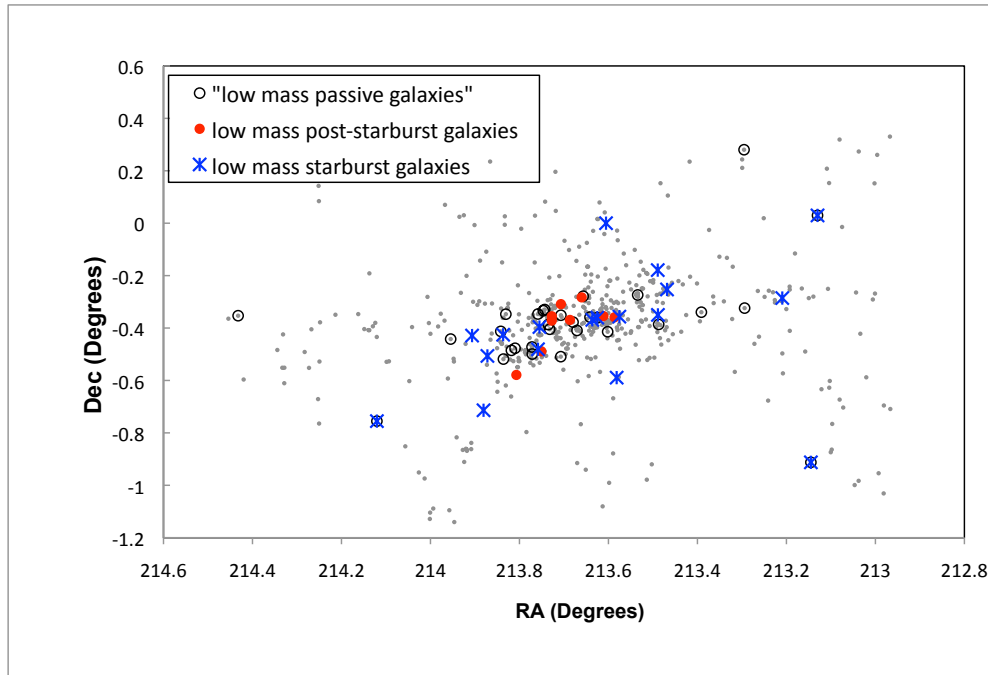


Figure 61: Spatial Distribution Of Starburst and Post-Starburst (k+a) Galaxies For Low Mass Galaxies

galaxies (Figure 61). We also see three times the number of dwarf starburst galaxies in the infall region of the groups as compared to the intermediate starburst galaxies, further confirming our suspicion that the dwarf galaxies somehow retain their gas content much further into the system as compared to the intermediate mass galaxies. It is possible that the dwarf galaxies have a smaller cross-section for mergers and hence do not quench by merging in the outskirts and retain their gas contents till they reach the inner regions.

The passive galaxies appear to prefer the high density regions and lie along the dense groups and the filaments (Figure 62).

Figure 61, 63 and 64 show the relative positions of passive, starburst and post starburst phases of galaxies as a function of their mass. The spatio-temporal sequence of the two spectral classes can be observed in both low mass as well as

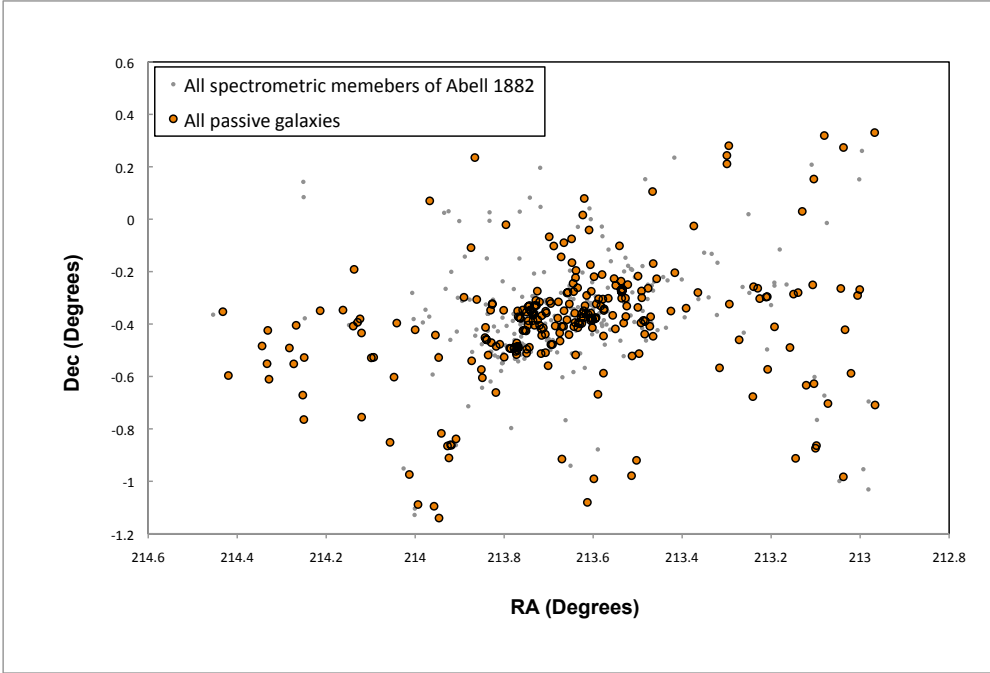


Figure 62: Spatial Distribution Of Passive Galaxies

intermediate mass galaxies.

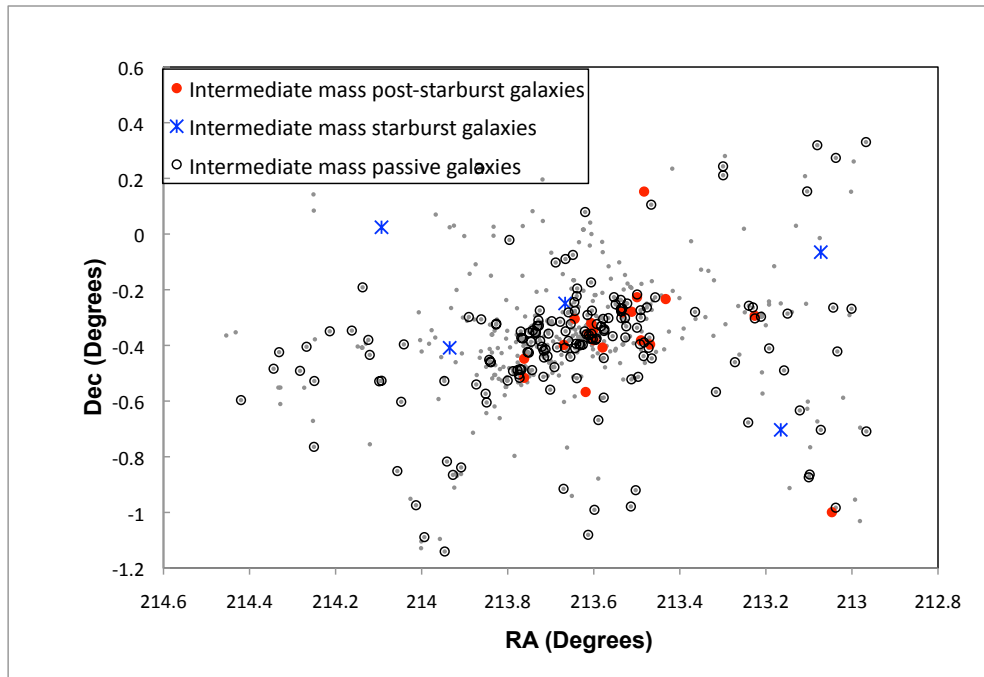


Figure 63: Spatial Distribution Of Starburst and Post-Starburst (k+a) Galaxies For Intermediate Mass Galaxies

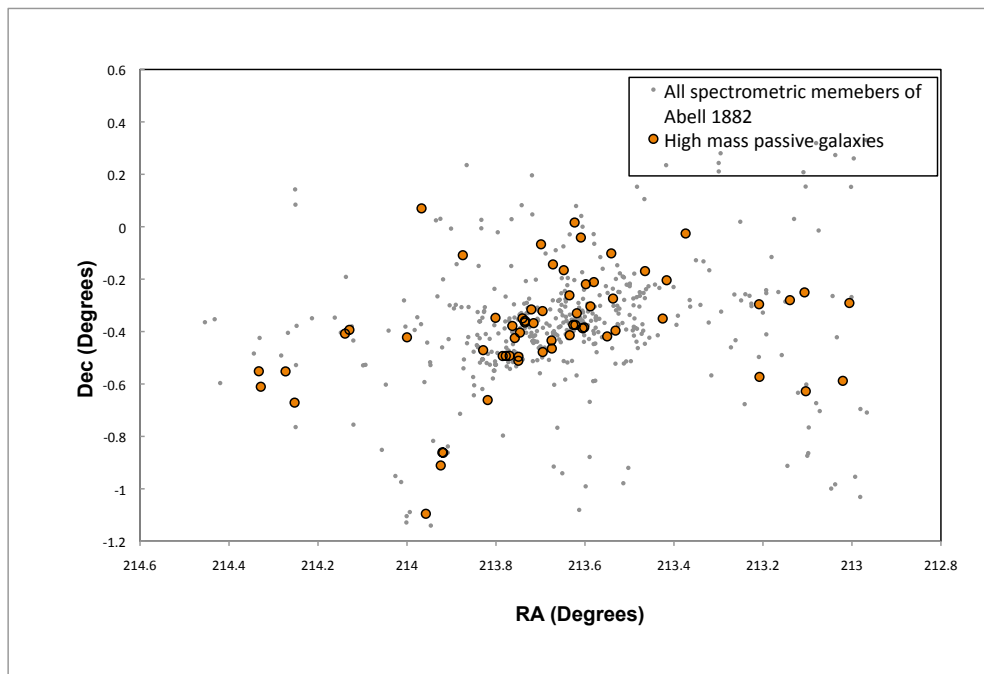


Figure 64: Spatial Distribution Of Passive Galaxies For High Mass Galaxies

7 SUMMARY AND FUTURE WORK

We have presented our data and results from multi-wavelength photometry and optical spectrometry of the nearest, extremely rich filamentary large scale structure, namely SuperGroup Abell 1882. It is a precursor of a Coma-like cluster and provides us with a unique opportunity to explore the galaxy transformations occurring in the far outskirts of the structures, as well as in the infall region and within the SuperGroup itself.

We see a huge local galaxy density effect as has been predicted by the past three decades of studies on galaxy transformations. Adding more details to the picture, we find a mass dependent transformation of galaxies. The lower mass galaxies appear to be more strongly affected and show a stronger redward trend with increasing local galaxy density and decreasing projected distance from the assumed center of Abell 1882 as compared to the intermediate mass galaxies. Due to archaeological downsizing of galaxies, the most massive galaxies have already made their stars at an earlier epoch and are not star forming by the time they enter the SuperGroup region. We also see a second order radial dependence of colors at a fixed local galaxy density. Color changes in the galaxies occur at least from 3 Mpc away from the assumed center, which is a couple of virial radii away from the SuperGroup. Over-abundance of passive galaxies along the filaments indicates that transformations in the filaments might have happened earlier and further away than the sample set.

The spatial location of post-starburst galaxies indicates that the intermediate mass galaxies have undergone transformation at the far outskirts, several virial radii away from the Supergroup and its associated ICM. We propose mergers as the environmental mechanism for this transformation, since it occurs in the

low density, low velocity dispersion region which is ideal for mergers. In order to confirm this, we plan optical and IR imaging using resources like JWST, WFIRST etc. to explore the morphology of these galaxies to see traces of mergers in the form of tidal tails, shells and asymmetric factor (ASY). There are also significant numbers of intermediate mass galaxies very close to the groups. These galaxies may be formed outside the groups. However, the caustic diagram indicates that these galaxies may also be backplash galaxies which are outward bound at this time.

The dwarf post-starburst and low b_{300} galaxies are spatially confined to the groups as opposed to that in the intermediate mass galaxies. This is counterintuitive because we expect the shallow potential wells of the dwarf galaxies to be affected much earlier than the intermediate mass galaxies. These dwarf galaxies somehow retained their gas reservoir till they entered the group ICM and underwent harassment or ram pressure stripping. Investigating this would require deep imaging of the r-band which represents the old stellar disk and is expected to be unperturbed during a ram pressure stripping. It would also require UV imaging, which is expected to show a heavily truncated $H\alpha$ disk at the upwind, i.e. in the direction of cluster, and a tail downwind, opposite to the direction of motion of the galaxy with respect to the ICM. Tidal stripping in the outskirts can also perturb the gas reserve of a galaxy enough to facilitate ram pressure stripping as the galaxies enter the ICM. We plan to undertake the above mentioned studies to address the question of whether these galaxies are quenched at a fixed stellar mass or lost mass due to harassment. We also plan to look for signs of harassment in the form of tidal tails and how much stellar mass has been lost from the galaxies overall and reside in the galaxy halos.

We also see a spatio-temporal sequence of starburst and post-starburst galaxies. The overall radial distribution of the spectral types show up as expected. The starburst galaxies occur at least a couple of virial radii away from the groups and are unlikely to be caused due to the ram pressure stripping by the ICM. The starburst galaxies predominantly occur within the filaments in the outskirts, or in the groups and their immediate infall regions. This indicates that mechanisms driven by filament environment may be key to galaxy transformations in the far outskirts. Post-starburst galaxies can be formed when a high continuous star formation is suddenly quenched, or when a starburst is suddenly quenched. Hence at least some of these starburst galaxies appear to be progenitors of the post starburst galaxies in the inner regions. We also found that the NUV is more sensitive to recent star formation episodes as compared to optical colors which have longer dynamical timescales and hence is a much robust diagnostic of post-starburst galaxy colors.

REFERENCES

- [1] Abell, George O. 1958ApJS....3..211A
- [2] Baldry, Ivan K. et al. 2004ApJ...600..681B
- [3] Baldry, Ivan K. et al. 2006MNRAS.373..469B
- [4] Balogh, Michael L. et al. 2004ApJ...615L.101B
- [5] Bekki, Kenji; Couch, Warrick J.; Shioya, Yasuhiro 2002ApJ...577..651B
- [6] Bell, Eric F. et al. 2004ApJ...608..752B
- [7] Bell, Eric F.; de Jong, Roelof S. 2001ApJ...550..212B
- [8] Bernardi, Mariangela et al. 2005AJ....129...61B
- [9] Blanton M. R., et al. 2001, AJ, 121, 2358
- [10] Blanton, Michael R. et al. 2001AJ....121.2358B
- [11] Blanton, Michael R., et al. 2003ApJ...594..186B
- [12] Bower, Richard G.; Lucey, J. R.; Ellis, Richard S. 1992MNRAS.254..589B
- [13] Bressan, Alessandro; Chiosi, Cesare; Fagotto, Franco 1994ApJS...94...63B
- [14] Brinchmann, Jarle; Ellis, Richard S. 2000ApJ...536L..77B
- [15] Brinchmann, J., et al. 2004, MNRAS, 351, 1151
- [16] Brough, S.; Forbes, D. A.; Kilborn, V. A.; Couch, W. 2006yCat..73701223B
- [17] Bundy, Kevin et al. 2006ApJ...651..120B

- [18] Calzetti, D., et al. 2007ApJ...666..870C
- [19] Cardelli, Jason A. et al. 1989ApJ...345..245C
- [20] Cooper, Michael C., et al. 2007MNRAS.376.1445C
- [21] Cowie, Lennox L. et al. 1996AJ....112..839C
- [22] Cucciati, O., et al. 2006astro.ph.12120C
- [23] de Vaucouleurs, G. 1953AJ.....58...30D
- [24] de Vaucouleurs, G.; Capaccioli, M. 1979ApJS...40..699D
- [25] Diaferio, Antonaldo; Geller, Margaret J. 1997astro.ph..1034D
- [26] Dressler, A., 1980ApJ...236..351D
- [27] Dressler, Alan et al. 1997ApJ...490..577D
- [28] Dressler, Alan et al. 1999ApJS..122...51D
- [29] Erkurt,A. et al. 2009POBeo..86..305E
- [30] Evrard, August E. et al. 1996ApJ...469..494E
- [31] Fadda,Dario, 2008galx.prop...18F
- [32] Fassbender, R., et al. 2011A&A...527L..10F
- [33] Felten, J. E. 1977AJ.....82..861F
- [34] Fleenor,M.C.; Johnston-Hollitt,M., 2010ASPC..423...81F
- [35] Fujita, Yutaka 1998ApJ...509..587F

- [36] Gallazzi, Anna et al. 2006MNRAS.370.1106G
- [37] Geller, M. J.; Diaferio, Antonaldo; Kurtz, M. J. 1999ApJ...517L..23G
- [38] Gmez, Percy L., et al. 2003ApJ...584..210G
- [39] Gomez, P. L. et al. AAS Meeting 215, 351.03
- [40] Gomez, Percy L. et al. 2010AAS...21535103G
- [41] Gonzalez, Anthony H. et al. 2005ApJ...624L..73G
- [42] Goto, Tomotsugu et al. 2003MNRAS.346..601G
- [43] Gunn, James E.; Gott, J. Richard, III 1972ApJ...176....1G
- [44] Hashimoto, Yasuhiro et al. 1998ApJ...499..589H
- [45] Heavens, Alan et al. 2004Natur.428..625H
- [46] Hogg, David W. et al. 2004ApJ...601L..29H
- [47] Huchra, J. P.; Geller, M. J. 1982ApJ...257..423H
- [48] Huchra, J.P. 1983HiA.....6..749H
- [49] Icke, V. 1985A&A...144..115I
- [50] Jimenez, Raul et al. 2005MNRAS.356..495J
- [51] Kaiser, Nick 1987MNRAS.227....1K
- [52] Kauffmann, Guinevere; Charlot, Stephane 1998astro.ph.10031K
- [53] Kauffmann, Guinevere et al. 2004MNRAS.353..713K

- [54] Kautsch, Stefan J. et al. 2008ApJ...688L...5K
- [55] Kaviraj, S. et al. 2005MNRAS.360...60K
- [56] Keel, William C. 2007rgf..book.....K
- [57] Kennicutt, R. C., Jr. 2004yCat.7141....0K
- [58] Kennicutt,RobertC.,Jr., 1998ARA&A..36..189K
- [59] Kennicutt,RobertC. et al. 2009ApJ...703.1672K
- [60] Kodama, T.; Arimoto, N. 1997A&A...320...41K
- [61] Kroupa,Pavel, 2000NewA....4..615K
- [62] Lagache, Guilaine; Puget, Jean-Loup; Dole, Herv 2005ARA&A..43..727L
- [63] Larson, R. B.; Tinsley, B. M.; Caldwell, C. N. 1980ApJ...237..692L
- [64] Larson, Richard B. 1974MNRAS.166..585L
- [65] Lewis, Ian et al. 2002MNRAS.334..673L
- [66] Lopez-Cruz, Omar et al. 2004ApJ...614..679L
- [67] Mahajan, Smriti et al. 2010MNRAS.404.1745M
- [68] Mahajan, Smriti et al. 2011MNRAS.412.1098M
- [69] Mamon, G. A. et al. 2004A&A...414..445M
- [70] Marcillac,D.; Rigby,J.R.; Rieke,G.H.; Kelly,D.M., 2007ApJ...654..825M
- [71] Martin,D.Christopher et al. 2007ApJS..173..342M

- [72] McIntosh, Daniel H. et al. 2005ApJ...619..193M
- [73] Miller, Christopher J. et al. 2010AAS...21641801M
- [74] Moore, Ben et al. 1996Natur.379..613M
- [75] Moore, Ben; Lake, George; Katz, Neal 1998ApJ...495..139M
- [76] Morrison, Glenn et al. 2008sptz.prop50292M
- [77] Nelan, Jenica E. et al. 2005ApJ...632..137N
- [78] Oke, J. B.; Gunn, J. E. 1983ApJ...266..713O
- [79] Panter, B., Heavens, A. F., & Jimenez, R. 2003, MNRAS, 343, 1145
- [80] Peebles, P. J. E.; Yu, J. T., 1970ApJ162..815P
- [81] Petrosian, V. 1976ApJ...209L...1P
- [82] Pimbblet, Kevin A. et al. 2002MNRAS.331..333P
- [83] Pimbblet, Kevin A. 2011MNRAS.411.2637P
- [84] Porter, Scott C. et al. 2008MNRAS.388.1152P
- [85] Postman, M.; Geller, M. J. 1984ApJ...281...95P
- [86] Postman, M. et al. 2005ApJ...623..721P
- [87] Press, William H.; Schechter, Paul 1974ApJ...187..425P
- [88] Quilis, Vicent; Moore, Ben; Bower, Richard 2000Sci...288.1617Q
- [89] Richstone, D. O. 1976ApJ...204..642R

- [90] Salim,Samir, et al. 2007ApJS..173..267S
- [91] Salim,Samir; Rich,R.Michael 2010ApJ...714L.290S
- [92] Schechter, P. 1976ApJ...203..297S
- [93] Schiminovich,David et al., 2007ApJS..173..315S
- [94] Schlegel, David J.; Finkbeiner, Douglas P.; Davis, Marc 1998ApJ...500..525S
- [95] Strateva,Iskra et al. 2001AJ....122.1861S
- [96] Smith, Graham P. et al. 2005ApJ...620...78S
- [97] Snyder, Gregory F. et al. 2011ApJ...741...77S
- [98] Spitzer, Lyman, Jr.; Baade, Walter 1951ApJ...113..413S
- [99] Thilker, David A., et al. 2007ApJS..173..572T
- [100] Thomas, Daniel et al. 2005ApJ...621..673T
- [101] Toomre, Alar; Toomre, Juri 1972ApJ...178..623T
- [102] Tremonti, C. A. et al. 2004, ApJ, 613, 898
- [103] Treu, Tommaso et al. 2003ApJ...591...53T
- [104] Yi, S. K.; Yoon, et al. 2005ApJ...619L.111Y
- [105] Yoon, Joo H. et al. 2008ApJS..176..414Y
- [106] van Dokkum, Pieter G. et al. 1998ApJ...500..714V
- [107] Visvanathan, N.; Sandage, A. 1977ApJ...216..214V

[108] Vollmer, Bernd 2013pss6.book..207V

[109] Werner, M.; Gorjian, V.; Lawrence, C. 2004AAS...20511018W

[110] Wyder, Ted K. et al. 2007ApJS..173..293W